Università degli Studi di Torino

Doctoral School of University of Turin
PhD in Chemical and Materials Sciences

XXXIV Cycle 2019-2022

Universität Leipzig

Faculty for Physics and Earth Sciences

Paramagnetic Transition Metal Ions on Oxide Surfaces: an EPR Investigation

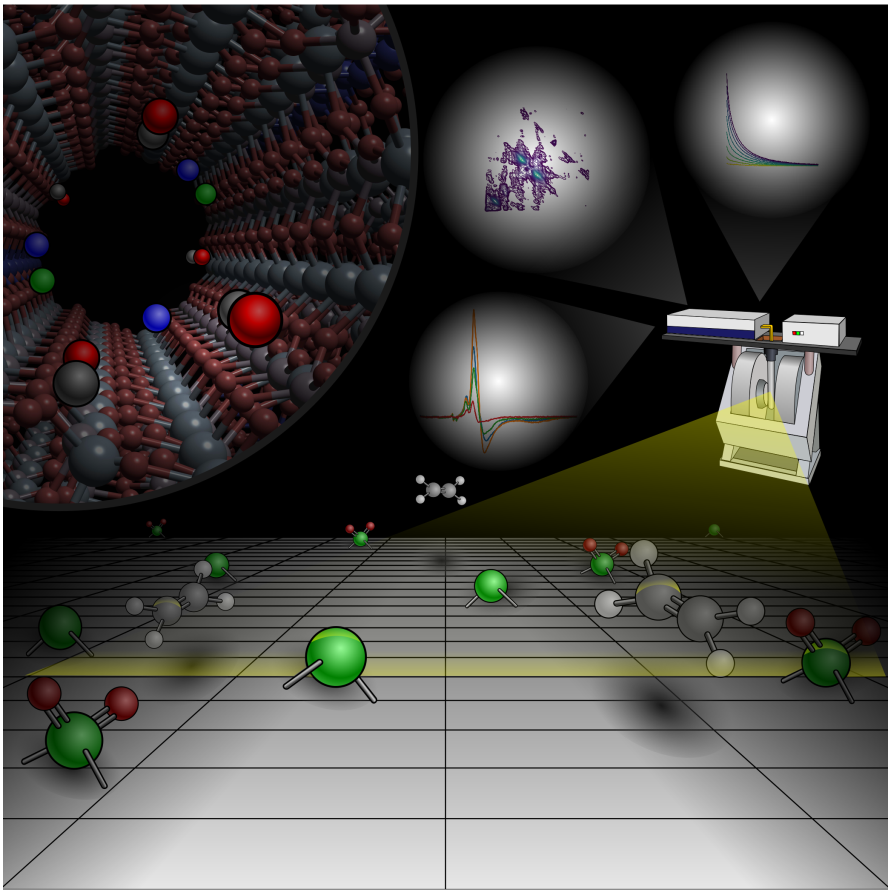

Yu-Kai Liao
Promoters:

Prof. Mario Chiesa
Prof. Andreas Pöppl

Paramagnetic Transition Metal Ions on Oxide Surfaces: an EPR Investigation

Der Fakultät für Physik und Geowissenshaften

der Universität Leipzig

eingereichte

DISSERTATION

zur Erlangung des akademischen Grades

doctor rerum natrualium

(Dr. rer. nat.)

vorgelegt

von M.Sc. Yu-Kai Liao

geboren am 28.09.1990 in Chiayi

Gutachter:
Prof. Dr. Eike Brunner
Dr. Andrea Folli

Tag der Verleihung 27.02.2023

Bibliographische Beschreibung:

Liao, Yu-Kai
Paramagnetic Transition Metal Ions on Oxide Surfaces: an EPR Investigation
Universität Leipzig, Dissertation 2022
99 S.,[1] 143 Lit.,[2] 49 Abb., 9 Tab., 1 Anlage

Refarat (Abstract):

A long standing problem in catalysis is the identification and characterization of the active sites, i.e. an atom or an ensemble of atoms spouse on the surface of a catalyst.[3] One relevant case, that is treated in this thesis, is constituted by the Phillips catalyst.[4] For several reasons, even though this catalyst has be applied at industrial scale for decades and is accounted for a majority of the high density polyethylene (HDPE) production, the identification and the mechanism of the active sites are still under debate. This work was initiated in the framework of the PARACAT project,[5] which is dedicated to study the paramagnetic species in catalysis, and focuses on "The role of Cr paramagnetic states in olefin polymerization over Phillips catalyst." In the course of the study, I brought this research to a larger scale which included but was not limited to the Phillips catalyst itself. Considering the relevance of the interaction between transition metal ions (TMI) and the support to the catalytic activity, I worked on systems that cover a number of oxide-supported TMIs by means of electron paramagnetic resonance (EPR) spectroscopy.

In this thesis I investigated the paramagnetic Cr(V) and Cr(III) species in the Phillips catalyst. Cr(V) species were used as spin probes to provide more information on the overall system. Besides studying the Phillips catalyst itself, I studied also the silica supported organometallic-Cr catalyst, $Cr[CH(SiMe_3)_2]_3/SiO_2$, which served as a model system to investigate the catalytic active Cr species with well-defined oxidation states and geometry. On the other hand, microporous materials including zeolites and zeotype materials such as aluminophosphate (AlPO) can be engineered with different physical and chemical properties in terms of chemical composition and provide a relevant example of structure sensitivity of a heterogeneous catalyst. Such structure sensitivity is highly relevant in catalysis and can be very well studies with EPR spectroscopy. In this regard, I investigated a series of SAPO-5 materials doped with different TMI. In the first place, the incorporation of Cr in SAPO-5 was studied focuses on the discrimination of isomorphous substitution at framework sites and extra-framework sites. In addition, a method to prepare a bi-metallic Mo/V-SAPO-5 system was developed and the metal-metal synergy was validated with a single electron transfer reaction and the short range hyperfine interaction. Finally, the surface properties of SAPO-5 were studied by adsorbing NO radicals in the pores and investigating their interaction with the surface.

---

[1] ··· S. (Seitenzahl insgesamt)

[2] ··· Lit. (Anzahl der im Literaturverzeichnis ausgewiesenen Literaturangagen)

[3] Taylor, Hugh Stott. “A Theory of the Catalytic Surface.” *Proceedings of the Royal Society of London. Series A, Containing Papers of a Mathematical and Physical Character* 108, **1925**, 105–11.

[4] Hogan, J. P.; Banks, R. L. Polymers and production thereof, U.S. Patent 2,825,721. 1958

[5] `https://paracat.eu`

Contents

1 Paramagnetic Transition Metal Ions at Surfaces 1

1.1 Phillips Based Systems 1

1.2 TMI in Crystalline Microporous Materials 4

1.2.1 Single Atom Catalyst 5

1.2.2 Bi-Metallic Catalyst 6

2 Electron Paramagnetic Resonance 13

2.1 Continuous Wave EPR 13

2.2 Spin Hamiltonian 16

2.2.1 Electron Zeeman Interaction 16

2.2.2 Zero Field Interaction 19

2.2.3 Nuclear Zeeman Interaction 19

2.2.4 Hyperfine Interaction 21

2.2.5 Nuclear Quadrupolar Interaction 21

2.3 Spin Dynamics 22

2.4 Experimental Methods 25

2.4.1 Quantitative EPR 25

2.4.2 Instantaneous Diffusion 25

2.4.3 Echo-Detected Field Sweep (EDFS) 26

2.4.4 Hyperfine Sublevel Correlation Spectroscopy 28

3 Materials and Methods 35

3.1 Materials 35

3.1.1 Phillips Catalyst 35

3.1.2 $Cr(CH(SiMe_3)_2)_3/SiO_2$ 35

3.1.3 Silico-Aluminophosphate-5 (SAPO-5) 36

3.2 Treatments **36**
3.2.1 Cr-based Catalyst: Activation and Ethylene Polymerization 36
3.2.2 Silico-Aluminophosphate-5 (SAPO-5): Activation and Reactivity 37
3.2.3 Silico-Aluminophosphate-5 (SAPO-5): Bi-Metallic System 38
3.3 EPR Characterization **38**

4 Results and Discussion: Chromium on Silica 41
4.1 Phillips Catalyst **41**
4.1.1 Coordination of Cr(V) 41
4.1.2 Reactivity of Cr(V) 44
4.1.3 Distribution of Cr(V) 47
4.2 Organometallic-Cr on Silica **48**
4.2.1 Structure of the Grafted Cr 48
4.2.2 Quantitative Analysis of the Grafted Cr 51
4.2.3 Reactivity of the Grafted Cr 52

5 Results and Discussion: SAPO-5 57
5.1 Cr-Incorporated SAPO-5 . . . . **57**
5.1.1 Coordination of the Pentavalent Cr 57
5.1.2 Local Environment of the Pentavalent Cr 61
5.2 Bi-Metallic Mo/V-SAPO-5 . . . . **63**
5.2.1 Local Environment of V-SAPO-5 63
5.2.2 Local Environment of Mo/V-SAPO-5 69
5.3 NO-Adsorbed SAPO-5 . . . . **71**
5.3.1 Distinguishing NO Adsorption Sites 72
5.3.2 Characterizing Adsorption Sites 74

6 Summary 83

Appendices 87

A Acronyms and Symbols 87
Acronyms **87**
Symbols **88**

List of Figures

1.1 The collection of characterization techniques for TMI (green balls) at surfaces. 2

1.2 The structures of a) ZSM-5 and b) SAPO-5. 4

2.1 The diagram of the magnitudes of different spin interactions. 14

2.2 The scheme diagrams of the CW-EPR mechanism 15

2.3 The scheme of spin-orbit coupling effect on the tetragonal distortion for the tetrahedral coordinate d-orbital. 17

2.4 The powder spectra for axial and rhombic g-tensors. 18

2.5 The *zfi* diagram for different spins at zero-field. 20

2.6 The schematic diagram of the time evolution of the electron spin. 23

2.7 A scheme of density matrix for a two spin system 24

2.8 The scheme of T_m mechanisms. 26

2.9 The scheme of the Instantaneous Diffusion. 27

2.10 The scheme of the 2-pulse sequence and the echo-detected field sweep (EDFS). 27

2.11 The scheme of the HYSCORE Spectroscopy 28

2.12 The scheme of the nuclear frequencies in the two electron manifolds. 29

2.13 The scheme of HYSCORE crosspeaks corresponding to different coherence transfering pathways with the τ suppression effect. 30

3.1 The PXRD pattern of the calcined Cr-SAPO-5 36

3.2 Isotropic part of ^{27}Al MAS spectra of four SAPO-5 samples. 37

3.3 A scheme of Mo/V-SAPO-5 Grafting Method using the EPR cell and flask with teflon stopcocks. 38

4.1 The X-band CW-EPR of the activated Phillips catalysts with different Cr concentrations measured at 77 K. 42

4.2 The X-band EDFS spectra of the 0.1 wt% Phillips catalyst measured at 10 K. 43

4.3 The X-band a) CW-EPR and b) EDFS spectra of 0.1 wt% Cr Phillips catalyst. 43

4.4 The CW-EPR spectra of the 0.1 wt% Cr Phillips catalyst at 77 K during the reaction with ethylene. 45

4.5 The relative population of the paramagnetic Cr species during the reaction with ethylene of 0.1 wt% Cr Phillips catalyst. 45

4.6 The CW-EPR spectra of the 0.05 wt% Cr Phillips catalyst at 77 K during the reaction with ethylene. 46

4.7 The relative population of the paramagnetic Cr species during the reaction with ethylene of 0.05 wt% Cr Phillips catalyst. 46

4.8 The spin-spin relaxation experiments at X-band of the 1 and 0.5 wt% Cr Phillips catalyst. . 47

4.9 The CW-EPR spectra of (1) CrR_3 in hexane and (2) $CrCl_3$ in water at 77 K. 49

4.10 The CW-EPR spectra of the a) experiments of the $n$$CrR_3/SiO_2$ and the relative amount of different Cr sites in the inset and b) each simulated Cr species. 50

4.11 The rhombogram for S=3/2 species. 50

4.12 The scheme for CrR_3 grafting on silica surface. 51

4.13 The experimental and simulated CW-EPR spectra of the $n$$CrR_3/SiO_2$. 52

4.14 The CW-EPR spectra of the $0.2$$CrR_3/SiO_2$ (1) before and (2) upon reaction with ethylene. 53

5.1 The structure of SAPO-5. 58

5.2 The CW-EPR spectra of the as-synthesized and calcined Cr-SAPO-5 sample recorded at 77 K. 58

5.3 The X-band CW-EPR spectra at 77 K and Q-band EDFS spectra at 30 K of the Cr-SAPO-5. 59

5.4 The Q-band standard 4-pulse HYSCORE, experimental 6-pulse HYSCORE, and simulated HYSCORE spectrum. 62

5.5 Fully optimized structure of Cr-SAPO-5 periodic models. 62

5.6 Experimental and simulated CW-EPR spectra of V-SAPO-5 recorded at X-band and Q-band. 64

5.7 The Q-band V-SAPO-5 EDFS spectrum and HYSCORE spectrum measured at T = 30K. . . . 67

5.8 The Q-band V-SAPO-5 EDFS spectrum and Remote-HYSCORE spectrum measured at T = 30 K. 68

5.9 The CW X-band EPR spectra of VCl_4 deposited at increasing doses on Mo-SAPO-5. 69

5.10 The Q-band Mo/V-SAPO-5 EDFS spectrum and HYSCORE spectrum measured at T = 30K. 70

5.11 The Q-band Mo/V-SAPO-5 CW-EPR spectrum, EDFS spectrum, Remote-HYSCORE, and standard-HYSCORE spectrum measured at T = 30 K. 71

5.12 X-band CW-EPR spectra of the NO-adsorbed SAPO-5. 73

5.13 The X-band ^{27}Al HYSCORE spectra of the NO-adsorbed SAPO-5. 75

5.14 The X-band ^{1}H HYSCORE spectra of the NO-adsorbed SAPO-5. 76

5.15 The application of the method for ^{1}H HYSCORE spectrum analysis. 76

5.16 The X-band EDFS and both experimental and simulated ^{1}H HYSCORE spectra of **L20** at two field positions. 78

5.17 The scheme of the water-NO coordination for *hfi* theoretical calculation and the resulting water-NO distances corresponding to different spin density distributions. 79

List of Tables

2.1 The g-factors of nuclei that appeared in this work. 20

4.1 The spin Hamiltonian parameters for Cr(V) in the Phillips catalyst from this work and some literature. 44

4.2 Spin concentration of the 1 and 0.5 wt% Cr Phillips catalyst with instantaneous diffusion analysis and spin counting. 48

4.3 The spin Hamiltonian parameters of the Cr species in the nCrR$_3$/SiO$_2$. 51

5.1 Spin Hamiltonian parameters of Cr-SAPO-5. 60

5.2 Spin Hamiltonian parameters of Mo/V-SAPO-5 derived from the simulations of the CW-EPR spectra. 65

5.3 Hyperfine coupling parameters of Mo/V-SAPO-5 derived from the simulations of the HYSCORE spectra. 65

5.4 The name of the samples for the NO-adsorbed SAPO-5 and their corresponding experimental condition. 72

5.5 The spin Hamiltonian parameters derived from CW-EPR of the physisorbed NO. 74

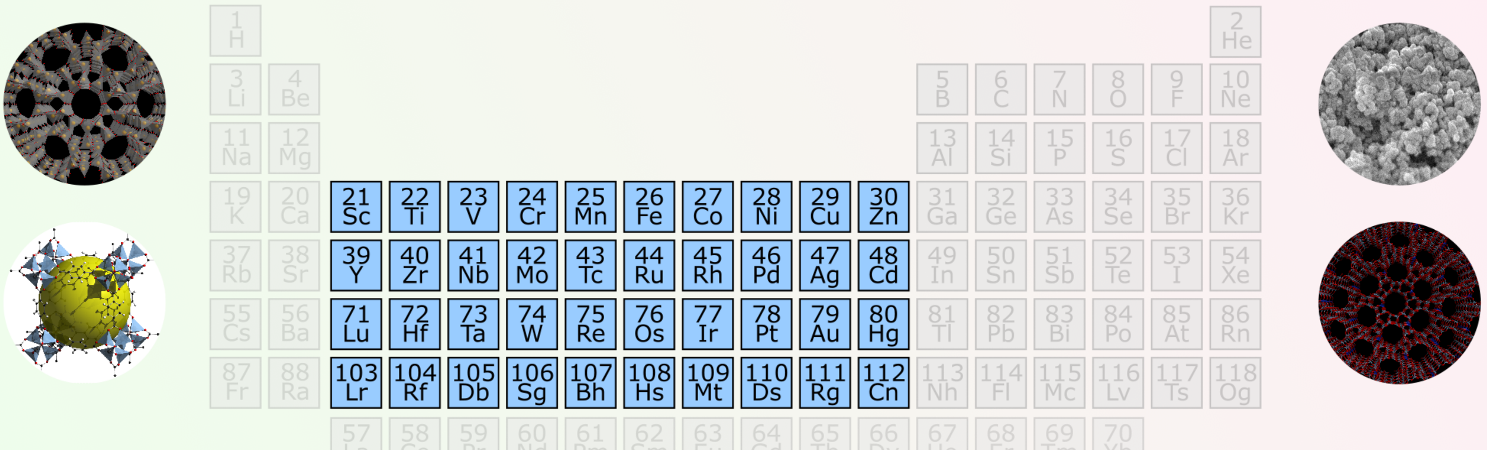

1. Paramagnetic Transition Metal Ions at Surfaces

Transition metal elements are characterized by partially filled d orbitals and display a wide variability of oxidation states and coordination numbers. These properties provide the basis for the diverse chemical behavior and the relevance in catalysis of transition metal ions (TMI). TMI can serve as catalytic active sites[1–3] and used to tune the redox or acidity properties of different supports,[4] which can range from inorganic oxides,[2, 5–8] zeolites,[2, 9, 10] zeotype materials,[3, 4] to metal-organic frameworks (MOFs).[11–13]

Porous materials are characterized by their regular and uniform porous structures. The pore size and pore shape are the most significant parameters that are used for describing the structure. According to the International Union of Pure and Applied Chemistry (IUPAC),[14] the porous materials are classified as microporous (pore width <2 nm), mesoporous (pore width 2-50 nm), and macroporous (pore width >50 nm). The distribution of the size, shape, and volume of the pores in the materials are related to the performance for the desired functionality. In terms of catalysis, these dimensions also determine the activity and selectivity.[15]

It is however a demanding challenge to characterize TMI containing materials and a collection of experimental methods is required to obtain the complementary picture. (Fig.1.1) In terms of the open-shell TMI species, electron paramagnetic resonance (EPR) can be a powerful technique providing the localized information including the local coordination geometry,[16–18] chemical environment,[9, 19–22] and the dispersion/distribution of the TMI.[23–25] In the case of EPR-silent TMI species, paramagnetic molecules can be adsorbed at the surface and used as probes for investigating the chemical and physical properties of the materials.[26–29]

In this chapter, the Phillips based catalysts and TMI in zeotype materials in an EPR perspective are introduced. The introduction to the Phillips based catalysts is part of my work included in a book chapter.[30]

1.1 Phillips Based Systems

The Phillips catalyst was invented by J. P. Hogan and R. L. Banks in the 1950s.[31] The catalyst is a Cr-based catalyst used for ethylene polymerization and its use is so widespread that it accounts for over 40% of the high-density polyethylene (HDPE) production.[6] Despite being successfully utilized

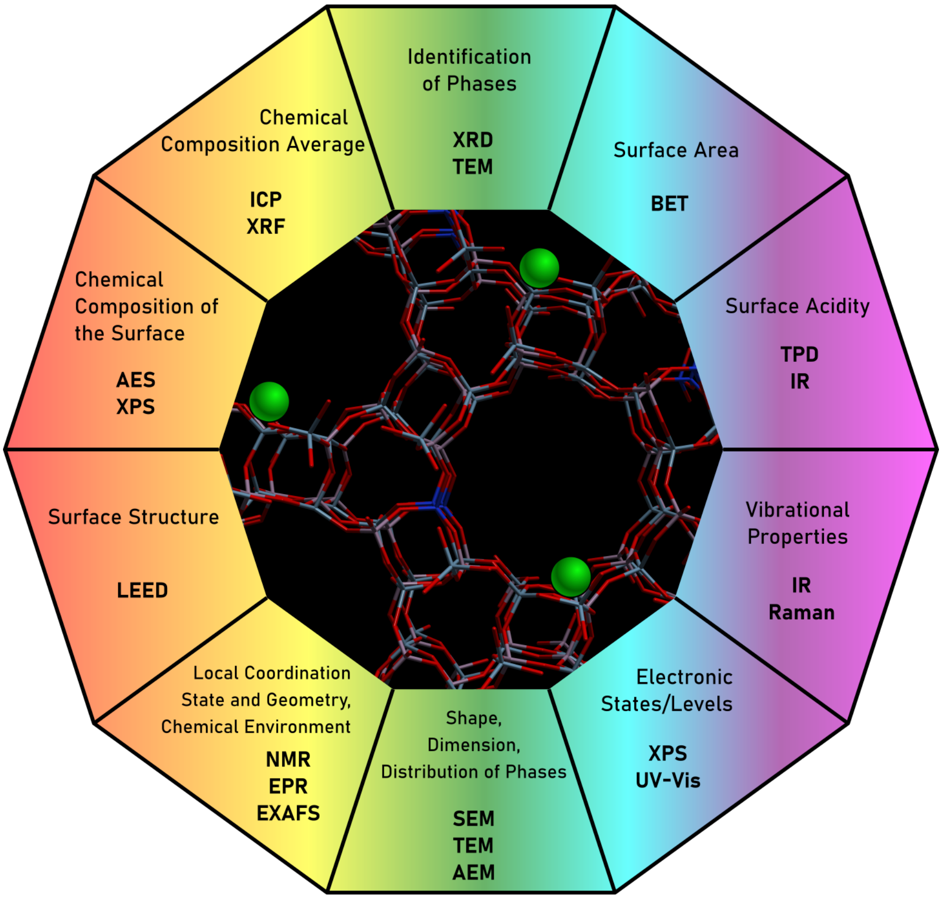
Identification of Phases
XRD
TEM
Surface Area
BET
Surface Acidity
TPD
IR
Vibrational Properties
IR
Raman
Electronic States/Levels
XPS
UV-Vis
Shape, Dimension, Distribution of Phases
SEM
TEM
AEM
Local Coordination State and Geometry, Chemical Environment
NMR
EPR
EXAFS
Surface Structure
LEED
Chemical Composition of the Surface
AES
XPS
Chemical Composition Average
ICP
XRF

Figure 1.1: The collection of characterization techniques for TMI (green balls) at surfaces.

in large scale industrial operations for the past 60 years, it may be rather surprising to learn that there are still many unanswered questions concerning the mode of operation of the catalysts.[6, 32, 33] In particular, the oxidation state and geometry of the active site are still poorly understood, whilst some of the fundamental steps involved in the polymerization mechanism remain elusive.

These questions remain unresolved for several reasons. First, only a small fraction of the Cr-sites are actually active, such that many studies have actually reported upon Cr-species that are not directly related to active sites.[6, 32] Second, the Phillips catalyst itself represents a rather complex arrangement of chemical entities, which are sensitive to the experimental conditions.[32, 33] As a result, experiments conducted in different research laboratories may have employed slightly different conditions, giving rise to slightly different distribution of centers within the catalyst. Third, most laboratory studies were conducted on high vacuum lines which often do not reproduce the experimental conditions employed in industrial applications, and therefore the observer is actually reporting on different states of the catalyst. [32, 33] In general terms, the Phillips catalysts are prepared by dispersing hexavalent chromium ions onto the surface of porous inorganic materials.[6, 33, 34] The catalyst is then activated by calcination in an oxidizing atmosphere at temperature above 600°C. After the activation step, Cr^{6+} will be the dominating Cr species, with a minor proportion of Cr^{5+} species.[35]

There are two common forms of the Phillips catalyst, namely the oxidized form and the reduced form. The oxidized form is based on the aforementioned Cr^{6+} precatalyst. It can react with ethylene at $T>100°C$, and initiate polymerization after the induction time. During the induction period, the chromium is reduced to lower oxidation state, predominantly Cr^{2+}, before forming the Cr-R active sites (for which the oxidation state is uncertain).[33] The small amount of Cr^{5+} centers (with $S = 1/2$), can be investigated by X-/Q-band EPR, and these usually reveal an axial set of g values when grafted on alumina support.[36] On the other hand, two Cr^{5+} centers with axial and rhombic g values were reported for the silica grafted material.[36, 37] Upon ethylene polymerization, high spin Cr species, characterized by signals with $g_{eff} \approx 4.3$, can also be detected. These were attributed to Cr^{3+} species ($S = 3/2$) with large zero-field interaction (*zfi*) parameters,[37] and illustrate the complexity of speciation in these catalysts.

By comparison, the reduced form of the Phillips catalyst can be obtained by further reducing the oxidized form with CO. At 350°C, the Cr^{6+} sites can be quantitatively converted to Cr^{2+}.[6, 38–40] After this reduction, the catalyst is active for polymerization with ethylene at room temperature, without an induction time. EPR investigations of these catalysts showed that only a small amount of Cr^{5+} remain as an impurity after the reduction.[37, 41, 42] The non-Kramers Cr^{2+} species ($S = 2$) was investigated using high field EPR, and was reported to have very small rhombicity for the zfs tensor.[41] Upon ethylene polymerization, two research groups reported different observations, albeit under slightly different conditions. In one case, the X-/Q-band spectra were reported to be unaltered following ethylene exposure at room temperature,[37] and assumed that no Kramers species was involved in the polymerization. However, in another study, the polymerization reaction was performed at $T = 80°C$ and the authors reported the appearance of Cr^{3+} signals, characterized by the broad linewidth, centered at $g \approx 1.98$ with axial symmetry, together with the loss from Cr^{2+} signals.[41, 42] Therefore, it was concluded that the Cr^{2+} sites were oxidized to organo-Cr^{3+} species by ethylene, which initiated the polymerization.

As described above, both forms of the Phillips catalysts require a reduction step forming the Cr^{2+}

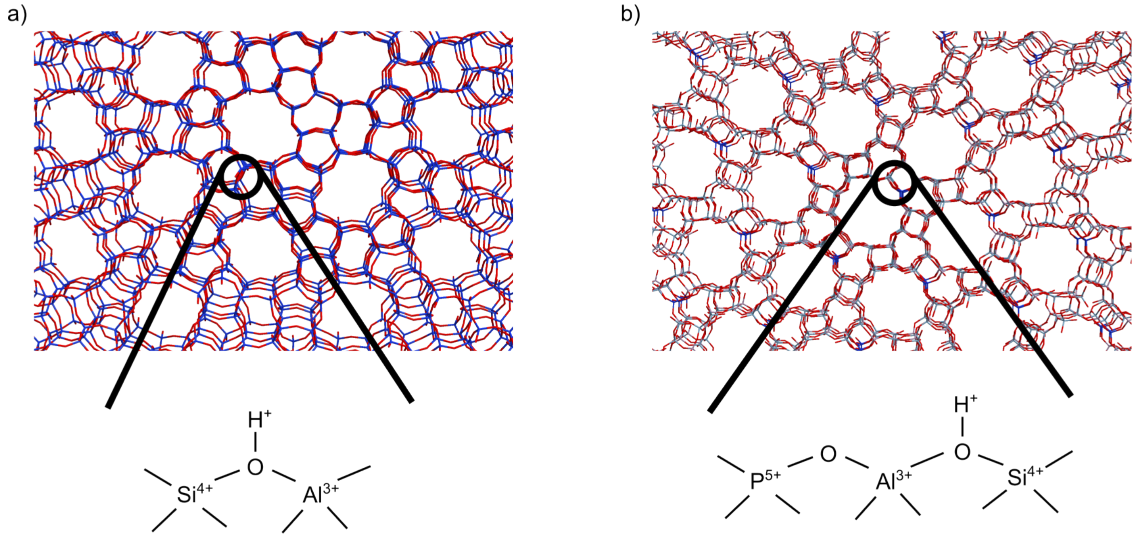

Figure 1.2: The structures of a) ZSM-5 and b) SAPO-5.

centers. The polymerization mechanism is then proposed to operate via a two electron redox process involving Cr^{2+} and Cr^{4+}, or a one electron redox process involving Cr^{2+} and Cr^{3+}. To delineate which mechanism is operative, considerable efforts in surface organometallic chemistry (SOMC) and supported homogeneous catalysis (SHC) have created systems bearing surface chromium sites with well-defined oxidation state and nuclearity on a silica-/alumina surface.[8] This is exemplified by the research from Copéret and colleagues.[43, 44] In their studies, Cr^{3+}-siloxide and Cr^{3+}-amide were grafted onto the silica surface. In the case of the Cr^{3+}-amide, an EPR signal with g_{eff} ≈2, attributed to low spin Cr^{3+} ($S = 1/2$) whilst the HYSCORE spectrum revealed strong hyperfine interaction (*hfi*) with ^{14}N indicating direct bonding of the N to the Cr. On the other hand, the grafted Cr^{3+}-siloxide produced two high spin Cr^{3+} species with g_{eff} ≈4.9 were detected in the Continuous Wave- (CW-) EPR and weakly coupled ^{29}Si identified in the HYSCORE experiment without the presence of N. In these two cases, hyperfine spectroscopy helps to elucidate the local environment of the grafted Cr^{3+} and provides evidences for the suggested structures.

Bearing in mind the limitations stated earlier, it is crucial to investigate the complex Phillips catalyst with the plethora of analytical and spectroscopic techniques, if the mechanism is to be truly understood. As shown above, EPR is one such spectroscopic technique that can provide detailed information on the local geometry of the Cr species and even the surrounding environment. Kramers species including Cr^{3+} and Cr^{5+} can be investigated at conventional microwave frequencies employed in EPR (i.e., X-/Q-band), whilst higher microwave frequencies are needed to investigate the non-Kramers species like Cr^{2+} and Cr^{4+}. The potential opportunities afforded by pulsed EPR are undoubtedly yet to be explored, but owing the complex speciation and distribution of spin active centers in these catalysts, it will always remain challenging to fully characterize the paramagnetic centers in these catalysts. Nevertheless, EPR will remain a vitally important tool in the arsenal of techniques used to study the Phillips catalysts.

1.2 TMI in Crystalline Microporous Materials

Among the many kinds of microporous materials, the best known members are zeolites, which have narrow and uniform pore size distributions resulting from their crystallographically defined pore system. Zeolites are constituted by corner-sharing tetrahedra of silicates and aluminates and form a variety of structures. The chemical composition of these materials is described by the Si/Al ratio. The Al content determines the number of extra-framework cations. This is because the presence of trivalent Al results in a negatively charged framework and the charge neutrality is achieved by extra-framework positive charges such as H^+, Na^+, etc (Fig.1.2a). Protonated zeolites are characterized by the presence of acidic (Brønsted) protons, which confer the acid character to these solids. Such acidic protons can be easily exchanged, which make it possible to introduce other types of metal ions via ion-exchange in aqueous solution. When TMI cations are introduced, redox functionalities are also inserted.

On the other hand, zeotype materials, such as the aluminophosphates (AlPO or APO) are structurally analogous to the zeolites, however, at variance with aluminosilicates, their frameworks are neutral. The materials consist of alternating tetrahedral units of phosphates and aluminates and form neutral frameworks (Fig.1.2b). In this case, the acid and redox properties can be engineered by isomorphous incorporating TMI with oxidation states from $+2$ to $+5$.[3, 4] In addition, the materials introduced with Si^{4+}, replacing isomorpously the framework Al or P, forms another category of the zeotype materials, the so-called silico-aluminophosphates (SAPO) (Fig.1.2b). These materials exhibit Brønsted acidity when the Si substitute isolated P, as a negative charge needs to be compensated by additional acid protons.[45]

As in the case of zeolites/zeotype materials, the TMIs introduced in the system are often paramagnetic and serve as perfect probe themselves. The spin states of the TMIs provide information on the oxidation states with different fingerprint signals.[46, 47] Moreover, hyperfine interaction with ^{31}P (100% abundance, $I = 1/2$) and ^{27}Al (100% abundance, $I = 5/2$) can be exploited to understand the structure of the incorporated TMI.[48–50]

1.2.1 Single Atom Catalyst

Single-site heterogeneous catalysts (SSHC) are defined as isolated active sites composed of one or more atoms dispersed on the surfaces of the supports.[1, 2] The properties of these catalysts are determined by the chemical interactions of the active sites with the supports, which are described in terms of charge transfer, orbital overlap, coordination structure, etc. Introducing TMI entities as the active sites, the aforementioned interactions can be studied with EPR spectroscopy. This section deals with the category that isolated TMIs that are atomically dispersed on zeolite/zeotype materials while the next section will focus on the SSHC with bi-metallic active sites.

For open-shell metals, the spin - and its delocalization - is central to dictating design principles for the development of new sustainable catalytic pathways.[51] In zeolites, TMIs are usually introduced via ion-exchange and end up at sites in the vicinity of framework ^{27}Al due to charge neutrality reasons. Studying the *hfi* between the TMI and the framework ^{27}Al can provide information related to the local coordination.[52–54] In zeotype materials, such as AlPO, since these materials are constituted by alternating aluminate and phosphate units, *hfi* with ^{31}P and ^{27}Al provide vital information on the location of the TMI in the materials and allow to discriminate between isomorphous substitution and extra-framework positions.[48, 55–58]

Experimentally, large enough *hfi* can be resolved in CW-EPR experiments. On the other hand, small *hfi* can be uncovered by means of hyperfine spectroscopies including Electron Nuclear Double Resonance (ENDOR), Electron Spin Echo Envelope Modulation (ESEEM), and Hyperfine Sublevel

Correlation (HYSCORE) spectroscopies.[20, 21] ENDOR experiments probe the NMR transition frequencies by means of the change of the EPR signal intensity induced by an incident radio frequency (RF) field. On the other hand. ESEEM and HYSCORE are time-domain techniques that monitor the electron spin-echo intensity modulation caused by *hfi* and nuclear quadrupolar interaction (*nqi*) over time, where the Fourier transform to the spectrum provides the nuclear frequencies of the system. Typically ENDOR is suitable for large couplings while ESEEM and HYSCORE are used for small *hfi*.

Several EPR studies using hyperfine spectroscopies have been performed on single metal sites in zeotype materials. Various studies on the SAPO systems with 3-pulse ESEEM experiments were done by Kevan and colleagues.[48, 49, 55, 56, 59] Their work focuses on the quantification of the paramagnetic nuclei in the weak interaction condition considering the relation between the 3-pulse ESEEM modulation depth, dipolar *hfi*, and the number of the equivalent nuclear species. The works covers the determination of the TMI location in the materials and investigation on the TMI interaction with adsorbed molecules such as D_2O, CD_3OH, CH_3OH, C_2D_4, etc. However, their approach is limited to small *hfi* and requires the suppression to the signals of species with large *hfi* which means lack of short range coordination information. On the other hand, HYSCORE spectroscopy, as a 2-D technique provides higher resolution to the hyperfine interactions, and is applied in some studies giving more direct evidence of the local environment. The work of Chiesa and colleagues show that Ti^{3+} is incorporated at framework Al^{3+} sites by deducing large *hfi* with ^{31}P and small *hfi* with ^{27}Al.[58] Meanwhile, in another work they identified extra-framework VO^{2+} species via simultaneous detection of large *hfi* with both ^{31}P and ^{27}Al. To determine uniquely the *hfi* and *nqi* parameters for the second coordination sphere nuclei, W-band ENDOR was demonstrated as a powerful technique.[53, 54, 60] In some cases, at the conventional X-/Q-band EPR frequencies, the anisotropy of the *hfi* might not be well-resolved due to poor orientation selection and W-band ENDOR can be a solution.

1.2.2 Bi-Metallic Catalyst

Besides the isolated TMIs dispersed on the surface where support-metal synergy is a key element to tune the reactivity and catalytic potential, the metal-metal synergy can be introduced in active sites by engineering the incorporation of 2 metal species.[61] Such systems can be achieved by combining two redox-active sites via simultaneous incorporation of two different TMI,[61, 62] which provides these materials with a peculiar bifuntional character.[2] However, so far only few reports have dealt with the use of SAPOs as supports for atomically dispersed metal catalysts, and little is known about the structures and the properties of highly dispersed bi-metallic systems.[63]

The key for the remarkable reactivity of bi-metallic dispersed species is the cooperative synergy between the two metal sites enabled by the optimal coordination structure enforced by the framework. This in turn is often a direct reflection of the synthetic protocols and specific reaction conditions. In fact, not only different oxidation states can be adopted by the metals, but also, they can in principle occupy both framework and extra-framework positions and distinguishing between the two situations if often not easy.

Clearly, subtle control of these single atom or bimetallic catalysts requires reliable characterization methods allowing to monitor in detail the local structural environment and the chemistry (catalytic potential) of the dopant ions.

In the work of Paterson and colleagues, they reported the enhanced activity of the bimetallic CoTiAlPO-5 catalyst compared to the corresponding monometallic analogues for olefin epoxidation.[62] While the work of Leithall et al. reported the VTiAlPO-5 bimetallic catalyst with higher activity than the TiAlPO-5 and VAlPO-5.[61] In the latter case, the presence of bimetallic sites was validated with EPR spectroscopy based on their redox properties and interaction with the framework.[64]

Bibliography

(1) Kaiser, S. K.; Chen, Z.; Faust Akl, D.; Mitchell, S.; Pérez-Ramírez, J. *Chemical Reviews* **2020**, *120*, 11703–11809 (cited on pages 1, 5).

(2) Thomas, J. M.; Raja, R.; Lewis, D. W. *Angewandte Chemie - International Edition* **2005**, *44*, 6456–6482 (cited on pages 1, 5, 6).

(3) Hartmann, M.; Kevan, L. *Research on Chemical Intermediates* **2002**, *28*, 625–695 (cited on pages 1, 5).

(4) Hartmann, M.; Kevan, L. *Chemical Reviews* **1999**, *99*, 635–663 (cited on pages 1, 5).

(5) Dyrek, K.; Che, M. *Chemical Reviews* **1997**, *97*, 305–332 (cited on page 1).

(6) McDaniel, M. P. In *Advances in Catalysis*, 1st edition; Elsevier Inc.: 2010; Vol. 53, pp 123–606 (cited on pages 1, 3).

(7) Weckhuysen, B. M.; Wachs, I. E.; Schoonheydt, R. A. *Chemical Reviews* **1996**, *96*, 3327–3349 (cited on page 1).

(8) Copéret, C.; Allouche, F.; Chan, K. W.; Conley, M. P.; Delley, M. F.; Fedorov, A.; Moroz, I. B.; Mougel, V.; Pucino, M.; Searles, K.; Yamamoto, K.; Zhizhko, P. A. *Angewandte Chemie - International Edition* **2018**, *57*, 6398–6440 (cited on pages 1, 4).

(9) Bruzzese, P. C.; Salvadori, E.; Jäger, S.; Hartmann, M.; Civalleri, B.; Pöppl, A.; Chiesa, M. *Nature Communications 2021 12:1* **2021**, *12*, 1–13 (cited on page 1).

(10) Goursot, A.; Coq, B.; Fajula, F. *Journal of Catalysis* **2003**, *216*, 324–332 (cited on page 1).

(11) Corma, A.; García, H.; Llabrés I Xamena, F. X. *Chemical Reviews* **2010**, *110*, 4606–4655 (cited on page 1).

(12) Furukawa, H.; Cordova, K. E.; O'Keeffe, M.; Yaghi, O. M. *Science* **2013**, *341*, DOI: `10.1126/science.1230444` (cited on page 1).

(13) Babucci, M.; Guntida, A.; Gates, B. C. *Chemical Reviews* **2020**, *120*, 11956–11985 (cited on page 1).

(14) *Pure and Applied Chemistry* **1976**, *46*, 71–90 (cited on page 1).

(15) Zecchina, A.; Groppo, E.; Bordiga, S.; Zecchina, A.; Groppo, E.; Bordiga, S. *Chemistry – A European Journal* **2007**, *13*, 2440–2460 (cited on page 1).

(16) Gast, P.; Groenen, E. J. In *eMagRes*; Major Reference Works; John Wiley & Sons, Ltd: Chichester, UK, 2016, pp 1435–1444 (cited on page 1).

(17) Telser, J. *eMagRes* **2017**, *6*, 207–234 (cited on page 1).

(18) Chiesa, M.; Giamello, E.; Livraghi, S.; Paganini, M. C.; Polliotto, V.; Salvadori, E. *Journal of Physics: Condensed Matter* **2019**, *31*, 444001 (cited on page 1).

(19) Bennati, M. *eMagRes* **2017**, *6*, 271–282 (cited on page 1).

(20) Van Doorslaer, S. *eMagRes* **2017**, *6*, 51–70 (cited on pages 1, 6).

(21) Harmer, J. R. In *eMagRes*; John Wiley & Sons, Ltd: Chichester, UK, 2016, pp 1493–1514 (cited on pages 1, 6).

(22) Bruzzese, P. C.; Salvadori, E.; Civalleri, B.; Jäger, S.; Hartmann, M.; Pöppl, A.; Chiesa, M. *Journal of the American Chemical Society* **2022**, *144*, 13079–13083 (cited on page 1).

(23) Jeschke, G. *eMagRes* **2016**, *5*, 1459–1476 (cited on page 1).

(24) Borbat, P. P.; Freed, J. H. In *eMagRes*; John Wiley & Sons, Ltd: Chichester, UK, 2017, pp 465–494 (cited on page 1).

(25) Salvadori, E.; Fusco, E.; Chiesa, M. *Journal of Physical Chemistry Letters* **2022**, *13*, 1283–1289 (cited on page 1).

(26) Che, M.; Tench, A. In *Advances in Catalysis*; C, 1983; Vol. 32, pp 1–148 (cited on page 1).

(27) Chiesa, M.; Giamello, E.; Che, M. *Chemical Reviews* **2010**, *110*, 1320–1347 (cited on page 1).

(28) Pöppl, A.; Rudolf, T.; Michel, D. *Journal of the American Chemical Society* **1998**, *120*, 4879–4880 (cited on page 1).

(29) Pöppl, A.; Rudolf, T.; Manikandan, P.; Goldfarb, D. *Journal of the American Chemical Society* **2000**, *122*, 10194–10200 (cited on page 1).

(30) Bracci, M.; Bruzzese, P. C.; Famulari, A.; Fioco, D.; Guidetti, A.; Liao, Y.-K.; Podvorica, L.; Rezayi, S. F.; Serra, I.; Thangavel, K.; Murphy, D. M. In *Electron Paramagnetic Resonance: Volume 27*; The Royal Society of Chemistry: 2020; Vol. 27, pp 1–46 (cited on page 1).

(31) Hogan, J. P.; Banks, R. L. Polymers and production thereof US Patent, 2,825,721, 1958 (cited on page 1).

(32) Weckhuysen, B. M.; Schoonheydt, R. A. *Catalysis Today* **1999**, *51*, 223–232 (cited on page 3).

(33) Groppo, E.; Martino, G. A.; Piovano, A.; Barzan, C. *ACS Catalysis* **2018**, *8*, 10846–10863 (cited on page 3).

(34) McDaniel, M. In *Advances in Catalysis*; C; Academic Press: 1985; Vol. 33, pp 47–98 (cited on page 3).

(35) Weckhuysen, B. M.; De Ridder, L. M.; Grobet, P. J.; Schoonheydt, R. A. *Journal of physical chemistry* **1995**, *99*, 320–326 (cited on page 3).

(36) Weckhuysen, B. M.; Schoonheydt, R. A.; Mabbs, F. E.; Collison, D. *Journal of the Chemical Society - Faraday Transactions* **1996**, *92*, 2431–2436 (cited on page 3).

(37) Morra, E.; Martino, G. A.; Piovano, A.; Barzan, C.; Groppo, E.; Chiesa, M. *Journal of Physical Chemistry C* **2018**, *122*, 21531–21536 (cited on page 3).

(38) Zecchina, A.; Garrone, E.; Ghiotti, G.; Coluccia, S. *Journal of Physical Chemistry* **1975**, *79*, 972–978 (cited on page 3).

(39) Krauss, v. H.; Stach, H. *Inorganic and Nuclear Chemistry Letters* **1968**, *4*, 393–397 (cited on page 3).

(40) Krauss, H. L.; Stach, H. *Zeitschrift für anorganische und allgemeine Chemie* **1969**, *366*, 34–42 (cited on page 3).

(41) Brown, C. et al. *ACS Catalysis* **2015**, *5*, 5574–5583 (cited on page 3).

(42) Brown, C. et al. *ACS Catalysis* **2017**, *7*, 7442–7455 (cited on page 3).

(43) Delley, M. F.; Núñez-Zarur, F.; Conley, M. P.; Comas-Vives, A.; Siddiqi, G.; Norsic, S.; Monteil, V.; Safonova, O. V.; Copéret, C. *Proceedings of the National Academy of Sciences of the United States of America* **2015**, *112*, E4505 (cited on page 4).

(44) Delley, M. F.; Lapadula, G.; Núñez-Zarur, F.; Comas-Vives, A.; Kalendra, V.; Jeschke, G.; Baabe, D.; Walter, M. D.; Rossini, A. J.; Lesage, A.; Emsley, L.; Maury, O.; Copéret, C. *Journal of the American Chemical Society* **2017**, *139*, 8855–8867 (cited on page 4).

(45) Sastre, G.; Lewis, D. W.; Richard, C.; Catlow, A. *Journal of Physical Chemistry B* **1997**, *101*, 5249–5262 (cited on page 5).

(46) Weckhuysen, B. M.; Schoonheydt, R. A. *Zeolites* **1994**, *14*, 360–366 (cited on page 5).

(47) Padlyak, B. V.; Kornatowski, J.; Zadrozna, G.; Rozwadowski, M.; Gutsze, A. *Journal of Physical Chemistry A* **2000**, *104*, 11842–11843 (cited on page 5).

(48) Chen, X.; Kevan, L. *Journal of the American Chemical Society* **1991**, *113*, 2861–2865 (cited on pages 5, 6).

(49) Zhu, Z.; Kevan, L. *Physical Chemistry Chemical Physics* **1999**, *1*, 199–206 (cited on pages 5, 6).

(50) Arieli, D.; Vaughan, D. E.; Strohmaier, K. G.; Goldfarb, D. *Journal of the American Chemical Society* **1999**, *121*, 6028–6032 (cited on page 5).

(51) Nandy, A.; Kulik, H. J. *ACS Catalysis* **2020**, *10*, 15033–15047 (cited on page 5).

(52) Goldfarb, D.; Kevan, L. *Journal of Magnetic Resonance (1969)* **1989**, *82*, 270–289 (cited on page 5).

(53) Goldfarb, D. *Physical Chemistry Chemical Physics* **2006**, *8*, 2325–2343 (cited on pages 5, 6).

(54) Carl, P. J.; Vauahan, D. E.; Goldfarb, D. *Journal of the American Chemical Society* **2006**, *128*, 7160–7161 (cited on pages 5, 6).

(55) Lee, C. W.; Chen, X.; Kevan, L. *The Journal of Physical Chemistry* **1992**, *96*, 357–361 (cited on pages 5, 6).

(56) Lee, C. W.; Saint-Pierre, T.; Azuma, N.; Kevan, L. *The Journal of Physical Chemistry* **1993**, *97*, 11811–11814 (cited on pages 5, 6).

(57) Nagarajan, V.; Rings, D.; Moschkowitz, L.; Hartmann, M.; Pöppl, A. *Chemistry Letters* **2005**, *34*, 1614–1615 (cited on page 5).

(58) Maurelli, S.; Vishnuvarthan, M.; Chiesa, M.; Berlier, G.; Van Doorslaer, S. *Journal of the American Chemical Society* **2011**, *133*, 7340–7343 (cited on pages 5, 6).

(59) Zhu, Z.; Wasowicz, T.; Kevan, L. *Electron Spin Resonance and Electron Spin Echo Modulation Spectroscopic Studies of Chromium Ion Location and Adsorbate Interactions in Calcined CrAPSO-11*; technical report; 1997 (cited on page 6).

(60) Goldfarb, D.; Strohmaier, K. G.; Vaughan, D. E.; Thomann, H.; Poluektov, O. G.; Schmidt, J. *Journal of the American Chemical Society* **1996**, *118*, 4665–4671 (cited on page 6).

(61) Leithall, R. M.; Shetti, V. N.; Maurelli, S.; Chiesa, M.; Gianotti, E.; Raja, R. *Journal of the American Chemical Society* **2013**, *135*, 2915–2918 (cited on pages 6, 7).

(62) Paterson, J.; Potter, M.; Gianotti, E.; Raja, R. *Chemical Communications* **2011**, *47*, 517–519 (cited on pages 6, 7).

(63) Perez-Aguilar, J. E.; Chen, C. Y.; Hughes, J. T.; Fang, C. Y.; Gates, B. C. *Journal of the American Chemical Society* **2020**, *142*, 11474–11485 (cited on page 6).

(64) Maurelli, S.; Chiesa, M.; Giamello, E.; Leithall, R. M.; Raja, R. *Chemical Communications* **2012**, *48*, 8700–8702 (cited on page 7).

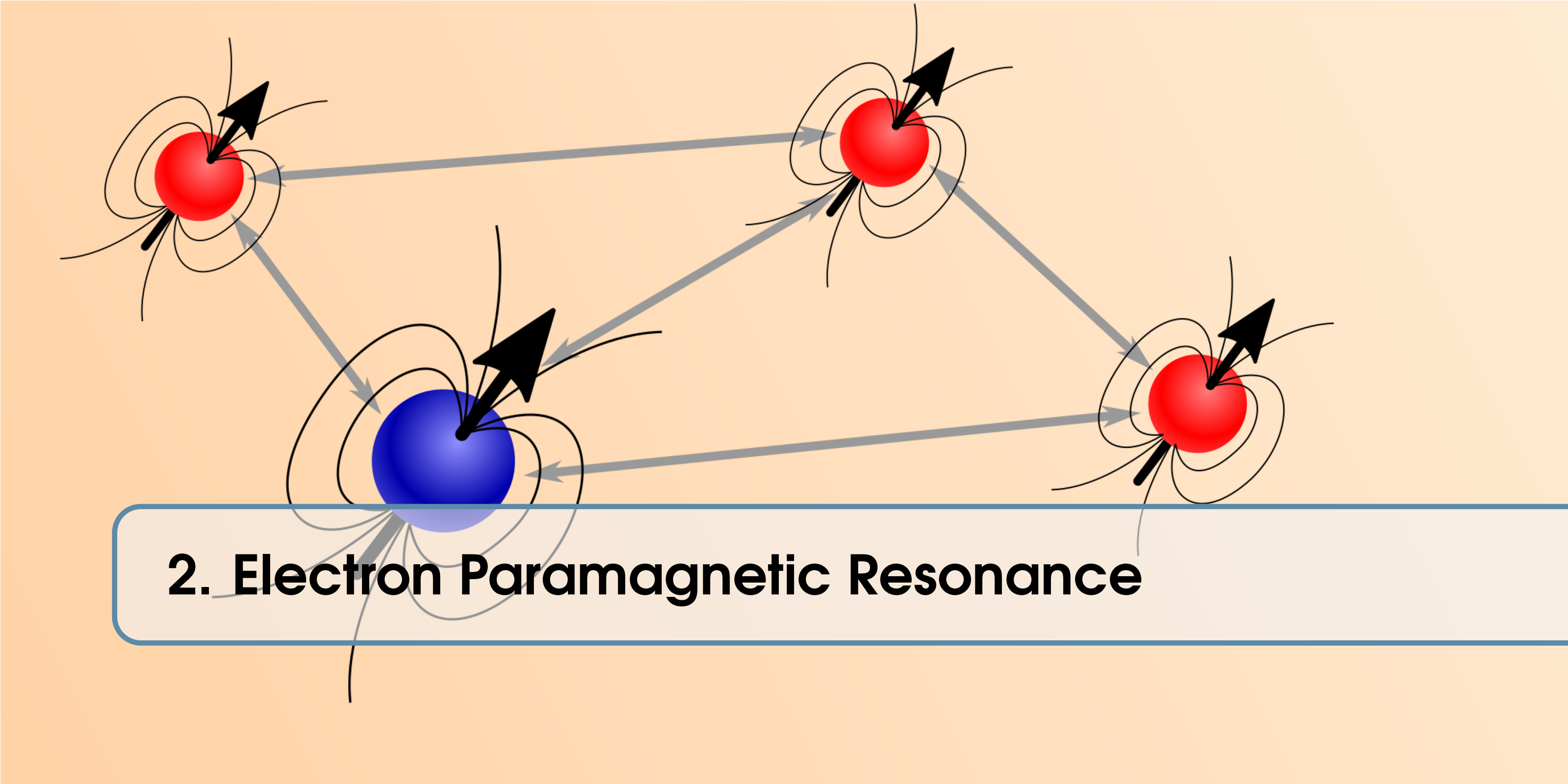

2. Electron Paramagnetic Resonance

In this chapter, the basic theory regarding the principles of the Electron Paramagnetic Resonance (EPR) spectroscopy; and the EPR experiments used in this work will be introduced.

EPR spectroscopy was discovered more than 70 years ago by E. Zavoisky at Kazan University in 1945, before the first nuclear magnetic resonance (NMR) experiments.[1] Taken into account the discovery of the Zeeman effect in 1890s,[2, 3] the Stern-Gerlach experiment in 1920s,[4–6] and the postulate of a quantized angular momentum, spin, of electron by Uhlenbeck and Goudsmit later,[7, 8] the history of the development of the quantum physics theories can be traced back for another 50 years. Thanks to the availability of microwave components and the development in the fast digital electronics in the recent decades, now many different methods, instruments, and applications are at hand.[9]

The magnitude of the interactions between electron spins and nuclear spins span across a wide range of frequencies.(Fig.2.1) By selecting the proper methods, including different microwave frequencies, in continuous wave (CW) EPR and pulsed EPR, one might be able to disentangle the information from complex paramagnetic systems.

2.1 Continuous Wave EPR

Classically, a magnetic dipole $\mathbf{m}$ placed in a static magnetic field $\mathbf{B}$ has the potential energy

$$U = -\mathbf{m} \cdot \mathbf{B}. \tag{2.1}$$

Eq. 2.1 describes how the potential energy of the magnetic dipole varies according to the exerted magnetic field. In quantum physics, a free electron has the magnetic dipole moment

$$\boldsymbol{\mu_S} = -g_e \beta_B \mathbf{S} \tag{2.2}$$

associated to its spin angular momentum $\mathbf{S}$ with the g-factor g_e and Bohr magneton β_B. Therefore, the Hamiltonian of an electron in a static magnetic field can be written as

$$\begin{aligned} \mathcal{H} &= -\boldsymbol{\mu_S} \cdot \mathbf{B} \\ &= g_e \beta_B \mathbf{S} \cdot \mathbf{B}. \end{aligned} \tag{2.3}$$

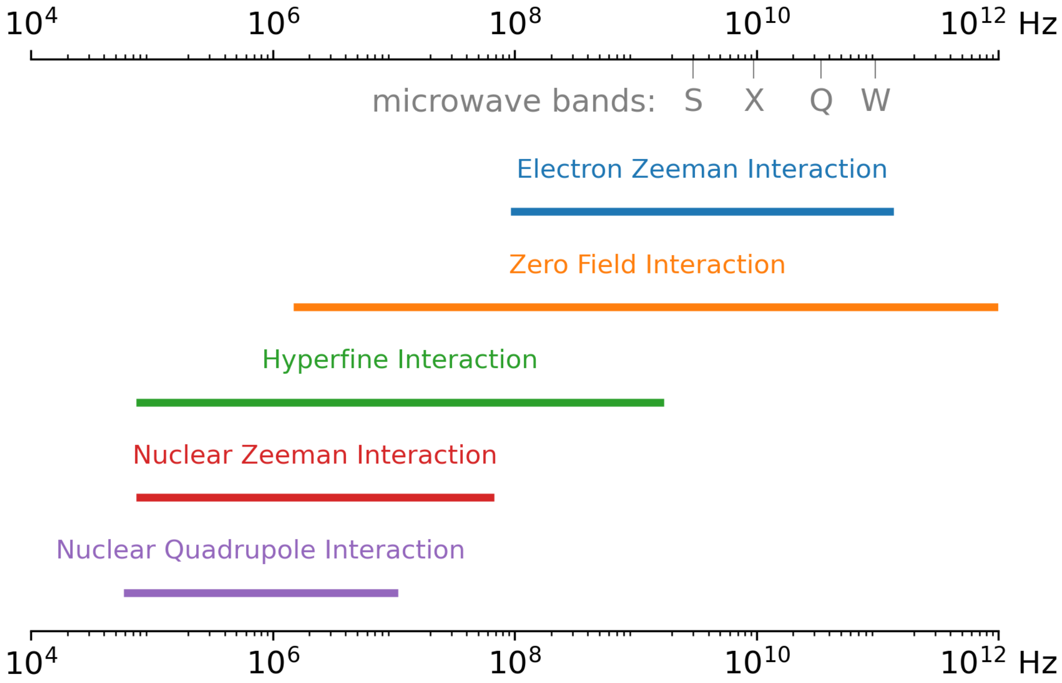

Figure 2.1: The diagram of the magnitudes of different spin interactions.[10]

The degenerate spin states are split under an external static field.

In CW EPR, this mechanism is exploited by sending continuously the microwave of a certain frequency (e.g. 9.5 GHz at X-band) at the sample in the resonator. Then the external magnetic field is swept through a designated range and as soon as the energy difference of the split spin states meets the microwave energy of the photon, a spin transition takes place and the microwave is absorbed.(Fig.2.2a)

In practice, the absorption is observed as the change of the quality factor (Q-value) of the resonator. The Q-value is the efficiency of the resonator and can be formulated as the energy stored in the cavity over the dissipated energy

$$Q = 2\pi \times \frac{\text{stored energy}}{\text{dissipated energy}} \tag{2.4}$$

or alternatively

$$Q = \frac{\nu_{\text{res}}}{\Delta\nu} \tag{2.5}$$

with the resonance frequency (ν_{res}) at which minimum reflection from the cavity is detected, and the half width of the frequency of the absorbed microwave ($\Delta\nu$).[11](Fig.2.2b) When the transition condition is met and the microwave absorbed by the sample, the Q-value of the resonator is decreased. This change is recorded by the spectrometer as the signal.

To increase sensitivity of the spectrometer, a field modulation (ΔB_0) is applied when sweeping the external field. At each field position, it quickly modulates the field in a sine function. The EPR signal ($\mathbf{I}$) is recorded as the difference of the Q-value from the part where the field modulation is applied.(Fig.2.2c) As a result, the spectrum appears as a derivative of the microwave absorption.(Fig.2.2d)

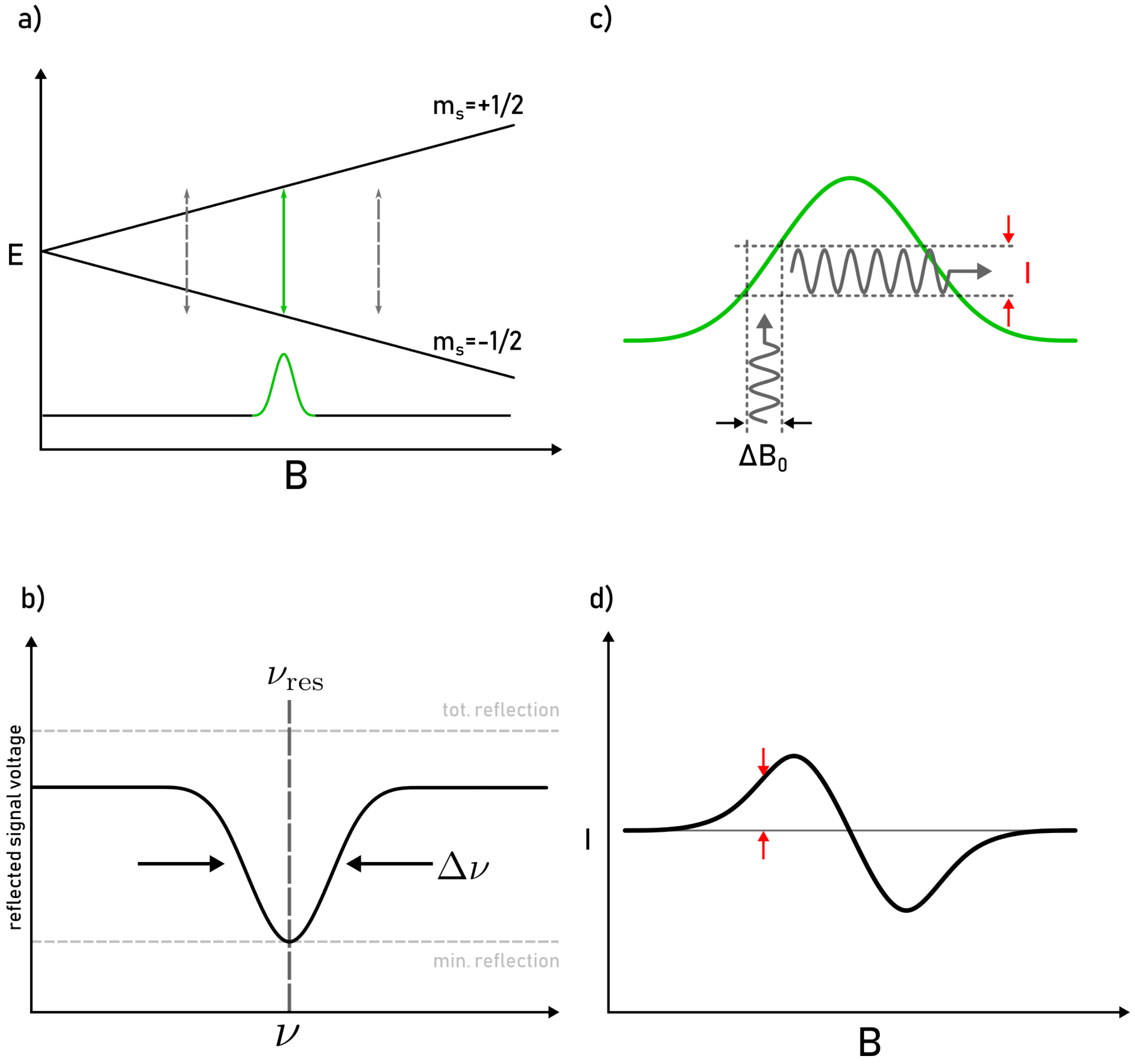
a)
m_s=+1/2
E
m_s=-1/2
B
c)
I
ΔB_0
b)
ν_{res}
tot. reflection
reflected signal voltage
$\Delta\nu$
min. reflection
ν
d)
I
B

Figure 2.2: The scheme diagrams of the CW-EPR mechanism. a) The diagram indicates the transition takes place at the field position where the splitting of the spin states meets the microwave frequency. b) The diagram shows how the Q-value is determined. c) The diagram shows how the application of field modulation turns the absorption of microwave into signal intensity. d) The diagram shows how the CW EPR spectrum appears in the derivative of an absorption spectrum with the signal intensity indicated in c).

Due to the order of magnitude of the interactions (Fig.2.1) and/or the line width of the spectrum, not all interactions related to the terms of the spin Hamiltonian can be well resolved in CW EPR. Pulsed EPR techniques, by applying microwave pulses to manipulate the electron magnetization, allow the detection of different spin interactions. By applying microwave pulse sequences in the ns to μs time regime, pulse EPR can provide sub-MHz resolution. The basic theory to describe pulsed EPR will be introduced in section 2.3 and some technique will be introduced in section 2.4.

2.2 Spin Hamiltonian

As shown in Fig.2.1, there are more interactions involved in the Hamiltonian of an electron spin originated not only from the external magnetic field but also the internal field of the spin system. Such interactions can provide information with regard to the local symmetry, structural information, and distribution of the target paramagnetic species. It is presented as different terms in the spin Hamiltonian

$$\begin{aligned}\mathcal{H} &= \mathcal{H}_{EZ} + \mathcal{H}_{ZFI} + \mathcal{H}_{NZ} + \mathcal{H}_{HFI} + \mathcal{H}_{NQI} \\ &= \beta_B \mathbf{B} \cdot \boldsymbol{g} \cdot \mathbf{S} + \mathbf{S} \cdot \mathbf{D} \cdot \mathbf{S} - \beta_n \sum_{k=1}^{m} g_{n,k} \cdot \mathbf{B} \cdot \mathbf{I}_k \\ &+ \sum_{k=1}^{m} \mathbf{S} \cdot \mathbf{A} \cdot \mathbf{I}_k + \sum_{I_k > 1/2} \mathbf{I}_k \cdot \mathbf{P}_k \cdot \mathbf{I}_k\end{aligned} \tag{2.6}$$

derived by Abragam and Pryce.[12] In Eq. 2.6, each term indicates the different interactions; $\mathcal{H}_{EZ}$: electron Zeeman interaction; $\mathcal{H}_{ZFI}$: zero-field interaction; $\mathcal{H}_{NZ}$: nuclear Zeeman interaction; $\mathcal{H}_{HFI}$: hyperfine interaction; $\mathcal{H}_{NQI}$: nuclear quadrupole interaction. In the following subsections, the details of each term of spin Hamiltonian will be introduced.

2.2.1 Electron Zeeman Interaction

In the previous section, spin Hamiltonian on a free electron associated to its magnetic dipole moment is discussed. However, for an electron in a material, it is also important to take into account the effect of the orbital angular momentum **L**. The spin Hamiltonian then becomes

$$\mathcal{H} = \beta_B \mathbf{B} \cdot (\mathbf{L} + g_e \mathbf{S}) + \lambda \mathbf{L} \cdot \mathbf{S}. \tag{2.7}$$

One might expect the effect of the orbital angular momentum would drop because for non-degenerate orbital states, the orbital angular momentum is quenched $\langle \mathbf{L} \rangle = 0$. However, by applying second order perturbation theory to the spin Hamiltonian, the spin Hamiltonian can be written as

$$\mathcal{H} = \beta_B \mathbf{B} \cdot (g_e \mathbf{1} + 2\lambda \mathbf{\Lambda}) \cdot \mathbf{S} + \lambda^2 \mathbf{S} \cdot \mathbf{\Lambda} \cdot \mathbf{S} \tag{2.8}$$

with

$$\Lambda_{ij} = \sum_{n \neq 0} \frac{\langle \psi_0 | \mathbf{L}_i | \psi_n \rangle \langle \psi_n | \mathbf{L}_j | \psi_0 \rangle}{E_0 - E_n} \text{ for } i, j = x, y, z \tag{2.9}$$

for $|\psi_0\rangle$ the ground state eigenfunction with eigenenergy E_0, and $|\psi_n\rangle$ the n^{th} excited state eigenfunction with eigenenergy E_n.[13–15] Fig.2.3 shows the scheme of an example of the tetragonal distortion for tetrahedral coordinate d-orbital,[14] where the only non-zero contributions are

$$\Lambda_{xx(yy)} = \frac{\langle z^2 | \mathbf{L}_{x(y)} | yz(xz) \rangle \langle yz(xz) | \mathbf{L}_{x(y)} | z^2 \rangle}{\Delta} \tag{2.10}$$

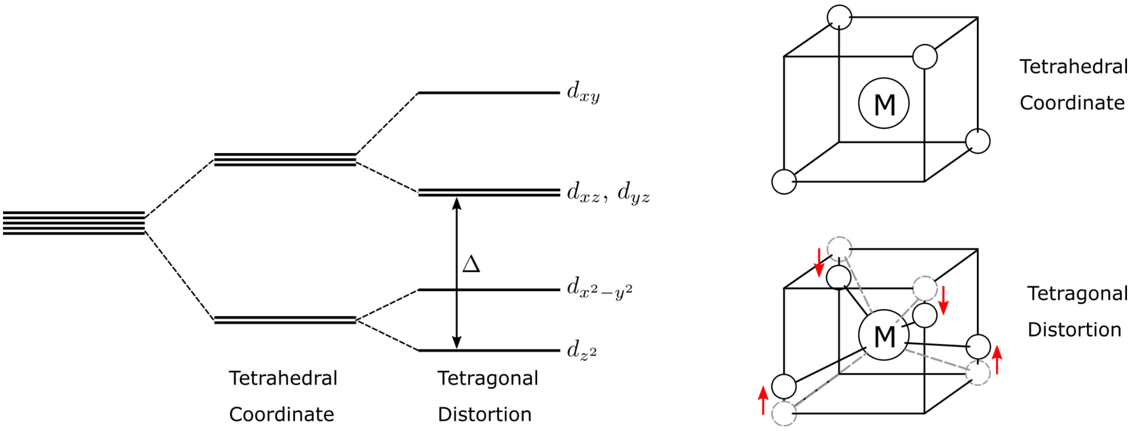

Figure 2.3: The scheme of spin-orbit coupling effect on the tetragonal distortion for the tetrahedral coordinate d-orbital.[14]

where $\Delta = E_{z^2} - E_{yz,xz}$. The first two terms of Eq. 2.8 is the corrected electron Zeeman interaction in Eq. 2.6

$$\mathcal{H}_{EZ} = \beta_B \mathbf{B} \cdot \boldsymbol{g} \cdot \mathbf{S} \tag{2.11}$$

with the g-tensor

$$\boldsymbol{g} = g_e \mathbf{1} + 2\lambda \boldsymbol{\Lambda} \tag{2.12}$$

whereas the last term represents the zero-field interaction which will be elaborated in the next section.

The anisotropy of the g-tensor therefore represents the distortion to the symmetry of the paramagnetic center. In general, the g-tensors are separated in three cases depending on the principle values of the g-tensors:

$$\begin{cases} g_{xx} = g_{yy} = g_{zz} & \text{for cubic } g\text{-tensor} \\ g_{xx} = g_{yy} = g_{\perp} \neq g_{zz} = g_{\parallel} & \text{for axial } g\text{-tensor} \\ g_{xx} \neq g_{yy} \neq g_{zz} & \text{for rhombic } g\text{-tensor} \end{cases}$$

The resonance field of an orientation of the paramagnetic center in dependence on the external field is

$$B_{res}(\theta, \phi) = \frac{h\nu_{mw}}{\beta_B \sqrt{(g_{xx}\cos\theta\sin\phi)^2 + (g_{yy}\sin\theta\sin\phi)^2 + (g_{zz}\cos\phi)^2}} \tag{2.13}$$

with ϕ the polar angle, the angle between the vector and the z-axis, and θ the azimuthal angle, the angle between the projection of the vector on the xy-plane and the x-axis. For powder samples, one might assume a homogeneous distribution of all possible orientations. Therefore, the absorption intensity is the sum of all possible orientation at the field position where transitions takes place. This can be interpreted as the surface area of the orientations on a sphere. It is shown in Fig.2.4 for the examples of an axial g-tensor and a rhombic g-tensor. Fig.2.4a,b show the absorption and first derivative spectrum with the spheres showing the orientation selection at each field positions corresponding to the different principle g-values. Fig.2.4c,d show the dependence of B_{res} on the polar angle ϕ.

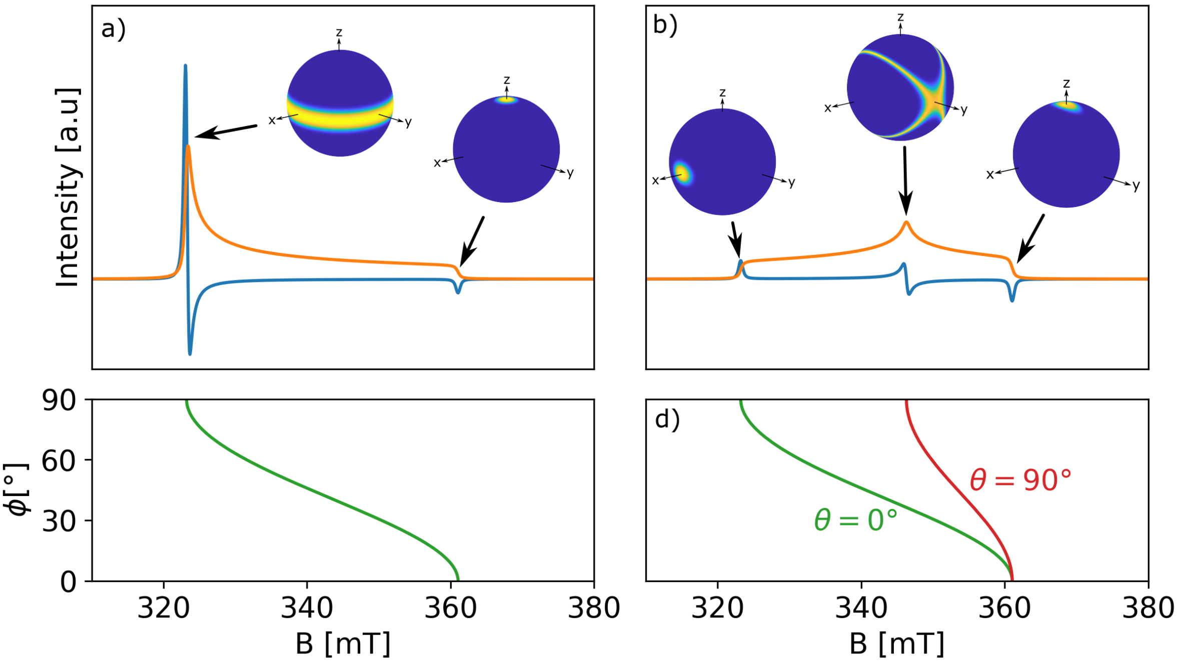

Figure 2.4: The powder spectra for axial and rhombic g-tensors. a) The absorption (orange line) and first derivative (blue line) spectrum of an axial case g-tensor with $g_\perp = 2.1$, $g_\| = 1.88$ and $\omega_{mw} = 9.5$ GHz, and b) the ϕ-dependent resonance field for arbitrary θ. c) The absorption (orange line) and first derivative (blue line) spectrum of a rhombic case g-tensor with $g_{xx} = 2.1$, $g_{yy} = 1.96$, $g_{zz} = 1.88$, and d) the ϕ-dependent resonance field for $\theta = 0°$ and $90°$. The yellow areas on the spheres represent the orientations that the transitions take place at the indicated field positions.

2.2.2 Zero Field Interaction

For spin systems with more than one unpaired electron ($S > 1/2$), one also needs to consider the interactions between the electron spins. These interactions can lead to the degeneracy of the spin states partially lifted without the external field. It is therefore called the zero-field interaction(*zfi*). There are two different types of interaction that can take part in *zfi*, the spin-orbit coupling (as shown the last term in Eq. 2.8) and the spin-spin coupling. However, typically spin-orbit coupling dominates in TMIs and spin-spin coupling is less prominent.[14, 16] The following description for *zfi* will be focused on the spin-orbit interaction as the high spin paramagnetic species related to this work are Cr^{n+} for n = 2,3,4.

The spin Hamiltonian for *zfi* can be written from the second term in Eq. 2.7 as

$$\mathcal{H}_{zfi} = \lambda^2 \mathbf{S} \cdot \mathbf{\Lambda} \cdot \mathbf{S} = \mathbf{S} \cdot \mathbf{D} \cdot \mathbf{S} \tag{2.14}$$

with the zero-field interaction tensor $\mathbf{D}$. For $S < \frac{5}{2}$ systems, it is more commonly rewritten as

$$\mathcal{H}_{zfi} = D(S_z^2 - \frac{1}{3}\mathbf{S}^2) + E(S_x^2 - S_y^2) \tag{2.15}$$

with

$$D = D_{zz} - \frac{1}{2}(D_{xx} - D_{yy}) = \frac{3}{2}D_{zz} \tag{2.16}$$

$$E = \frac{1}{2}(D_{xx} - D_{yy}) \tag{2.17}$$

for D_{ii} ($i = x, y, z$) the principle axis components of the *zfi* tensor $\mathbf{D}$. For $S > \frac{5}{2}$ systems, higher order terms need to be considered for *zfi*.[14, 16] Here, the D-value describes the distortion along the principle z-axis, with $D > 0$ for compression and $D < 0$ for elongation.[16] Whereas the E-value indicates rhombicity, with orthorhombic distortion described by $0 < E/D < \frac{1}{3}$.

Not all high spin systems are easy to investigate at conventional EPR frequencies (X-/Q-band frequencies). For half-integer spins ($S = \frac{1}{2}$, $\frac{3}{2}$, $\frac{5}{2}$, etc), they are typically called the Kramers, while the integer spins (S = 1, 2, 3, etc) are called the non-Kramers. The Kramers retain at least a two-fold degeneracy of the Kramers doublets ($m_S = \pm\frac{1}{2}, \pm\frac{3}{2}, \pm\frac{5}{2}$, etc) at zero-field regardless the magnitude of the interaction. This guarantees at least one transition to be observed. On the other hand, the spin states of non-Kramers don't always retain degeneracy at zero-field.[14, 16] (Fig.2.5) As a result, when the *zfi* becomes too much larger than the microwave frequency, there might be no transition to be observed. This is why the non-Kramers are often refered as the "EPR-silent" species.

2.2.3 Nuclear Zeeman Interaction

The nuclear Zeeman interaction, as shown in Eq. 2.6, is written as

$$\mathcal{H}_{NZ} = -\beta_n \sum_{k=1}^{m} g_{n,k} \cdot \mathbf{B} \cdot \mathbf{I}_k. \tag{2.18}$$

As each paramagnetic isotope has its own characteristic nuclear g-factor $\boldsymbol{g}_n$ (Tab. 2.1), even though the nuclear Zeeman interaction does not influence the CW-EPR spectrum in the first order, it allows distinguishing the different nuclei observed in spectra of hyperfine spectroscopy (e.g. HYSCORE, etc).

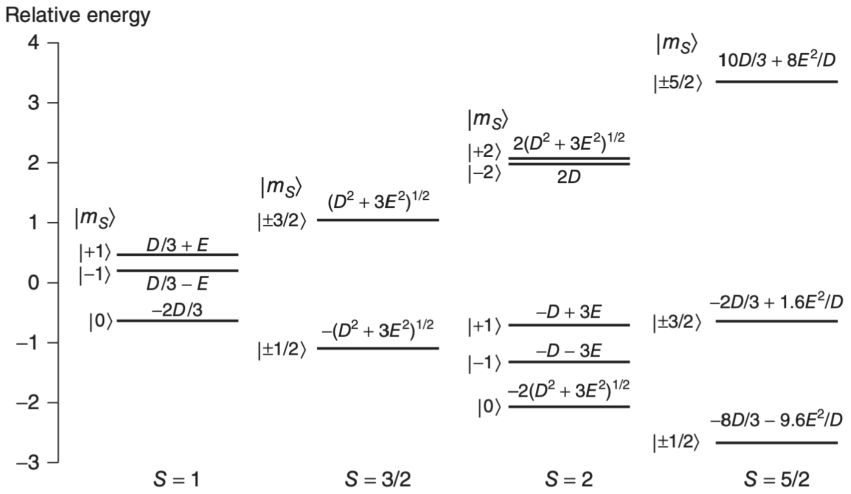
Relative energy
4
3
2
1
0
−1
−2
−3
$|m_S\rangle$
$|+1\rangle$ $D/3 + E$
$|-1\rangle$ $D/3 - E$
$|0\rangle$ $-2D/3$
$|m_S\rangle$
$|\pm3/2\rangle$ $(D^2 + 3E^2)^{1/2}$
$|\pm1/2\rangle$ $-(D^2 + 3E^2)^{1/2}$
$|m_S\rangle$
$|+2\rangle$ $2(D^2 + 3E^2)^{1/2}$
$|-2\rangle$ $2D$
$|+1\rangle$ $-D + 3E$
$|-1\rangle$ $-D - 3E$
$|0\rangle$ $-2(D^2 + 3E^2)^{1/2}$
$|m_S\rangle$
$|\pm5/2\rangle$ $10D/3 + 8E^2/D$
$|\pm3/2\rangle$ $-2D/3 + 1.6E^2/D$
$|\pm1/2\rangle$ $-8D/3 - 9.6E^2/D$
$S = 1$
$S = 3/2$
$S = 2$
$S = 5/2$

Figure 2.5: The *zfi* diagram for different spins at zero-field. Energy in units of D-value and *zfi* set to be rhombic with $|E/D| = 0.1$. For $S = 1, \frac{3}{2}, 2$ the energies are exact and second-order perturbation theory is applied for $S = \frac{5}{2}$.[16] Reproduced with permission from John Wiley & Sons, Ltd. eMagRes (2017). Copyright 2017, John Wiley & Sons, Ltd.

Isotope	Nuclear Spin I	Nuclear g-factor g_n	Natural Abundance [%]
^{1}H	1/2	+5.58569468	99.985
^{14}N	1	+0.403761	99.632
^{27}Al	5/2	+1.4566	100
^{29}Si	1/2	-1.11058	4.6832
^{31}P	1/2	+2.2632	100
^{51}V	7/2	+1.47106	99.75
^{53}Cr	3/2	-0.31636	9.501
^{95}Mo	5/2	-0.3657	15.92
^{97}Mo	5/2	-0.3734	9.55

Table 2.1: The g-factors of nuclei that appeared in this work. Data taken from the EasySpin nuclear isotope database.[17]

2.2.4 Hyperfine Interaction

The hyperfine interaction (*hfi*) describes the interaction between the electron spin and the nearby nuclear spins. Such interaction can be split into two terms, the isotropic term and the anisotropic term. The first term is also called the Fermi contact interaction and it considers the overlap of the wave function of the electron spin with the nucleus. The Hamiltonian of the Fermi contact interaction is written as

$$\mathcal{H}_{\mathcal{F}} = \frac{2}{3}\mu_0 g_e \beta_e g_n \beta_n |\Psi_0(0)|^2 \mathbf{S}\cdot\mathbf{I} = a_{iso}\mathbf{S}\cdot\mathbf{I} \tag{2.19}$$

with the electron spin density at the nucleus and a_{iso} represents the isotropic hyperfine coupling. This term of the *hfi* is used for understanding the electron spin delocalization at the surrounding nuclei. Whereas the latter term of the *hfi*, is characterized by the electron-nuclear dipolar interaction. The Hamiltonian for the interaction between a nuclear spin **I** and an electron spin **S** is written as

$$\mathcal{H}_{dip} = \frac{\mu_0}{4\pi} g_e g_n \beta_e \beta_n \left\{ \frac{3(\mathbf{S}\cdot\mathbf{r})(\mathbf{r}\cdot\mathbf{I})}{r^5} - \frac{\mathbf{S}\cdot\mathbf{I}}{r^3} \right\}. \tag{2.20}$$

And such information can be used for providing the orientation and distance to the nucleus carrying the nuclear spin **I** near the electron spin. Combining the two terms (Eq. 2.19, 2.20) the spin Hamiltonian for *hfi* can be expressed as

$$\mathcal{H}_{hfi} = \mathbf{S}\cdot\mathbf{A}\cdot\mathbf{I}, \text{ where } \mathbf{A} = a_{iso}\mathbf{1} + \mathbf{T} \tag{2.21}$$

The principle values of the hyperfine tensor **A** take the form

$$\begin{cases} A_{xx} = a_{iso} - T - \delta \\ A_{yy} = a_{iso} - T + \delta \\ A_{zz} = a_{iso} + 2T \end{cases} \tag{2.22}$$

where the a_{iso}, T, and δ are the isotropic, axial, and rhombic component.

The hyperfine interaction, reports on the type of chemical bond and/or the nearby environment. However, in many cases, *hfi* of ligand nuclei is too weak to be resolved in CW-EPR. Therefore, hyperfine spectroscopies among the many pulsed EPR experiments are needed for more detailed investigations.

2.2.5 Nuclear Quadrupolar Interaction

For nuclei with nuclear spin $I > \frac{1}{2}$, the charge distributions are not spherical due to their structures. This results in an electric quadrupole moment that interacts with the electric field gradient. It is called the nuclear quadrupole moment Q. Even though the interaction is purely electrostatic, the orientation of nuclear quadrupole moment is linked to that of the nuclear spin. It can be considered as a self-interaction of the nuclear spin and the Hamiltonian is written as:

$$\mathcal{H}_{nqi} = \mathbf{I}\cdot\mathbf{P}\cdot\mathbf{I} = \frac{e^2 q Q}{4I(2I-1)} \left[\left(3I_z^2 - \mathbf{I}^2\right) + \eta\left(I_x^2 - I_y^2\right) \right]. \tag{2.23}$$

This is the same equation as the *zfi*, for which the *nqi* tensor **P** can be expressed as

$$\mathbf{P} = \begin{bmatrix} -K(1+\eta) & 0 & 0 \\ 0 & -K(1-\eta) & 0 \\ 0 & 0 & 2K \end{bmatrix} \tag{2.24}$$

with

$$K = \frac{e^2 qQ}{4I(2I-1)} \text{ and } 0 \leq \eta \leq 1 \tag{2.25}$$

and similar to the D and E value in *zfi*, the K and η describe the axial and rhombic distortion of the *nqi*.

In most cases, the *nqi* is small with respect to the linewidth in CW-EPR.[18] Whereas it can cause splitting of the signals in pulsed-EPR experiments like ENDOR or ESEEM. It can give more information but also brings more complexity to the analysis.

2.3 Spin Dynamics

In the classical description, when a magnetic field $\mathbf{B}$ is exerted to a magnetic moment $\mathbf{m}$, the magnetic moment experiences a torque $\boldsymbol{\tau}$ so that

$$\boldsymbol{\tau} = \mathbf{m} \times \mathbf{B}. \tag{2.26}$$

With the spin angular momentum $\mathbf{S}$, Eq. 2.26 can be written as the equation of motion for a single electron spin

$$\boldsymbol{\tau} = \boldsymbol{\mu}_S \times \mathbf{B} = \frac{d\mathbf{S}}{dt}. \tag{2.27}$$

Considering an ensemble of electron spins in the system, Eq.2.27 can be rewritten with the magnetization $\mathbf{M}$, the net magnetic moment per unit volume, as

$$\frac{d\mathbf{M}}{dt} = -g_e \beta_B \mathbf{M} \times \mathbf{B}_0. \tag{2.28}$$

Unless the magnetization is aligned parallel to the static field (assuming $\mathbf{B}_0 = (0,\, 0,\, B_0)$), there is always a torque perpendicular to its direction applying on it. This will induce a precession of the magnetization around the z-axis with an angular frequency[10]

$$\omega_S = g_e \beta_B B_0, \tag{2.29}$$

called the Larmor frequency. If an microwave with oscillating magnetic field

$$\mathbf{B}_1(t) = (B_1 \cos(\omega_{mw} t), B_1 \sin(\omega_{mw} t), 0) \tag{2.30}$$

is supplied, the whole system can be viewed in a rotating frame which is rotating at such frequency with respect to the laboratory z-axis. In the rotating frame, the equations of motion of the magnetization are given as[10]

$$\begin{cases} \frac{dM_x}{dt} = -\Omega_S M_y \\ \frac{dM_y}{dt} = \Omega_S M_x - \omega_1 M_z \\ \frac{dM_z}{dt} = \omega_1 M_y \end{cases} \tag{2.31}$$

with the resonance offset frequency

$$\Omega_S = \omega_S - \omega_{mw} \tag{2.32}$$

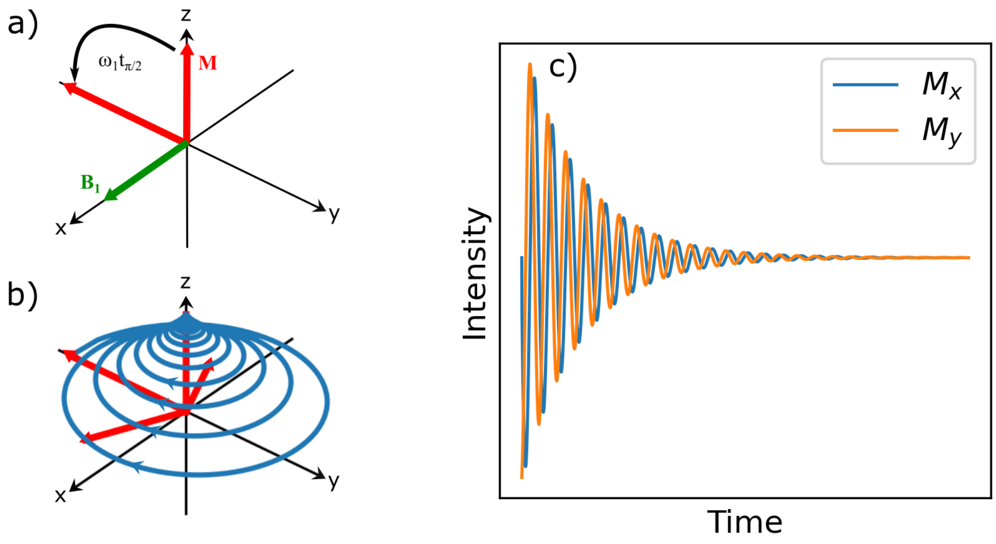

Figure 2.6: The schematic diagram of the time evolution of the electron magnetization. a) Shows a $\pi/2$ pulse flipping the magnetization $\mathbf{M}$. b) Shows how the magnetization with an initial state of $(M_x,\ M_y,\ M_z) = (M_0,\ 0,\ 0)$ precesses and relaxes back to equilibrium state $(0,\ 0,\ M_0)$. c) Shows the free induction decay (FID) of the measured M_x and M_y component.

and the precession frequency

$$\omega_1 = g_e \beta_B B_1 \tag{2.33}$$

to the additional $\mathbf{B}_1$ field. If the microwave frequency matches the Larmor frequency, the magnetization is rotated by an angle of $\omega_1 t$ around the x-axis in rotating frame.

This brings about the concept for microwave pulses, the most basic pulses are the $\pi/2$-and π-pulses, which turn the magnetization by $\pi/2$ and π. The general concept of pulsed-EPR experiments is to use these pulses to rotate the magnetization from the z-axis into the xy-plane, let it evolve under the influence of the spin Hamiltonian over time, then detect the final magnetization. Fig.2.6 shows an schematic diagram of an example of a $\pi/2$ pulse followed by a free induction decay (FID) of the M_x and M_y component.

To study the dynamics of a complex spin system in the pulse experiments, a quantum mechanical description is needed. The wave function of the spin system can be written as

$$|\Psi\rangle = \sum_{i=1}^{n} c_i \, |\psi_i\rangle \text{ , or in the matrix form } \boldsymbol{\Psi} = \begin{pmatrix} c_1 \\ \vdots \\ c_n \end{pmatrix} \tag{2.34}$$

with the eigenstates $|\psi_i\rangle$. And the expectation value of an observable $\mathbf{A}$ is given as

$$\langle \mathbf{A} \rangle = \langle \Psi | \, \mathbf{A} \, | \Psi \rangle = \sum_{i,j} c_i^\star c_j \, \langle \psi_i | \, \mathbf{A} \, | \psi_j \rangle \tag{2.35}$$

Defining the density matrix as

$$\boldsymbol{\rho} = \boldsymbol{\Psi}\boldsymbol{\Psi}^\dagger, \text{ for } \rho_{ij} = \langle \psi_i | \, \boldsymbol{\rho} \, | \psi_j \rangle = c_i c_j^\star, \tag{2.36}$$

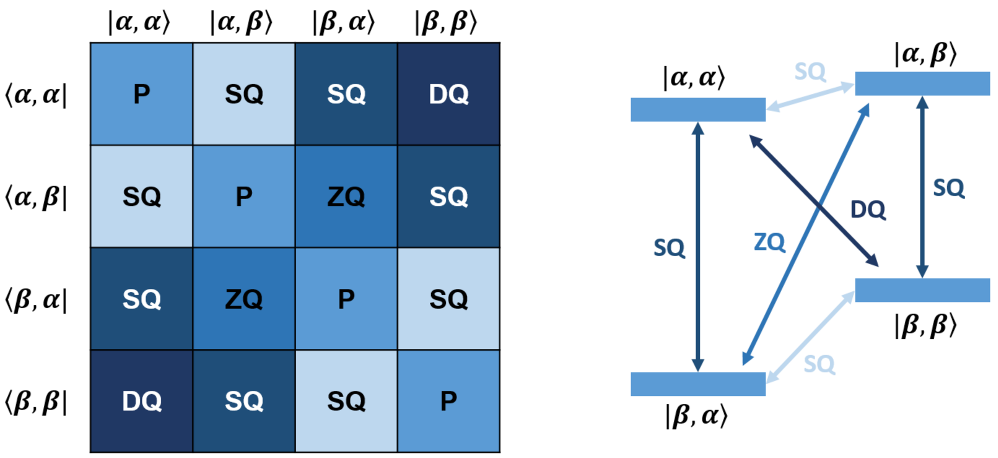

	$\lvert\alpha,\alpha\rangle$	$\lvert\alpha,\beta\rangle$	$\lvert\beta,\alpha\rangle$	$\lvert\beta,\beta\rangle$
$\langle\alpha,\alpha\rvert$	P	SQ	SQ	DQ
$\langle\alpha,\beta\rvert$	SQ	P	ZQ	SQ
$\langle\beta,\alpha\rvert$	SQ	ZQ	P	SQ
$\langle\beta,\beta\rvert$	DQ	SQ	SQ	P

$\lvert\alpha,\alpha\rangle$
SQ
$\lvert\alpha,\beta\rangle$
SQ
DQ
SQ
ZQ
$\lvert\beta,\beta\rangle$
SQ
$\lvert\beta,\alpha\rangle$

Figure 2.7: A scheme of density matrix for a two spin system. The diagram on the left shows the density matrix. Among the diagonal elements,**P** denotes the population of the eigenstates. For off-diagonal terms, **SQ** denotes the single quantum coherence, **DQ** denotes the double quantum coherence, and **ZQ** denotes the zero quantum coherence. The diagram on the right shows the energy levels arrangement in the two-spin system with transitions of different coherences. Reproduced from Ref.[10]

which describes the population of each eigenstate and coherence between different eigenstates (Fig.2.7), then Eq. 2.35 becomes

$$\langle \mathbf{A} \rangle = \sum_{i,j} \langle \psi_j | \boldsymbol{\rho} | \psi_i \rangle \langle \psi_i | A | \psi_j \rangle = \mathrm{Tr}(\boldsymbol{\rho}\mathbf{A}). \tag{2.37}$$

To understand what information is obtained through a pulse experiment, one needs to calculate the evolution of the density matrix over time during the pulse sequences. Writing the Schrödinger equation

$$i\hbar \frac{\partial}{\partial t} |\Psi\rangle = \mathcal{H} |\Psi\rangle \tag{2.38}$$

in the form of density matrix[10]

$$i\hbar \frac{\partial}{\partial t} \boldsymbol{\rho} = i\hbar \left(\frac{\partial}{\partial t} \boldsymbol{\Psi} \boldsymbol{\Psi}^\dagger + \boldsymbol{\Psi} \frac{\partial}{\partial t} \boldsymbol{\Psi}^\dagger\right) = \mathcal{H} \boldsymbol{\Psi} \boldsymbol{\Psi}^\dagger - \boldsymbol{\Psi} \boldsymbol{\Psi}^\dagger \mathcal{H} = [\mathcal{H}, \boldsymbol{\rho}] \tag{2.39}$$

one obtains the Liouville-von Neumann equation. The solution of the equation gives the density matrix at time t after the time evolution under the influence of the Hamiltonian $\mathcal{H}$,

$$\boldsymbol{\rho}(t) = e^{-i\mathcal{H}t/\hbar} \boldsymbol{\rho}(0) e^{i\mathcal{H}t/\hbar}. \tag{2.40}$$

The exponent operator

$$U_i(t) = e^{-i\mathcal{H}_i t/\hbar} \tag{2.41}$$

is called a propagator that propagates the density matrix in time.[10] From the mathematical point of view, a pulse experiment consists of a sequence of propagators. To examine the state of the spin system, a number of propagators are applied to the density matrix and the expectation value of the desired operator $\mathbf{A}$ is calculated as

$$\langle \mathbf{A} \rangle = \mathrm{Tr}(U_n(t) \dots U_1(t)\rho(0)U_1^\dagger(t) \dots U_n^\dagger(t)\mathbf{A}). \tag{2.42}$$

This is called the density matrix formalism.[10] The propagators correspond to either the perturbation (by m.w. or r.f. pulse) which transfer the matrix elements or the free evolution which changes the phase of the matrix elements (the off-diagonal elements) if it's in the eigenbasis of $\mathcal{H}$.

2.4 Experimental Methods

In this section, the experimental methods that have been applied in this thesis will be briefly introduced. It includes the methods to study the spin concentration/distribution, to disentangle different paramagnetic species, and to investigate the local environment of the paramagnetic species.

2.4.1 Quantitative EPR

Quantitative EPR is a simple technique providing the total number of spins. It is based on the fact that the spin numbers should be proportional to the double integral of the CW-EPR spectrum, if the proper experimental conditions are supplied. The intensity of the double integral of the CW-EPR spectrum follows the following equation:[11]

$$DI = c \cdot [G_R \cdot C_t \cdot n] \cdot \left[\frac{\sqrt{P} \cdot B_m \cdot Q \cdot n_B \cdot S \cdot (S+1) \cdot n_s}{f(B_1, B_m)} \right] \tag{2.43}$$

which:

c = A constant calculated from a sample with a known number of spins
G_R = Receiver Gain
C_t = Conversion time
n = Number of scans
P = Microwave power (W)
B_m = Modulation amplitude (Gauss)
Q = Quality factor of resonator
n_B = Boltzmann factor for temperature dependence
S = Total electron spin
n_s = Number of spins
$f(B_1, B_m)$ = Spatial distribution of the microwave field and the modulation field experienced by the sample

One can see that most of the parameters are specific for the instruments and resonators. One of the methods to perform quantitative EPR is to compare the double integral of the target sample with a standard with known spin numbers. Alternatively, the new Xenon software on the Bruker spectrometer has been implemented and calibrated with the needed information and can compute of the spin numbers.[19]

2.4.2 Instantaneous Diffusion

The transversal relaxation of the magnetization (T_m) is called the spin-spin relaxation. It describes how fast the xy component of the magnetization decays and dephases. As how it is called, the

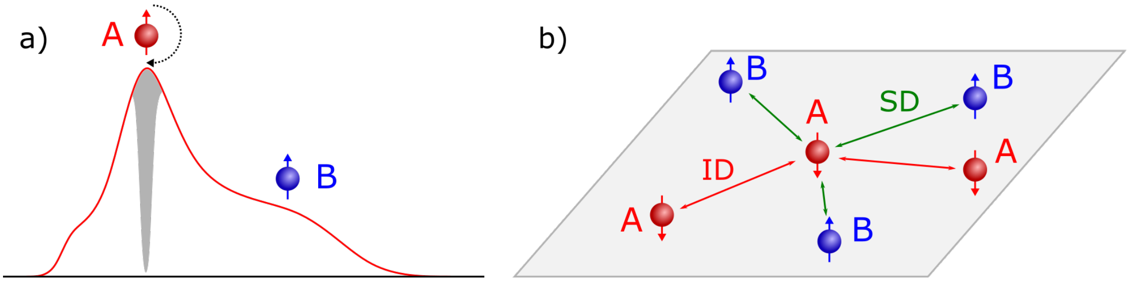

Figure 2.8: The scheme of T_m mechanisms. a) The spins that are excited, marked the shadowed area, are the A spins and the others are the B spins. b) The interaction between A and B spins includes the spectral and spin diffusion (SD) and the interaction among A spins is the instantaneous diffusion (ID).

interaction between electron spins accounts for the dephasing and decaying. The two major interactions are the spin/spectral diffusion and the instantaneous diffusion.[10] When a pulse is sent to the sample, the spins that are excited are called the A spins while the other spins are called the B spins.(Fig.2.8a) The spin/spectral diffusion is involved the interaction between the A spins and the B spins. Meanwhile, the interaction in between the A spins is called the instantaneous diffusion (ID).

In the measurement of T_m, the interpulse delay τ of the 2 pulse sequence is increased and the change of the echo intensity is recorded. (Fig.2.9a) The relation of the recorded T_m^{exp} to the turning angle θ of the second pulse is written as

$$\frac{1}{T_m^{exp}} = \frac{1}{T_m^{act}} + \frac{2\pi}{9\sqrt{3}}\gamma^2 hC_A\langle sin^2\frac{\theta}{2}\rangle = \frac{1}{T_m^{act}} + \frac{1}{T_m^{ID}} \tag{2.44}$$

where C_A represents the concentration of the A spin; and $\langle sin^2\frac{\theta}{2}\rangle$ is written as

$$\langle sin^2\frac{\theta}{2}\rangle = \int \frac{B_1^2}{(B'-B_0)^2+B_1^2}\sin^2\left[\gamma t_p\sqrt{(B'-B_0)^2+B_1^2}\right]g(B')dB' \tag{2.45}$$

with pulse length t_p of the second pulse and the spectral distribution $g(B')$ of the A spins.[20, 21] The second term in Eq. 2.44 is the instantaneous diffusion. The ID can be investigated by changing either the B_1 or the t_p. (Fig.2.9b) The idea of ID is that with different turning angles, the number of flipped A spins will be different. Therefore the dipolar interaction between A spins becomes a variable. (Fig.2.9c) By changing the turning angle θ of the second pulse, the real T_m can be extrapolated and the concentration of the A spins is obtained.

2.4.3 Echo-Detected Field Sweep (EDFS)

Among the large number of different pulsed-EPR techniques, the echo-detected field sweep (EDFS) is one of the most basic experiments. In general, it provides the absorption spectrum of the sample which can be analogous to the integral of the CW-EPR spectrum with less sensitivity. But some pulse techniques can be used to separate different paramagnetic species by their relaxation times.

The most basic EDFS experiment is applying the 2-pulse sequence which gives the electron spin echo and recording the echo intensity at each field position. (Fig.2.10) The typical 2-pulse sequence is composed of a $\pi/2$-pulse and a π-pulse after the interpulse delay τ. The $\pi/2$-pulse flip the magnetization to the xy-plane and during the interpulse delay the magnetization starts to dephase. With the π-pulse, the magnetization is refocused and the electron spin echo is detected after τ.

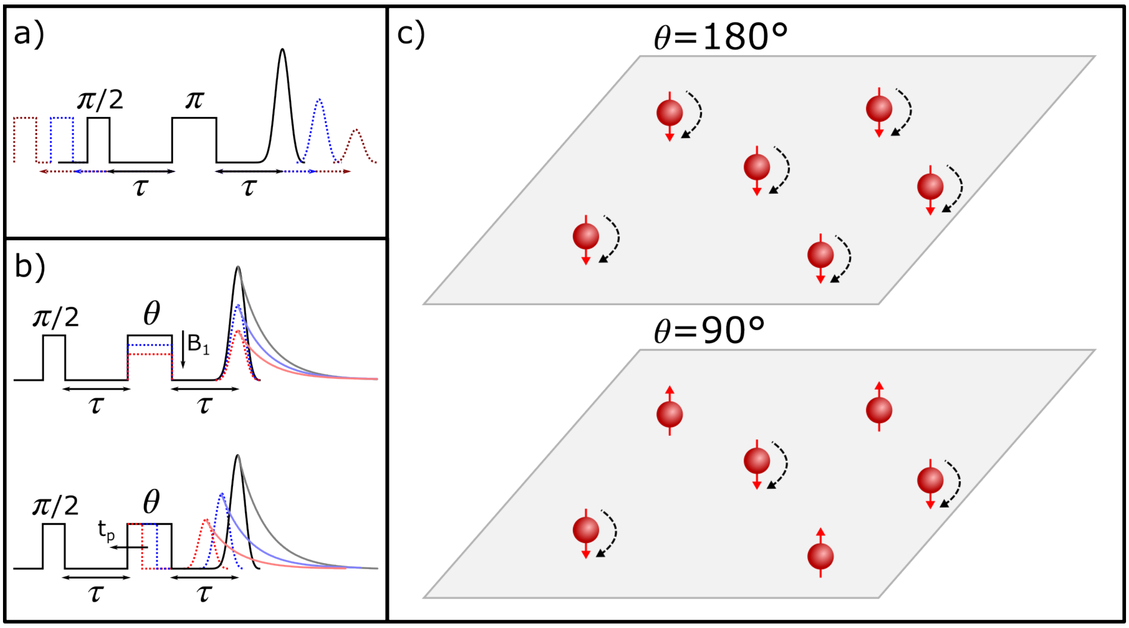
a)
$\pi/2$
π
τ
τ
b)
$\pi/2$
θ
B_1
τ
τ
$\pi/2$
θ
t_p
τ
τ
c)
θ=180°
θ=90°

Figure 2.9: The scheme of the Instantaneous Diffusion (ID). a) The pulse sequence of a basic T_m measurement. b) The two methods to perform the ID experiment. c) The relation between the turning angle θ of the second pulse and the flipped A spin population.

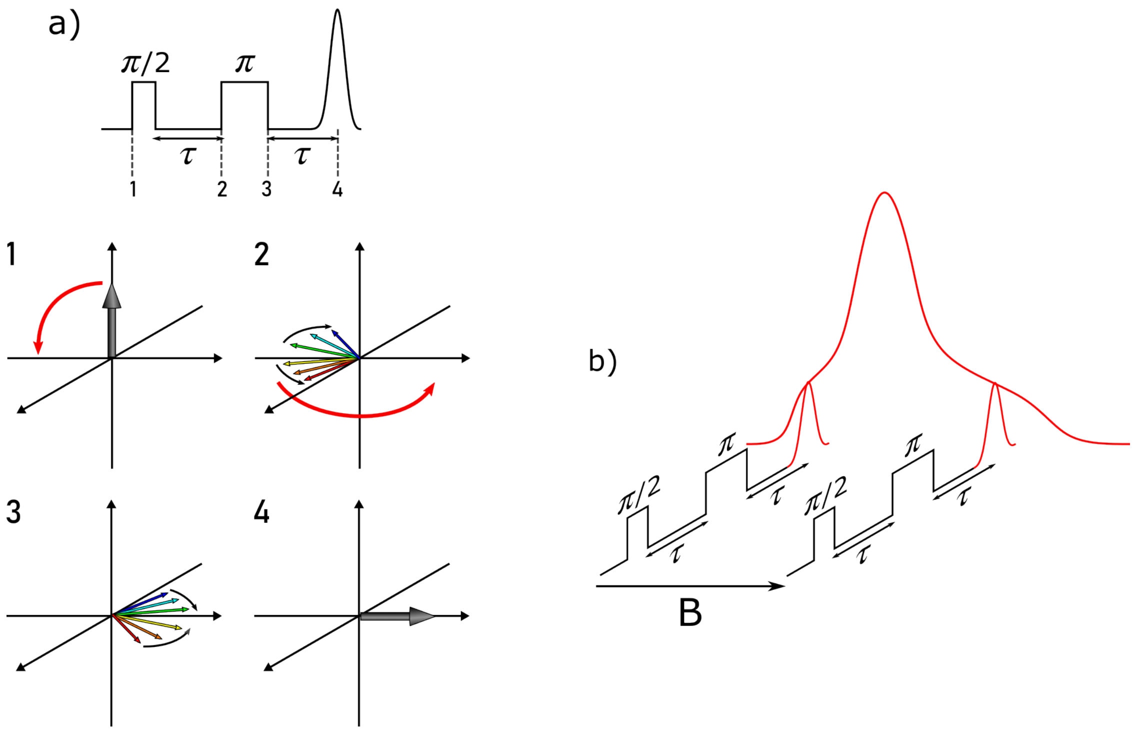
a)
$\pi/2$
π
τ
τ
1
2
3
4
1
2
3
4
b)
$\pi/2$
π
τ
τ
$\pi/2$
π
τ
τ
B

Figure 2.10: The scheme of the 2-pulse echo and the echo-detected field sweep (EDFS). a) The typical 2-pulse echo is composed of a $\pi/2$ pulse followed by a π pulse with an interpulse delay τ. The diagram at the bottom shows how the magnetization is manipulated by the pulses and evolves overtime at each marked time step. b) By keeping the pulse sequence and sweeping over the field, the absorption spectrum is recorded.

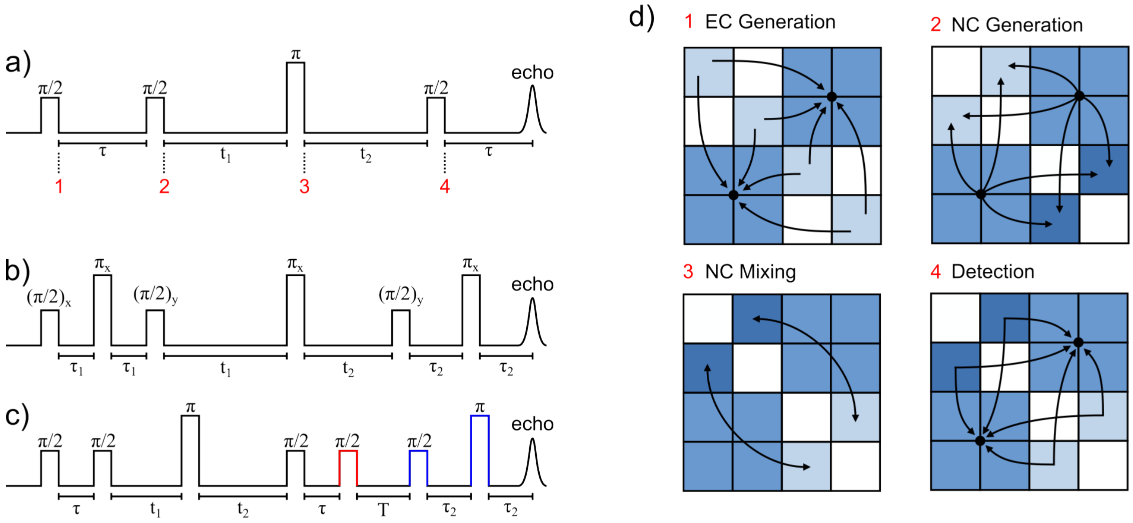

Figure 2.11: The scheme of the HYSCORE Spectroscopy. Diagrams on the left show the pulse sequences of the a) standard HYSCORE, b) 6-pulse HYSCORE, and c) Remote HYSCORE (the storage pulse in red and detection pulse in blue). Diagram on the right d) shows how the density matrix elements transfer after each pulse.

In the more sophisticated experiments, one might either add additional pulses, change the pulse lengths, or manipulate with the interpulse delay. Practical applications will be shown in the results and discussion.

2.4.4 Hyperfine Sublevel Correlation Spectroscopy

To study the hyperfine couplings that are unresolved in CW-EPR, there are many techniques categorized as the hyperfine spectroscopy at hand. There are the Electron-Nuclear Double Resonance (ENDOR), ELDOR-Detected NMR (EDNMR), and the Electron Spin Echo Envelope Modulation (ESEEM). Each of the hyperfine spectroscopies has advantages and disadvantages. The information one provides can be complementary to the others. Among the many hyperfine spectroscopies, ESEEM relies on the forbidden transitions and anisotropy of the spin system,[22, 23] and it is more effective in detecting weak hyperfine couplings.[24] Therefore, it is applied as the tool to study the local environment of the spin systems in this work.

There are different pulse sequences for ESEEM experiments. In the case of overlapping signals from multiple nuclei, the 2D 4-pulse ESEEM, Hyperfine Sublevel Correlation (HYSCORE) spectroscopy, can be of help. The pulse sequence of the HYSCORE spectroscopy follows $\pi/2 - \tau - \pi/2 - t_1 - \pi - t_2 - \pi/2 - \tau - echo$ (Fig.2.11a). The first pulse transfers the polarization (P) to electron coherence (EC); the second pulse transfers the EC to nuclear coherence (NC); the third pulse mixes the NC in the two electron manifolds, say the electron $|\alpha\rangle$ and $|\beta\rangle$ states; and finally the last pulse transfers the NC back to EC for detection.[24] Fig.2.11d depicts how the elements of the density matrix transfers after each pulse in a two spin system. A π pulse is inserted between the second and fourth pulse to interchange the nuclear coherence in the two electron spin manifolds. The Fourier transform of the spectrum recorded in the evolution times t_1 and t_2 maps the frequencies in 2D. (Fig.2.11d)

To understand the nuclear frequencies in the two electron manifolds, a simplified case of a

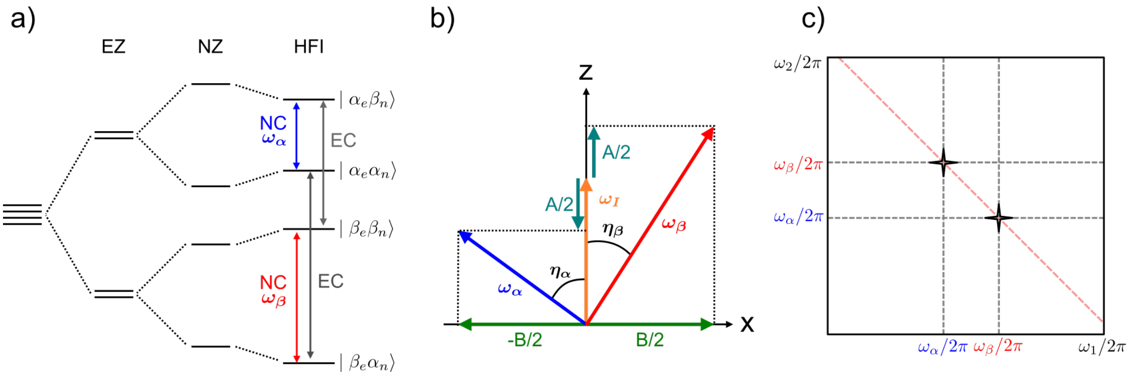
a)
EZ
NZ
HFI
$|\alpha_e\beta_n\rangle$
NC
ω_α
EC
$|\alpha_e\alpha_n\rangle$
$|\beta_e\beta_n\rangle$
NC
ω_β
EC
$|\beta_e\alpha_n\rangle$
b)
Z
A/2
A/2
ω_I
η_β
ω_β
η_α
ω_α
-B/2
B/2
X
c)
$\omega_2/2\pi$
$\omega_\beta/2\pi$
$\omega_\alpha/2\pi$
$\omega_\alpha/2\pi$ $\omega_\beta/2\pi$
$\omega_1/2\pi$

Figure 2.12: The scheme of the nuclear frequencies in the two electron manifolds. The diagram a) indicates the energy level splitting under the influence of different interactions, b) indicates the vectors of the nuclear frequencies composed of the secular and pseudo-secular hfi components, and c) shows how the cross-peaks in the HYSCORE spectrum correspond to the nuclear frequencies.

$S = 1/2$ and $I = 1/2$ system is considered here. The spin Hamiltonian can be written as

$$\mathcal{H}_0 = \omega_S S_x - \omega_I I_z + A S_z I_z + B S_z I_x \tag{2.46}$$

where ω_S and ω_I are the electron and nuclear Zeeman frequencies and

$$A = A_{zz}, \text{ and } B = \sqrt{A_{zx}^2 + A_{zy}^2}, \tag{2.47}$$

that are called the secular and pseudo-secular hfi constants.[10, 24, 25] The energy levels splitting according to these interactions is shown in Fig.2.12a. By introducing the spin polarization operators for the electron spin manifolds to Eq. 2.46

$$1 = S^\alpha + S^\beta \text{ and } S_z = \frac{1}{2}(S^\alpha - S^\beta), \tag{2.48}$$

the nuclear frequencies in the each electron spin manifolds are given as[10]

$$\begin{aligned} \omega_\alpha &= \left(\tfrac{A}{2} - \omega_I\right)\cos\eta_\alpha - \tfrac{B}{2}\sin\eta_\alpha \\ \omega_\beta &= \left(\tfrac{A}{2} + \omega_I\right)\cos\eta_\beta + \tfrac{B}{2}\sin\eta_\beta \end{aligned} \tag{2.49}$$

with

$$\eta_{\alpha,\beta} = \tan^{-1}\left(\frac{B/2}{\omega_I \mp A/2}\right). \tag{2.50}$$

Eq. 2.49 can be visualised in a vectorial picture (Fig.2.12b). Fig.2.12c shows how these nuclear frequencies form the cross-peaks in the HYSCORE spectrum after Fourier transform.

Apart from the frequencies observed in the spectrum, the signal intensities also need to be considered. The echo modulation of the HYSCORE experiment can be written as[24]

$$V_{4p_{tot}}(\tau, t_1, t_2) = 1 - \frac{k}{4}(V_{\mathrm{I}} + V_{\mathrm{IIa}} + V_{\mathrm{IIb}} + V_{\mathrm{IIIa}} + V_{\mathrm{IIIb}}) \tag{2.51}$$

with the modulation depth

$$k = \left(\frac{B\omega_I}{\omega_\alpha\omega_\beta}\right)^2 \tag{2.52}$$

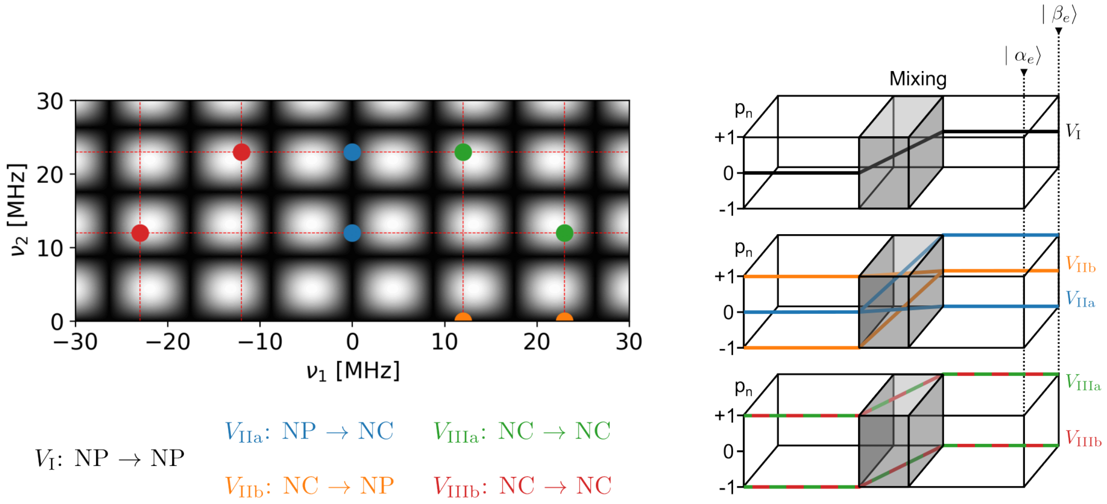

Figure 2.13: The scheme of HYSCORE cross-peaks corresponding to different coherence transferring pathways with the τ suppression effect. The cross-peaks corresponding to different coherence transferring pathways are indicated in the same colors. Nuclear frequencies ω_α and ω_β are 12 and 23 MHz. The grayscale background indicates the suppression effect with $\tau = 114$ ns.

and for each V_{x} term represents different coherence transferring pathways (CTP) induced by the π pulse after the NC and nuclear polarization (NP) are generated by the second $\pi/2$ pulse. It is clear that the modulation depth k drops to zero when the hfi is isotropic ($B = 0$). This is why, as stated in the previous paragraph, the ESEEM experiments rely on anisotropy of the system. For each of the pathways, the V_{I} describes the transfer from NP to NP, the $V_{\mathrm{IIa,b}}$ describe the transfer between NP and NC, and $V_{\mathrm{IIIa,b}}$ describe the transfer between the NCs. The CTPs are depicted as the diagram on the right in Fig.2.13, which the nuclear coherence order $\mathrm{p_n}$=0 indicates NP and $\mathrm{p_n}$=±1 indicates NC. On the left of Fig.2.13, one can see that only the V_{IIIx} pathways are of interest in the HYSCORE experiments. Among them, the V_{IIIa} gives rise to the cross-peaks in the (+,+) quadrant while the V_{IIIb} gives rise to those in the (−,+) quadrant.[24] For both terms, the modulations are described with the same pre-factor which depends on the interpulse delay τ as

$$V_{\mathrm{IIIa,b}} \propto \sin(\omega_\alpha \tau/2)\sin(\omega_\beta \tau/2). \tag{2.53}$$

And this results in suppression to the cross-peaks (as the shadowed region in Fig.2.13). Therefore, an appropriate HYSCORE experiment must come with a careful selection of the τ. In the case of wide ridges, multiple τ might be needed to obtain the full spectrum.

In the case of multiple nuclei in the spin system, one might encounter the problem of cross suppression.[26] The presence of nuclei with large modulation depth ($k \approx 1$) can suppress the nuclei with small modulation depth ($k \approx 0$). To circumvent this issue, one might apply the 6-pulse HYSCORE instead of the stadard 4-pulse HYSCORE.[27, 28] (Fig.2.11b) With such a pulse sequence, the single quantum transitions from the weakly modulated nuclei suffer less suppression from the strongly modulated nuclei. Also, the combination frequencies between different nuclei is absent in the spectrum of the 6-pulse HYSCORE experiment. This simplifies the complexity for the analysis to the results.

To avoid blind spots, sometimes multiple τ is needed to recover the full spectrum in HYSCORE. This can be time-consuming. Meanwhile, as shown in Eq. 2.53, the nth τ suppression takes place at

$\frac{n}{\tau}$ in the frequency domain. Therefore, it is also possible to avoid the suppression by using short τ. However, the echo might fall into the detection dead-time and make it impossible to record the spectrum. To solve this problem, a remote detection technique can be used.[29, 30] The idea is to move and store the magnetization in the z-direction with a $\pi/2$ storage pulse and detect it after a delay T with a 2-pulse sequence and $\tau_2 > t_d$ (t_d the detection dead-time). (Fig.2.11c)

The adaptation of the HYSCORE experiments with different pulse sequences will be shown and discussed in the results and discussion chapter.

Bibliography

(1) Zavoisky, E. K. *Zhur. Eksperiment. i Theoret. Fiz.* **1945**, *15*, 344–350 (cited on page 13).

(2) Zeeman, P. *The London, Edinburgh, and Dublin Philosophical Magazine and Journal of Science* **1897**, *43*, 226–239 (cited on page 13).

(3) Zeeman, P. *Nature* **1897**, *55*, 347–347 (cited on page 13).

(4) Gerlach, W.; Stern, O. *Zeitschrift für Physik* **1922**, *8*, 110–111 (cited on page 13).

(5) Gerlach, W.; Stern, O. *Zeitschrift für Physik* **1922**, *9*, 353–355 (cited on page 13).

(6) Gerlach, W.; Stern, O. *Zeitschrift für Physik* **1922**, *9*, 349–352 (cited on page 13).

(7) Uhlenbeck, G. E.; Goudsmit, S. *Die Naturwissenschaften* **1925**, *13*, 953–954 (cited on page 13).

(8) Uhlenbeck, G. E.; Goudsmit, S. *Nature* **1926**, *117*, 264–265 (cited on page 13).

(9) Junk, M. J. N. In *Assessing the Functional Structure of Molecular Transporters by EPR Spectroscopy*; Springer Berlin Heidelberg: Berlin, Heidelberg, 2012; Chapter Electron P, pp 2–52 (cited on page 13).

(10) Schweiger, A.; Jeschke, G., *Principle of Pulse Electron Paramagnetic Resonance*; Oxford University Press: Oxford, 2001 (cited on pages 14, 22, 24–26, 29).

(11) Eaton, G. R.; Eaton, S. S.; Barr, D. P.; Weber, R. T., *Quantitative EPR*, 1st edition; Springer, Vienna: 2010 (cited on pages 14, 25).

(12) Abragam, A.; Pryce, M. H. L. *Proceedings of the Royal Society of London. Series A. Mathematical and Physical Sciences* **1951**, *205*, 135–153 (cited on page 16).

(13) Pryce, M. H. L. *Proceedings of the Physical Society. Section A* **1950**, *63*, 25–29 (cited on page 16).

(14) Atherton, N., *Principles of Electron Spin Resonance*; Ellis Horwood Limited: 1993 (cited on pages 16, 17, 19).

(15) Gast, P.; Groenen, E. J. In *eMagRes*; Major Reference Works; John Wiley & Sons, Ltd: Chichester, UK, 2016, pp 1435–1444 (cited on page 16).

(16) Telser, J. *eMagRes* **2017**, *6*, 207–234 (cited on pages 19, 20).

(17) Stoll, S.; Schweiger, A. *Journal of Magnetic Resonance* **2006**, *178*, 42–55 (cited on page 20).

(18) Stoll, S.; Goldfarb, D. *eMagRes* **2017**, *6*, 495–510 (cited on page 22).

(19) Eichhoff, U.; Höfer, P. *Applied Magnetic Resonance* **2020**, *51*, 1723–1737 (cited on page 25).

(20) Salikhov, K. M.; Dzuba, S. A.; Raitsimring, A. M. *Journal of Magnetic Resonance (1969)* **1981**, *42*, 255–276 (cited on page 26).

(21) Raitsimring, A. M.; Salikhov, K. M. *Bulletin of Magnetic Resonance* **1985**, *7*, 184–217 (cited on page 26).

(22) Mims, W. B. *Physical Review B* **1972**, *5*, 2409–2419 (cited on page 28).

(23) Höfer, P.; Grupp, A.; Nebenführ, H.; Mehring, M. *Chemical Physics Letters* **1986**, *132*, 279–282 (cited on page 28).

(24) Van Doorslaer, S. *eMagRes* **2017**, *6*, 51–70 (cited on pages 28–30).

(25) Bennati, M. *eMagRes* **2017**, *6*, 271–282 (cited on page 29).

(26) Stoll, S.; Calle, C.; Mitrikas, G.; Schweiger, A. *Journal of Magnetic Resonance* **2005**, *177*, 93–101 (cited on page 30).

(27) Song, R.; Zhong, Y. C.; Noble, C. J.; Pilbrow, J. R.; Hutton, D. R. *Chemical Physics Letters* **1995**, *237*, 86–90 (cited on page 30).

(28) Kasumaj, B.; Stoll, S. *Journal of Magnetic Resonance* **2008**, *190*, 233–247 (cited on page 30).

(29) Cho, H.; Pfenninger, S.; Gemperle, C.; Schweiger, A.; Ernst, R. *Chemical Physics Letters* **1989**, *160*, 391–395 (cited on page 31).

(30) Höfer, P. Distortion-Free Electron-Spin-Echo Envelope-Modulation Spectra of Disordered Solids Obtained from Two-Dimensional and Three-Dimensional HYSCORE Experiments, 1994 (cited on page 31).

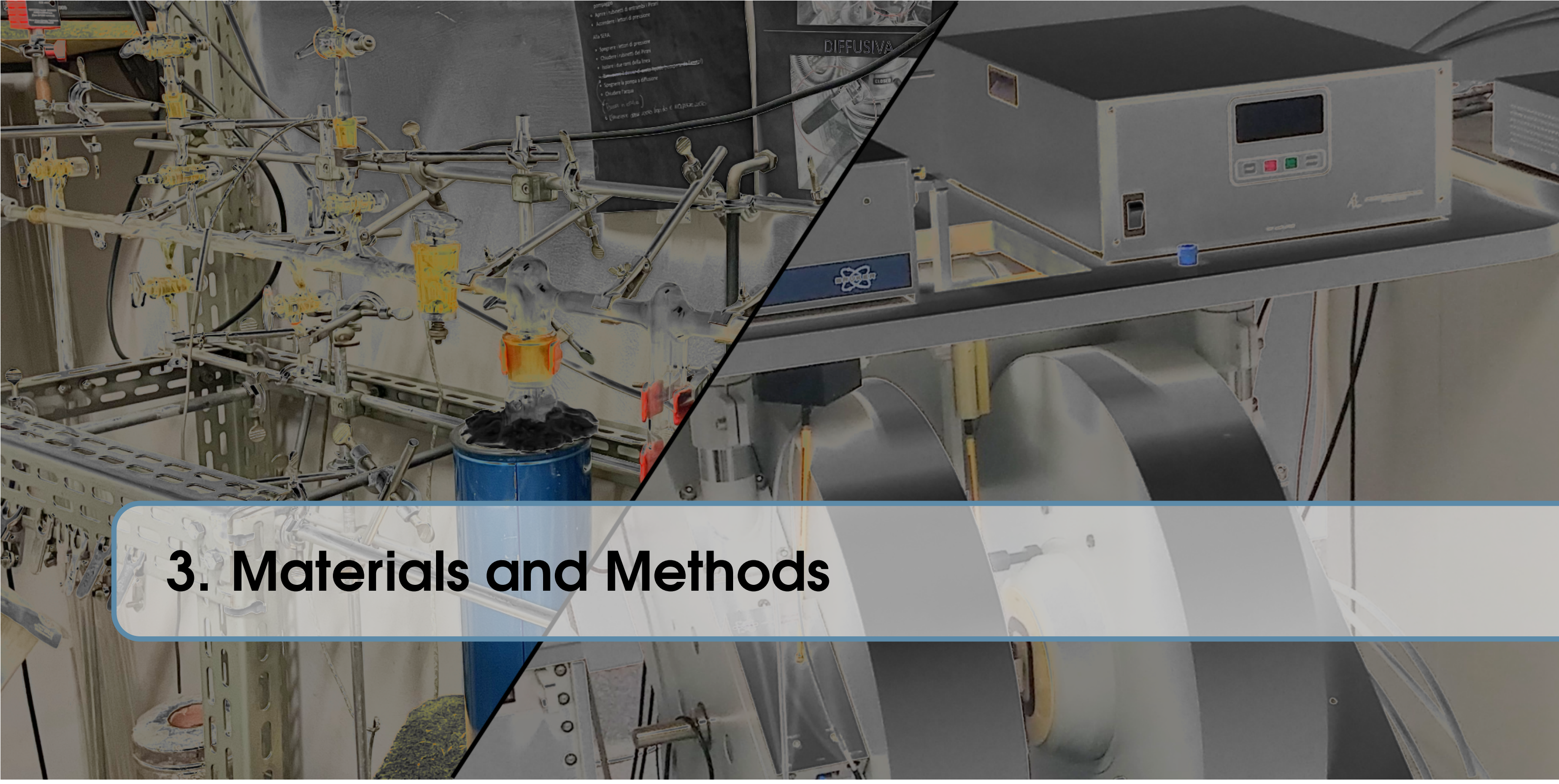

3. Materials and Methods

In this chapter, the details of the experiments are provided. The information related to the sample preparation is included in the first section, while the EPR methods are described in the second section.

3.1 Materials

The Phillips catalysts were synthesized at Prof. Elena Groppo's group at University of Turin. The $Cr[CH(SiMe_3)_2]_3/SiO_2$ catalysts were supplied by Prof. Elena Groppo at University of Turin. The (Cr-)silico-aluminophophate-5 ((Cr-)SAPO-5) were synthesized at Prof. Martin Hartmann's group at University of Erlangen-Nuremberg. Details of how the materials were synthesized are described in the following subsections.

3.1.1 Phillips Catalyst

The Phillips catalysts were prepared by wet-impregnation method. CrO_3 was dissolved in water and added drop-wise to the fumed silica (Aerosil 300 with surface area ca 300 m^2/g) until the silica forms the gel. The concentration of the CrO_3 solution was calculated so that the amount of the solution was just enough to form the gel and reach the desired Cr concentration on silica. The gel was then stirred with glass rod to make sure the mixing of the CrO_3 solution was mixed homogeneously with the silica. The beaker was covered with parafilm which contains holes and let dry in air for about two weeks. The dried mixture was ground with mortar for further experiments. In this work, 5 different Cr loadings (1, 0.5, 0.1, 0.05, 0.01 wt-%) were used.

3.1.2 $Cr(CH(SiMe_3)_2)_3/SiO_2$

The samples are prepared according to the procedure described in the published paper.[1]

The $Cr[CH(SiMe_3)_2]_3$ was synthesized from $(Me_3Si)_2CHCl$ and $CrCl_3$ following the procedure reported by Barker and colleagues.[2] The silica support (Sylopol952 from Grace, surface area 300 m^2/g and pore volume 1.6 cm^3/g) was calcined for 24 h at 873 K under a stream of N_2. The hexane solution of $Cr[CH(SiMe_3)_2]_3$ was then reacted for 1h at 313 K with the preactivated silica and outgassed under dynamic vacuum at the same temperature until no volatiles appeared.[3]

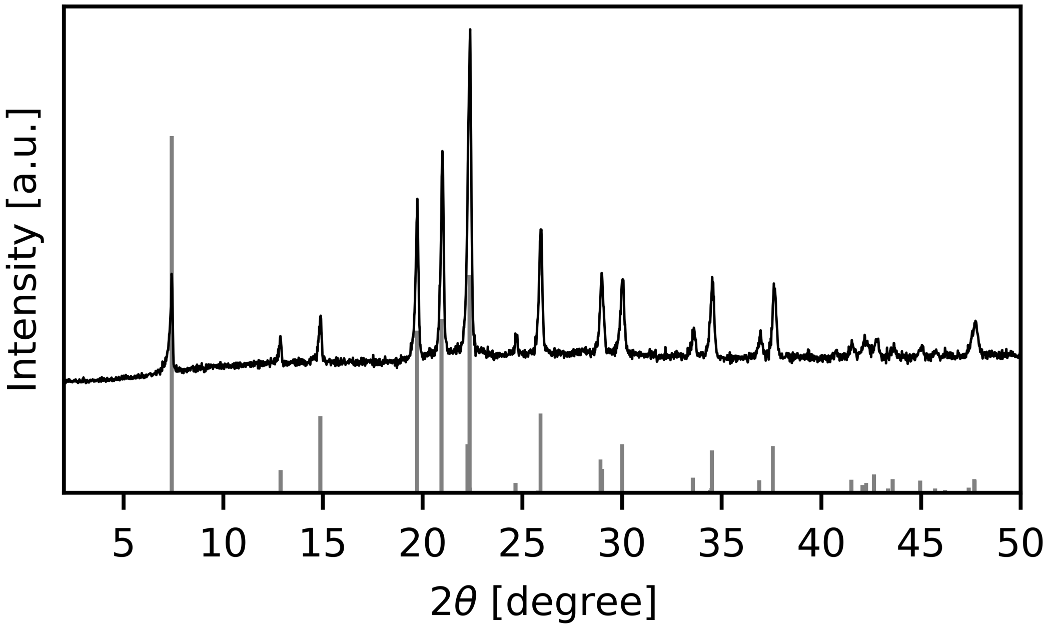

Figure 3.1: The PXRD pattern of the calcined Cr-SAPO-5

The catalysts were synthesized with four different Cr loadings, 0.2, 0.3, 0.4, and 0.5 wt-%. And they are denoted as nCr[CH(SiMe$_3$)$_2$]$_3$/SiO$_2$ with n as the Cr loading.

3.1.3 Silico-Aluminophosphate-5 (SAPO-5)

The silico-aluminophophate-5 (SAPO-5) and CrSAPO-5 were synthesized by hydrothermal method reported by Zhu and Kevan and described in a paper of this work.[4, 5]

The synthesis started by mixing 20.400 g of aluminum isopropoxide and 20.000 g of distilled water and stirring until the slurry was homogeneous. The slurry was added drop-wise with 12.106 g of 85% phosphoric acid; for CrSAPO-5, the solution of 0.027 g of $CrCl_3{\cdot}H_2O$ dissolved in 4.185 g of distilled water is added additionally. After stirring for 1 h, a mixture of 0.900 g of fumed silica and 10.000 g of distilled water was added dropwise and stirred for another 0.5 h. Afterward, 7.150 g of tripropylamine was added dropwise to the mixture and stirred overnight to ensure the homogeneity. The mixture was transferred to a 100 mL Teflon-lined autoclave and heated at 493 K for 48 h. The autoclave was quenched after synthesis, and the solid product was recovered by centrifugation, repeatedly washed with water, and dried at 353 K overnight. To removed the template, the sample was calcined at 823 K in nitrogen flow for 12 h and in air flow for 6 h.

The AFI structure of the SAPO-5 and CrSAPO-5 was verified by the powder X-ray diffraction (PXRD) performed by Ms. Susanne Pachaly from Prof. Martin Hartmann's group at University of Erlangen-Nuremberg. (Fig.3.1)

3.2 Treatments

3.2.1 Cr-based Catalyst: Activation and Ethylene Polymerization

The Phillips catalysts were activated following the protocols reported by Morra and coworkers. [6]

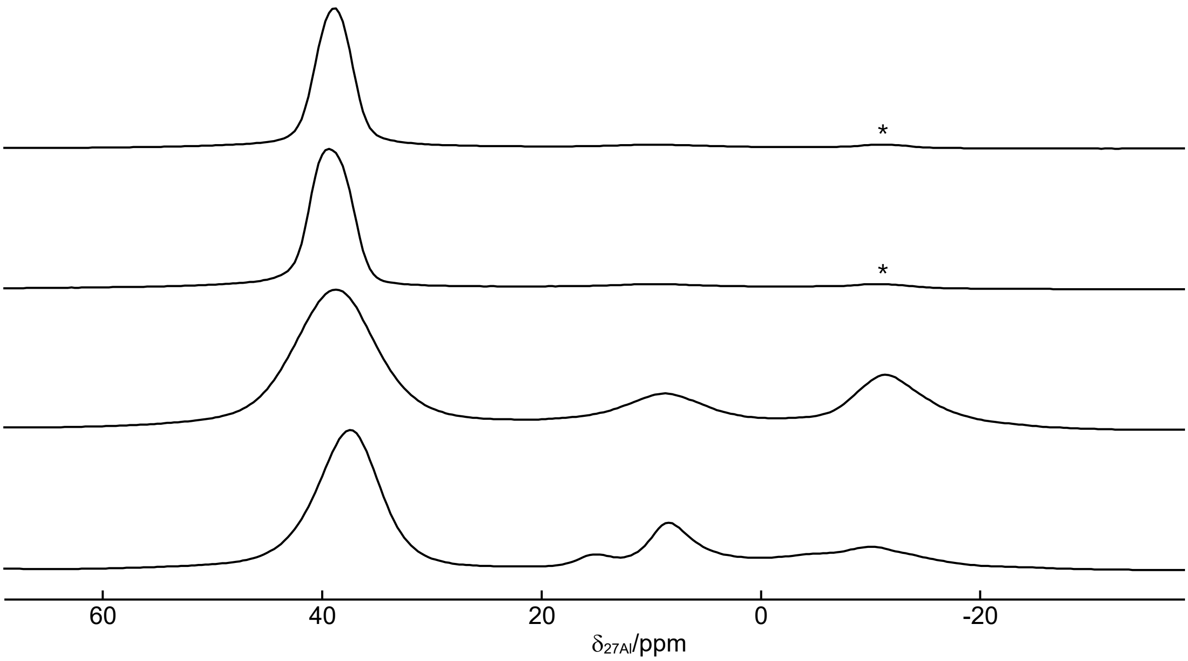

Figure 3.2: Isotropic part of ^{27}Al MAS spectra of four SAPO-5 samples. From top to bottom: 350oC activated, 200oC activated, calcined, as-synthesized sample. Asteriks denote spinning side-bands.

The activation started from the dehydration by heating up to 393 K with a 2 K/min ramp under dynamic vacuum and left at this temperature for 30 min. Then it was heated to 923 K with a 5 K/min ramp under dynamic vacuum to remove the hydroxyl group at the surface. Subsequently, oxidation in O_2 (with pressure ~100 mbar, twice) was performed at this temperature to graft the Cr at the silica surface. The O_2 was removed at 623 K.

To perform the polymerization, the catalyst was reacted with ethylene (with pressure ~100 mbar in the enclosed EPR cell) at 423 K for up to 25 hr. EPR measurements were conducted at reaction times: 1, 2, 3, 5, 20, 25 hr. Whenever the cell was removed from the oven for measurements, the reaction was quenched by keeping the cell in liquid nitrogen.

For the $Cr[CH(SiMe_3)_2]_3/SiO_2$ catalysts, ethylene was admitted directly inside the EPR cell (ca. 100 mbar) at room temperature and measured after 10 min of poylmerization.[7]

3.2.2 Silico-Aluminophosphate-5 (SAPO-5): Activation and Reactivity

The SAPO-5 materials were activated under dynamic vacuum at 473 K for 2 hr or at 623 K overnight. Solid-state NMR experiments were conducted by Dr. Marko Bertmer at Leipzig University to characterize the ^{27}Al species present in the samples that were as-synthesized, calcined, activated at 200°C, and 350°C. (Fig.3.2) The spectra shows dominant ^{27}Al species with $e^2qQ/h \leq 2.3$ MHz at 40.0 ppm assigned to four-coordinated aluminum,[8] while the signals at 10 ppm were assigned to five-coordinated aluminum and simulated with isotropic shift of 10.8 ppm and $e^2qQ/h = 4.0$ MHz with large uncertainty due to the low amount.

The NO gas was admitted to the EPR tube after the activation for the SAPO-5. The amount of NO gas introduced was estimated by the NO pressure at the vacuum line before and after the EPR tube was placed in a liquid N_2 cold trap.

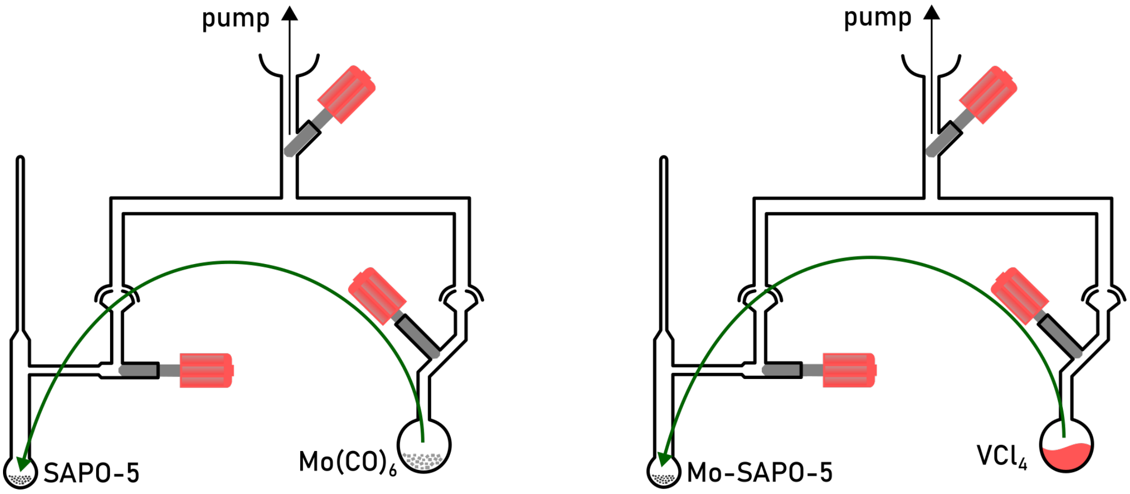

Figure 3.3: A scheme of Mo/V-SAPO-5 Grafting Method using the EPR cell and flask with teflon stopcocks.

In this work, the SAPO-5 samples were prepared with 10/20 μmol of NO loadings enclosed in the EPR tube.

3.2.3 Silico-Aluminophosphate-5 (SAPO-5): Bi-Metallic System

For the bi-metallic system study, the SAPO-5 materials were prepared with V and/or Mo grafted.

The procedure for grafting the V at the surface of SAPO-5 was according to the work reported by Lagostina, et al.[9] The SAPO-5 activated at 623 K was exposed to VCl_4 vapor several times. (Fig.3.3) The cell was evacuated after each exposure to remove excess VCl_4 and the reaction products (HCl).

To graft the Mo, the procedure developed by Abdo and Howe[10] was adapted and tested. The precursor $Mo(CO)_6$ (commercial Sigma Aldrich) was sublimated at room temperature and let adsorbed by the activated SAPO-5. (Fig.3.3) After the adsorption, the sample was treated under dynamic vacuum at 473 K for 1h. Then it was oxidized with 100 mbar oxygen at rising temperature (from 373 to 573 K) to reach 6+ oxidation state.

For the bi-metallic system, the Mo was first grafted then following the procedure of VCl_4 vapor phase grafting to obtain the final product.

3.3 EPR Characterization

The X-band (microwave frequency ~9.5 GHz) CW EPR spectra measured at University of Turin, the measurements were performed on a Bruker EMX spectrometer equipped with a ER4122SHQE cavity. Low temperature spectra were recorded using the finger dewar filled with liquid N_2.

The X-band CW EPR spectra measured at Leipzig University, in particular the spectra recorded at temperature below 77 K, were conducted on a Bruker EMX Micro spectrometer equipped with a Bruker ER4119HS cavity and with an Oxford Instruments He gas-flow cryostat ESR900.

Pulsed-EPR experiments at X-and were performed on the Bruker Elexys 580 EPR spectrometers equipped with the Bruker EN4118X-MD-4 cavity and the Oxford Instruments He gas-flow cryostat CF935O at University of Turin; and the Bruker EN4118X-MD-4 cavity and the Oxford Instruments He gas-flow cryostat CF935P at Leipzig University.

The Q-band (microwave frequency ∼34 GHz) CW and pulsed EPR spectra were performed on a Bruker Elexys 580 EPR spectrometer equipped with the Burker EN 5107D2 with an Oxford Instruments He gas-flow cryostat CF935O and a Bruker ER035M NMR gaussmeter.

EDFS experiments were performed with the pulse sequence $\frac{\pi}{2}$-τ-π-τ-echo while sweeping the external field (B_0).

T_1 filtered EDFS experiments were performed with the pulse sequence π-T-$\frac{\pi}{2}$-τ-π-τ-echo where T were set to eliminate signals of the filtered paramagnetic species.

T_m experiments[11] regarding the instantaneous diffusion mechanism were performed with the pulse sequence $\frac{\pi}{2}$-t-θ-t-echo for t incremented for suitable relaxation times and turning angles of θ-pulse were varied by changing the B_1 from MPFU channel amplitude or by changing the length of the pulses.

HYSCORE experiments[12] were performed with the pulse sequence $\frac{\pi}{2}$-τ-$\frac{\pi}{2}$-t_1-π-t_2-$\frac{\pi}{2}$-τ-echo with t_1 and t_2 incremented by 16 ns at X-band and 8/16 ns at Q-band. The interpulse delays τ were chosen to enhance/suppress the desired/unwanted cross-peaks.[13] Phase cycles of 4-/8-step were used to eliminate unwanted echos.

6-pulse HYSCORE experiments[14] were performed at Q-band with the pulse sequence $(\frac{\pi}{2})_x$-τ_1-π_x-τ_1-$(\frac{\pi}{2})_y$-t_1-π_x-t_2-$(\frac{\pi}{2})_y$-τ_2-π_x-τ_2-echo with t_1 and t_2 incremented by 16 ns. The interpulse delays τ_1 and τ_2 were set the same to minimize the blind-spot issue and the chosen to enhance/suppress the desired/unwanted cross-peaks.[13] Phase cycles of 8-step were used to eliminate unwanted echos.

Remote-HYSCORE experiments[13] were performed with the pulse sequence $\frac{\pi}{2}$-τ_1-$\frac{\pi}{2}$-t_1-π-t_2-$\frac{\pi}{2}$-τ_1-$\frac{\pi}{2}$-T-$\frac{\pi}{2}$-τ_2-π-τ_2-echo. The interpulse delay τ_1 were picked to obtain the minimal τ-suppression across the spectrum, and t_1 and t_2 were selected with the same principle as the standard HYSCORE. The delay T after storage pulse was picked as short as the phase memory time, and τ_2 was picked long enough to avoid signal covered by the instrumental dead-time. The 8-step phase-cycle was implemented considering the computation by Stoll and Kasumaj.[15]

Analysis and simulations were done on MATLAB with the EasySpin toolbox development versions (6.0.0-dev.x).[16]

Bibliography

(1) Martino, G. A.; Piovano, A.; Barzan, C.; Liao, Y. K.; Morra, E.; Hirokane, K.; Chiesa, M.; Monoi, T.; Groppo, E. *Journal of Catalysis* **2021**, *394*, 131–141 (cited on page 35).

(2) Barker, G. K.; Lappert, M. F.; Howard, J. A. K. *Journal of the Chemical Society, Dalton Transactions* **1978**, 734 (cited on page 35).

(3) Monoi, T.; Ikeda, H.; Sasaki, Y.; Matsumoto, Y. *Polymer Journal* **2003**, *35*, 608–611 (cited on page 35).

(4) Zhu, Z.; Kevan, L. *Physical Chemistry Chemical Physics* **1999**, *1*, 199–206 (cited on page 36).

(5) Liao, Y. K.; Bruzzese, P. C.; Hartmann, M.; Pöppl, A.; Chiesa, M. *Journal of Physical Chemistry C* **2021**, *125*, 8116–8124 (cited on page 36).

(6) Morra, E.; Martino, G. A.; Piovano, A.; Barzan, C.; Groppo, E.; Chiesa, M. *Journal of Physical Chemistry C* **2018**, *122*, 21531–21536 (cited on page 36).

(7) Martino, G. A.; Piovano, A.; Barzan, C.; Rabeah, J.; Agostini, G.; Bruekner, A.; Leone, G.; Zanchin, G.; Monoi, T.; Groppo, E. *ACS Catalysis* **2020**, *10*, 2694–2706 (cited on page 37).

(8) Freude, D.; Ernst, H.; Hunger, M.; Pfeifer, H.; Jahn, E. *Chemical Physics Letters* **1988**, *143*, 477–481 (cited on page 37).

(9) Lagostina, V.; Salvadori, E.; Chiesa, M.; Giamello, E. *Journal of Catalysis* **2020**, *391*, 397–403 (cited on page 38).

(10) Abdo, S.; Howe, R. F. *Journal of Physical Chemistry* **1983**, *87*, 1722–1730 (cited on page 38).

(11) Salikhov, K. M.; Dzuba, S. A.; Raitsimring, A. M. *Journal of Magnetic Resonance (1969)* **1981**, *42*, 255–276 (cited on page 39).

(12) Höfer, P.; Grupp, A.; Nebenführ, H.; Mehring, M. *Chemical Physics Letters* **1986**, *132*, 279–282 (cited on page 39).

(13) Höfer, P. Distortion-Free Electron-Spin-Echo Envelope-Modulation Spectra of Disordered Solids Obtained from Two-Dimensional and Three-Dimensional HYSCORE Experiments, 1994 (cited on page 39).

(14) Song, R.; Zhong, Y. C.; Noble, C. J.; Pilbrow, J. R.; Hutton, D. R. *Chemical Physics Letters* **1995**, *237*, 86–90 (cited on page 39).

(15) Stoll, S.; Kasumaj, B. *Applied Magnetic Resonance* **2008**, *35*, 15–32 (cited on page 39).

(16) Stoll, S.; Schweiger, A. *Journal of Magnetic Resonance* **2006**, *178*, 42–55 (cited on page 39).

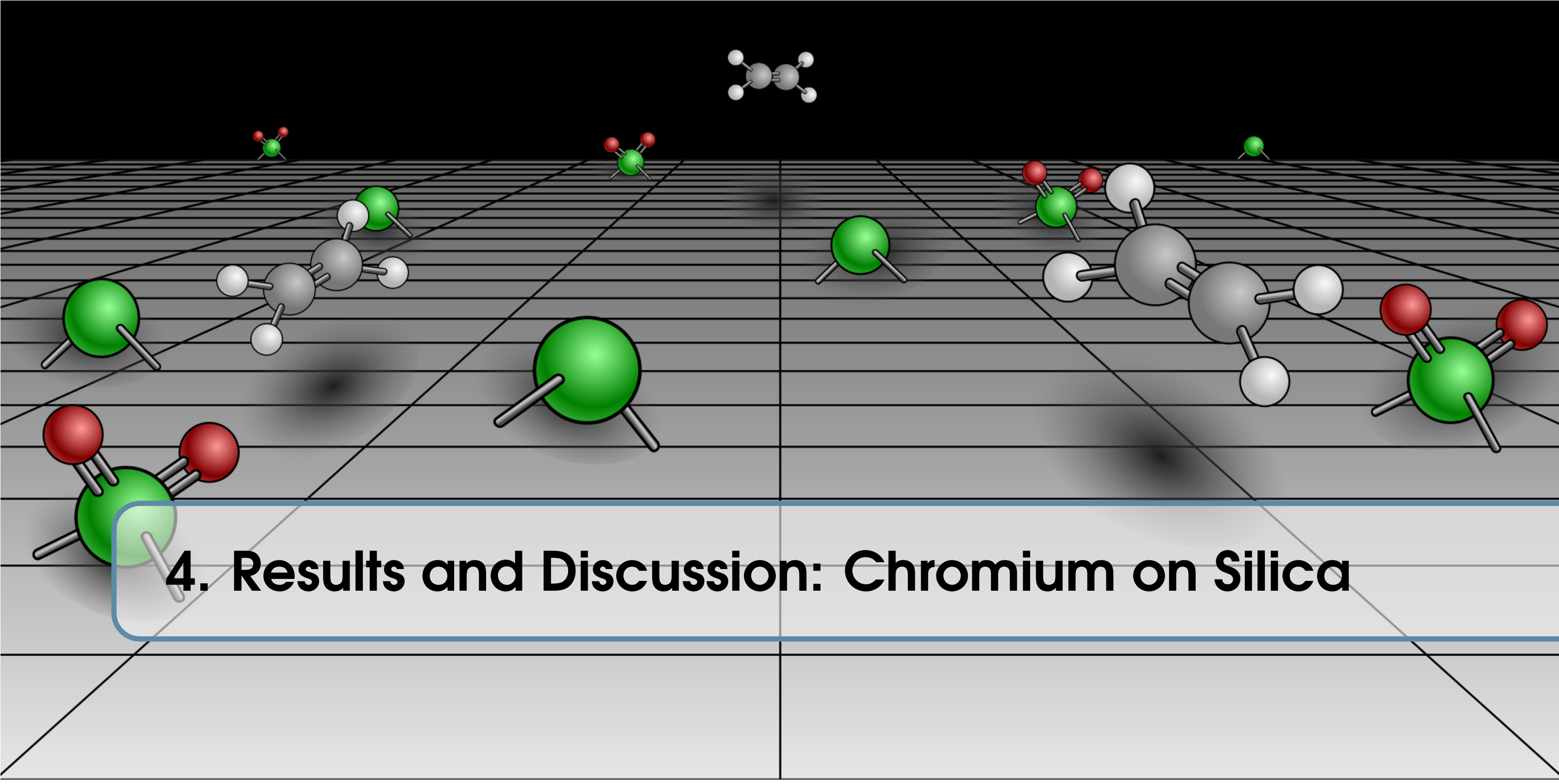

4. Results and Discussion: Chromium on Silica

In this chapter, I discuss the results obtained for the paramagnetic Cr species grafted on the silica surface, which include the pristine Phillips catalysts and the model organometallic-Cr catalysts. These works mainly focus on structural and quantitative study of the Cr-species on the silica surface.

4.1 Phillips Catalyst

The activation of the Phillips catalyst removes the excessive hydroxyl groups and grafts the hexavalent chromium at the remaining silanol sites as chromate or dichromate. [1, 2] The dominant Cr species in the catalyst are the diamagnetic Cr(VI), while small amount of residual paramagnetic Cr(V) species ($S{=}1/2$, $3d^1$) are still present in the catalyst.[3, 4] Even though the idea of the Cr(V) species being the active sites has long been abandoned,[1, 3, 5] the work reported by E. Morra and coworkers[4] has shown some correlation between the Cr(V) species and the Cr(III) species which occur in the catalyst after reaction with ethylene. On the other hand, Cr(III) is considered a possible candidate of the active site.[2] Unfortunately, the Cr(III) species give no electron spin echo signal that limits the access to information like long-range spin-spin interaction, superhyperfine interaction, etc. As a result, I focused on investigating the Cr(V) species with pulsed EPR techniques in addition. And the results help to find more information about the catalyst and probe the local environment of the potential active sites.

4.1.1 Coordination of Cr(V)

The activated catalysts with 4 different Cr concentrations (1, 0.5, 0.1, 0.05 wt%) were measured with CW-EPR at 77 K. (Fig.4.1) Spectra have shown microwave resonance occuring between magnetic field of 335 and 365 mT. The signals are consistent with the reported residual Cr(V) species.[3–5] The peak at 342 mT indicates that the presence of a second Cr(V) species. Assuming that the two species have different relaxation times, two EDFS methods were used to disentangle the overlapping signals of the two species.

Firstly, comparing the EDFS spectrum (Fig4.2a) measured with 5100 μs shots repetition time (srt, the delay time between acquisition points) and the spectrum measured with srt = 510 μs, we can see the spectrum measured with shorter srt has smaller signal intensity between 340 and 347

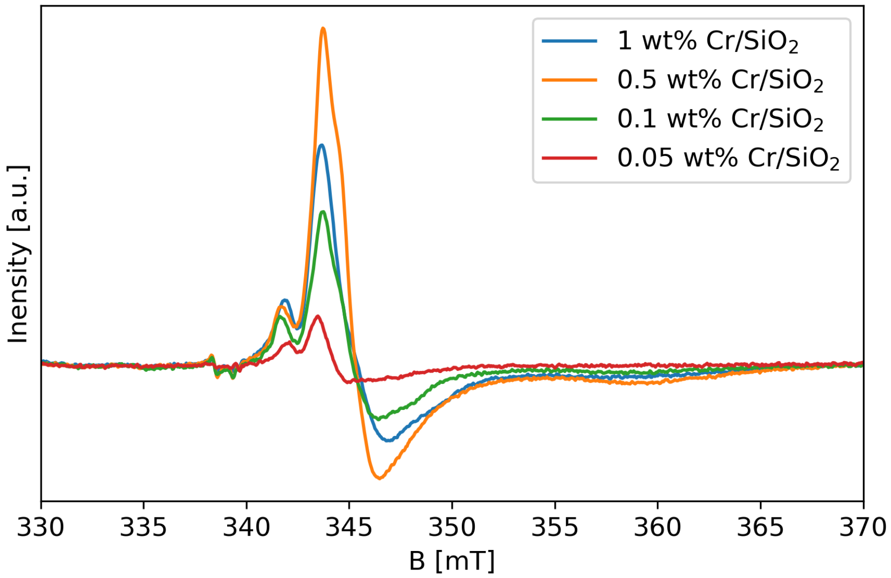

Figure 4.1: The X-band CW-EPR of the activated Phillips catalysts with different Cr concentrations measured at 77 K.

mT, while the other part of the spectra remain the same. This indicates that the assumed second species has a longer T_1 and the magnetization of it can not fully relax back to the z-axis before another acquisition. By subtracting the spectrum recorded with shorter srt from the one recorded with longer srt, the signal of the second species can be separated.

A second method, T_1 filtered EDFS, was used to validate this information. Inversion recovery experiment (π-T-$\frac{\pi}{2}$-τ-π-τ-echo) measured at 356 mT, at which no microwave resonance for the second species can occur, showed that when $T = 76$ μs the magnetization in z-direction becomes zero for the first species. Sweeping the field with this T can filter out the signal from the first species in the EDFS spectrum. Meanwhile, the inversion recovery experiment measured at 342 mT shows that the magnetization is still at (-z)-direction. This gives the EDFS spectrum in negative intensity. Fig.4.2b shows the normal EDFS alongside the T_1 filtered EDFS with the inversion recovery experiment in the inset. These experiments thus clearly show that the signal is composed of two Cr(V) species.

The first species has the more intense signal intensity that peaks at 345 mT with a shoulder extending to higher field until 365 mT, named as Cr(V)A species in the following texts. On the other hand, the second species peaks at 344 mT with a shoulder extending to lower field until 340 mT, named as Cr(V)B. A preliminary observation is that the two species are both in the axial symmetry; however, Cr(V)A has $g_\perp > g_\parallel$ while Cr(V)B has $g_\perp < g_\parallel$. To obtain the spin Hamiltonian parameters of the two Cr(V) species, simulations are needed.

The simulations in Fig.4.3 indicate a slightly rhombic g-tensor for Cr(V)A and an axial g-tensor for Cr(V)B. (Tab. 4.1) Due to the broad linewidth and the low natural abundance (9.5%) of the isotope ^{53}Cr(I=3/2), no hfi is resolved from the spectra. The g-tensor for Cr(V)A was assigned to a distorted tetrahedral coordination and is consistent with previous works.[4–6] Literature data for this second species report a g-tensor characterized by $g_\perp > g_\parallel$[4, 5] while the simulation of Cr(V)B indicates the opposite. This suggests a very different coordination for Cr(V)B. Other works on the $(CrO_4)^{3-}$ chromate in different complexes reported axial g-tensor with $g_\perp < g_\parallel$.[7–10] These Cr(V)

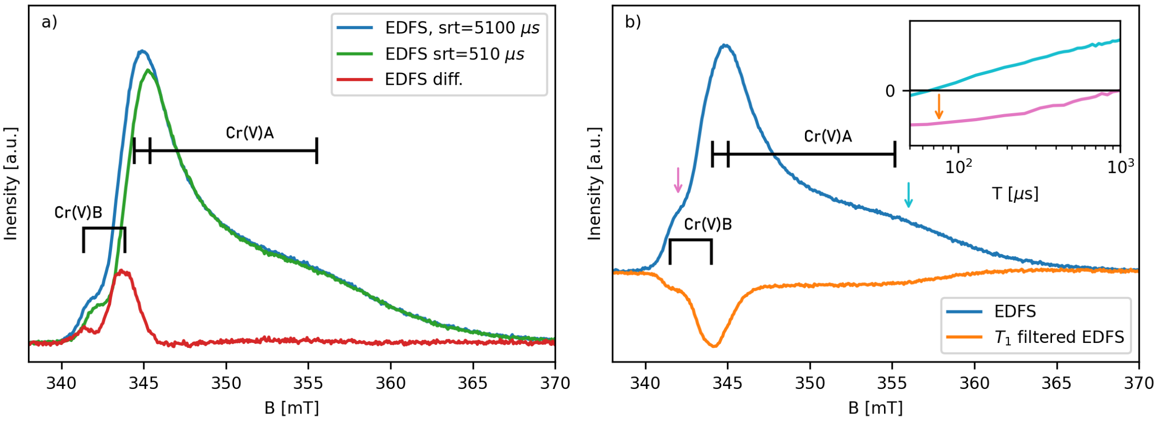

Figure 4.2: The X-band EDFS spectra of the 0.1 wt% Phillips catalyst measured at 10 K. a) the EDFS spectra measured with srt = 5100 (blue) and 510 (green) μs and the difference between the two (red). b) The normal EDFS spectrum (blue) and the T_1 filtered EDFS spectrum (orange) with $T = 76\mu$s. The inset shows the T_1 experiments measured at field positions indicated by the arrow of the same colors. The orange arrow shows how the constant T for the T_1 filtered EDFS reflects the signal intensity for the T_1 filtered EDFS spectrum.

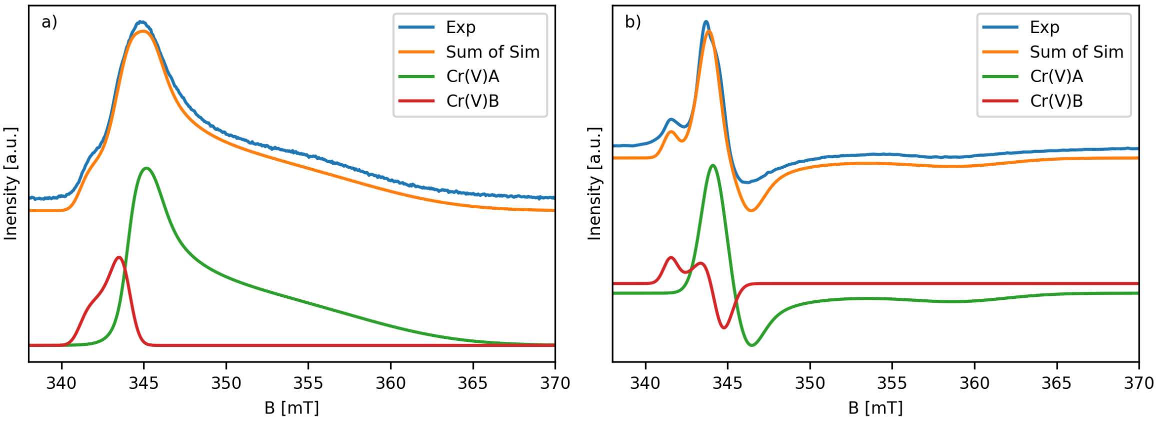

Figure 4.3: The X-band CW-EPR and EDFS spectra of 0.1 wt% Cr Phillips catalyst with the simulation of the two Cr(V) species and the sum of them.

	g_x	g_y	g_z	Ref.
	$g_\perp$		$g_\parallel$	
Cr(V)A	1.972 ± 0.002	1.963 ± 0.002	1.885 ± 0.002	This work
Cr(V)B	1.971 ± 0.003		1.988 ± 0.002	This work
Morra et al.	1.978	1.968	1.89	[4]
	1.988		1.91	
Weckhuysen et al.	1.978	1.969	1.895	[5]
	1.979		1.939	
Van Reijen et al.	1.975		1.898	[6]

Table 4.1: The spin Hamiltonian parameters for Cr(V) in the Phillips catalyst from this work and some literature.

species were assigned also with distorted tetrahedral coordination, but for a d_{z^2} ground state (i.e. elongation along the principle z-axis). Considering the perturbation theory, the spin Hamiltonian parameters are given by[7]

$$\begin{cases} g_\parallel = g_e \\ g_\perp = g_e - \frac{6\lambda}{E(xz,yz)-E(z^2)} \end{cases} \tag{4.1}$$

,with the spin-orbit coupling parameter λ, and the deviation of $g_\parallel$ was attributed to a third order effect that the $d_{(x^2-y^2)}$ state mixing with the d_{z^2} ground state as

$$\psi_{z^2} = ad_{z^2} + bd_{x^2-y^2}. \tag{4.2}$$

This should result in breaking the axial symmetry and makes $g_x \neq g_y$. But for Cr(V)B, considering the linewidth and the small deviation between $g_\parallel$ and $g_\perp$, the rhombic g-tensor might not be resolved.

4.1.2 Reactivity of Cr(V)

The reactivity of Cr(V) ions were investigated during their reaction with ethylene. The same reaction were reported for the 0.5 wt% Cr Phillips catalyst.[4] As studies suggested that the Cr activity is increased over decreasing loading,[1] this part of the experiment was conducted on the two samples with lower concentrations (0.1, 0.05 wt% Cr) to examine the difference between them and the 0.5 wt% Cr Phillips catalyst.

The CW-EPR spectra of the 0.1 wt% Cr sample reacted with ethylene is shown in Fig.4.4. After 300 min of reaction, a new signal emerged at low field around 160-190 mT. This is characteristic for Cr(III) (S=3/2, $3d^3$) with large zfs and small orthorhombic distortion.[11–13] ($D > 30$ MHz and $E/D = 0.022 \pm 0.005$ were obtained from computer simulation). Meanwhile, the signal intensity for Cr(V)A dropped significantly upon the emergence of Cr(III). The spectra are consistent with the work reported for the 0.5 wt% Cr sample, while showing a big difference in the timing. It was reported that the Cr(III) species emerged after 10 min of reaction, while here it took more than 180 min to observe this species.[4]

To give a quantitative analysis, each spectrum was simulated with the given spin Hamiltonian parameters and optimized with the line shape using the least-square fitting tool $esfit$ in the EasySpin

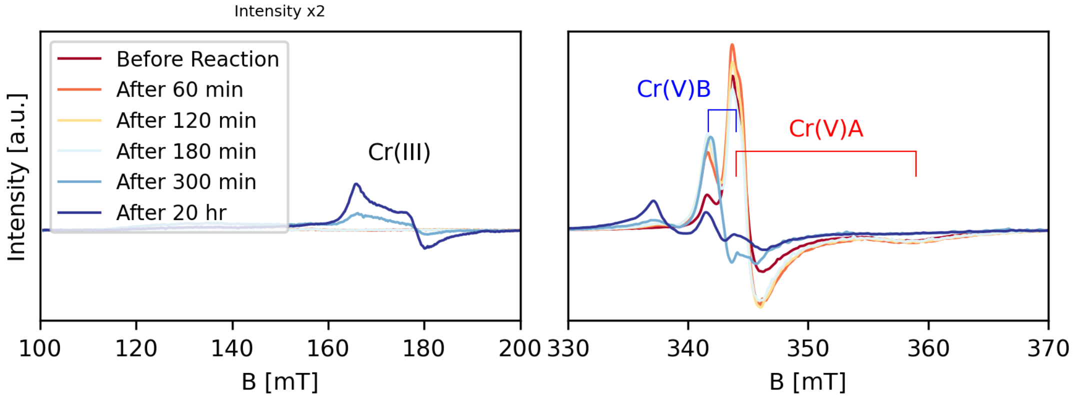

Figure 4.4: The CW-EPR spectra of the 0.1 wt% Cr Phillips catalyst at 77 K during the reaction with ethylene.

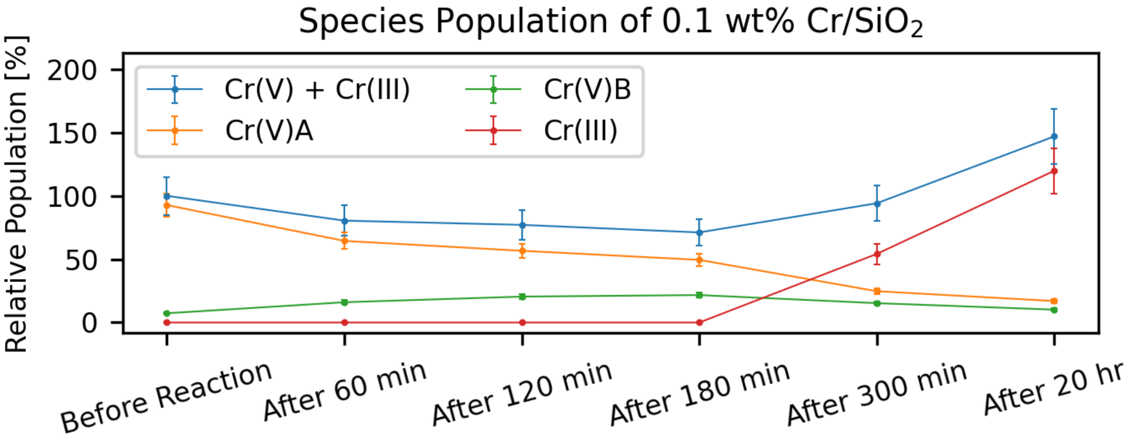

Figure 4.5: The relative population of the paramagnetic Cr species during the reaction with ethylene of 0.1 wt% Cr Phillips catalyst. The initial amount of the paramagnetic Cr is set to be 100 % percent of the relative population.

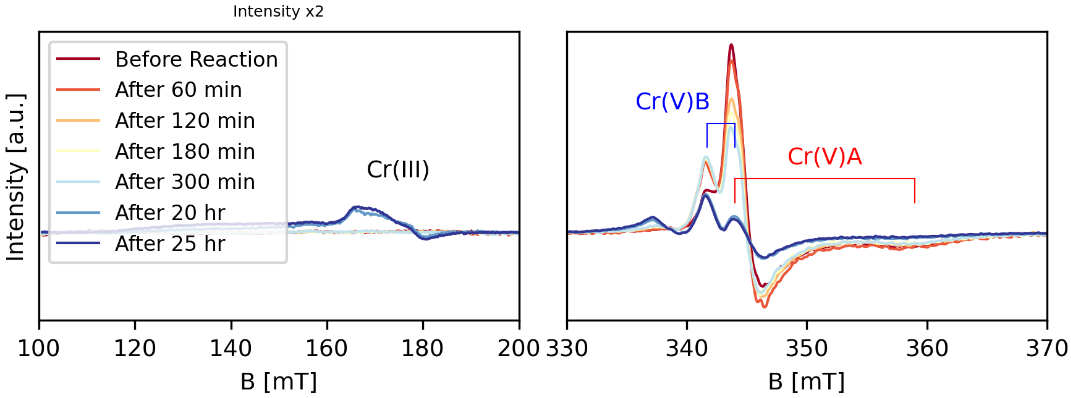

Figure 4.6: The CW-EPR spectra of the 0.05 wt% Cr Phillips catalyst at 77 K during the reaction with ethylene.

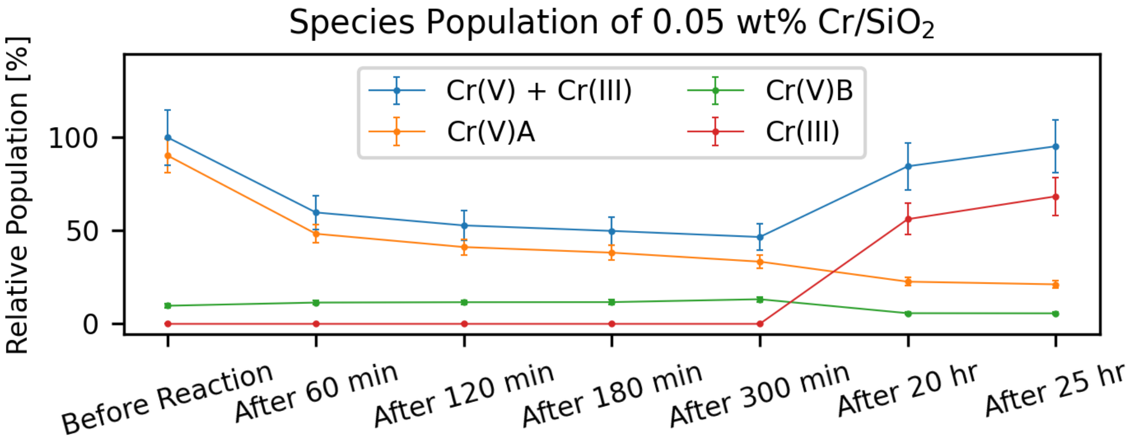

Figure 4.7: The relative population of the paramagnetic Cr species during the reaction with ethylene of 0.1 wt% Cr Phillips catalyst. The initial amount of the paramagnetic Cr is set to be 100 % percent of the relative population.

toolbox.[14] The different Cr species were simulated with individual scaling factors and the relative populations were determined accordingly. The results (Fig.4.5) show that since the reaction started, the amount of Cr(V)A started to decrease slowly while Cr(V)B increased by a small amount and the total amount of paramagnetic Cr stayed at the same level in the meantime until 180 min. After 300 min of reaction, a significant increase for the Cr(III) accompanied by the drop of the proportion of the two Cr(V) species. Among to two Cr(V) species, it is clear that Cr(V)A is more reactive than Cr(V)B. The trend continued after 20 hr of reaction and the total amount of paramagnetic Cr exceeded the initial value.

The same experiment was repeated for the 0.05 wt% Cr sample as shown in Fig.4.6. For this sample, the Cr(III) species emerged after even a longer time of reaction (20 hr). The quantitative analysis (Fig.4.7 showed a more steep decline in the amount of Cr(V)A while the growth of Cr(V)B is not as much as that of it in the 0.1 wt% Cr sample. This suggests that the Cr(V)A species is more reactive while Cr(V)B behaves otherwise. Similarly, the signal from both Cr(V) species decreased as Cr(III) emerged. At the same time, the total amount of the paramagnetic Cr increased.

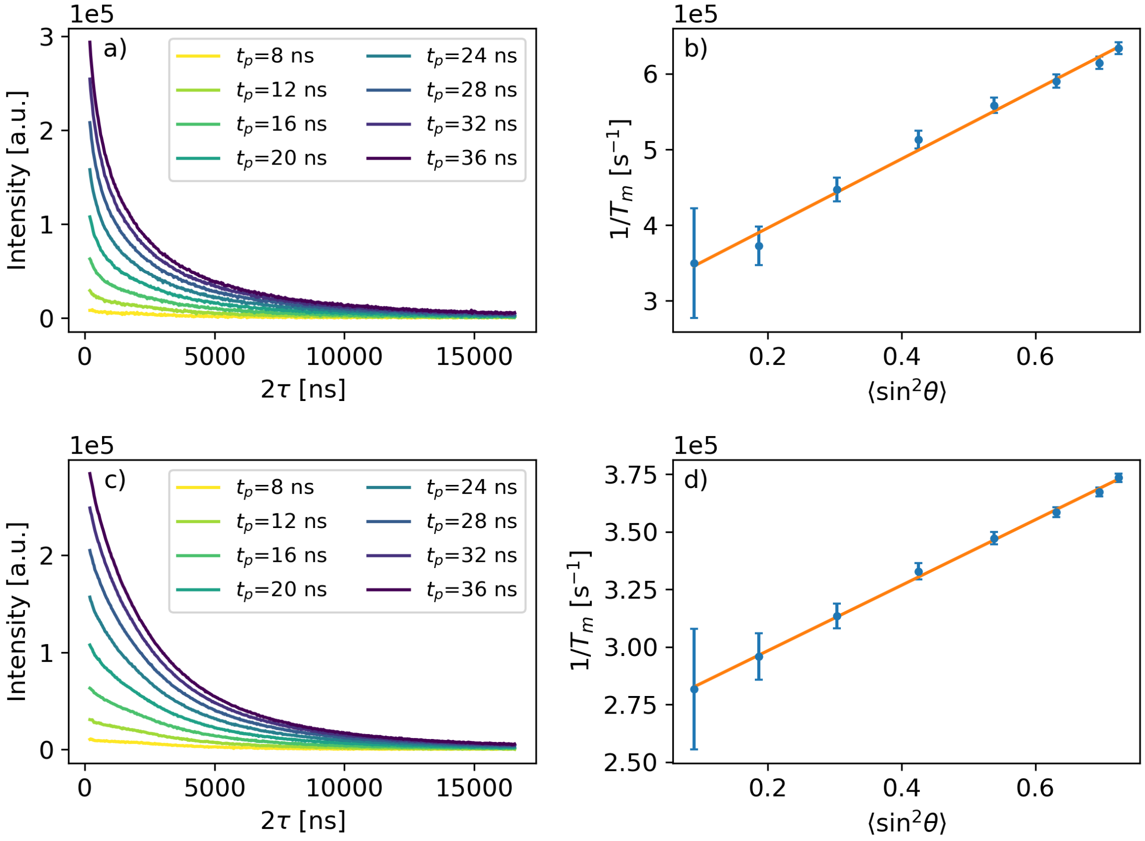

Figure 4.8: The spin-spin relaxation experiment at X-band of the 1 (a, b) and 0.5 (c, d) wt% Cr Phillips catalyst. The T_m measured with different pulse length of the second pulse (t_p). (a, c) And the instantaneous diffusion analysis with $1/T_m$ over the $\langle \sin^2 \theta \rangle$. (b, d)

Tracing the change of the population of each paramagnetic Cr, the analysis suggested there is no clear indication of the correlation between the Cr(V) and Cr(III). If the Cr(III) is reduced from Cr(V), the total amount of the paramagnetic Cr should remain unchanged. The inconsistency of the value indicates that both Cr(V) and Cr(III) had experienced the redox reaction from/to a pre-existing diamagnetic Cr oxidation state.

4.1.3 Distribution of Cr(V)

To understand how the (di-)chromate is dispersed on the silica, the distribution of Cr(V) in the activated sample was investigated, assuming it can reflect the overall distribution of the dominant diamagnetic Cr(VI). This experiment was conducted on the 1 and 0.5 wt% Cr samples as they give sufficient echo intensity for the instantaneous diffusion technique.

Fig.4.8a,c show the T_m measured with different second pulse (t_p) length and that the relaxation time increased with shorter t_p. This is according to the theory[15] that with smaller turning angle, less excited electron spins (A-spins) interact with each other and leads to smaller instantaneous diffusion effect. The measured T_m cannot be fit with the simple exponential decay function but with the stretched exponential function.

$$f(t) = a \cdot exp(-(\frac{2\tau}{T})^{\beta}) + b \tag{4.3}$$

Sample	Instantaneous Diffusion (m^{-3})	Spin Counting (m^{-3})
1 wt% Cr/SiO$_2$	$3.6\pm0.7\times10^{23}$	$1.1\pm0.3\times10^{23}$
0.5 wt% Cr/SiO$_2$	$1.1\pm0.8\times10^{23}$	$3.6\pm1.0\times10^{22}$

Table 4.2: Spin concentration of the 1 and 0.5 wt% Cr Phillips catalyst with instantaneous diffusion analysis and spin counting.

This can be interpreted as a distribution for the relaxation time (T_m). I took the mean value

$$\langle T\rangle = \frac{T}{\beta}\Gamma\left(\frac{1}{\beta}\right) \tag{4.4}$$

with Γ the gamma function as the T_m of the sample for the instantaneous diffusion analysis. Plotting the reciprocal of T_m over $\langle \sin^2 \frac{\theta}{2}\rangle$ (Fig.4.8b, d) and fit the results with a linear function, the concentration is obtained as the slope (Eq. 2.44,2.45). The results (Tab. 4.2) show that the Cr(V) concentrations are higher than the concentration obtained by spin counting by a factor of 3. Considering that the instantaneous diffusion effect is originated from the electron spin-spin interaction, the concentration obtained this way can be treated as a local concentration. Meanwhile, the spin counting experiment takes all the unpaired electron in the sample into account. It can be seen as the mean concentration across the whole sample filled in the EPR tube. This can indicate Cr(V) clusters are formed in the samples.

4.2 Organometallic-Cr on Silica

As a complementary study, I investigated the structure of chromium sites in silica-supported Cr[CH(SiMe$_3$)$_2$]$_3$ catalysts as a function of the chromium loading, in an effort to correlate it with the catalytic performances. This activity was part of a collaboration with the group of Prof. E. Groppo.[16] According to the works of Monoi et al.,[17] heterogeneous catalysts prepared by supporting tris[bis(trimethylsilyl)methyl]chromium(III), Cr[CH(SiMe$_3$)$_2$]$_3$, on a silica pre-calcined at high temperature, have a high activity towards ethylene polymerization, even without using any organo-aluminum compounds as co-catalysts or scavengers. These catalysts display characteristics similar to those of the Phillips catalyst (in terms of molecular weight, molecular weight distribution, copolymerization ability, and presence of LCB), prompting the conclusion that the active sites in the Phillips catalyst should resemble the active sites in the Cr[CH(SiMe$_3$)$_2$]$_3$/SiO$_2$ catalysts. This section focuses on characterizing the local structure of the grafted Cr(III) and quantitative analysis to identify the functionality of the Cr(III).

4.2.1 Structure of the Grafted Cr

To start with the investigation of the nCr[CH(SiMe$_3$)$_2$]$_3$/SiO$_2$ catalysis, the Cr[CH(SiMe$_3$)$_2$]$_3$ precursor was analysed and compared with the hexa-aquo Cr(III) complex. The CW-EPR spectrum (Fig.4.9(1)) of Cr[CH(SiMe$_3$)$_2$]$_3$ is characterized by a pseudo-axial pattern with the effective g-values $g_\perp \approx 4.0$ and $g_\parallel \approx 2.0$, the latter signal being rather weak. Assuming g-value of 1.98, analysis indicates that the $D \geq 23$ GHz and $E \approx 0$ are required to match the effective g-values.[4, 18–20] The axial symmetry of the zfs tensor is consistent with the D_{3h} symmetry that is interpreted with the transmission UV-vis spectrum.[16] Meanwhile, the spectrum of the CrCl$_3$ aqueous solution (Fig.4.9(2)) shows a completely different spectrum, characterized by a broad feature at the effective

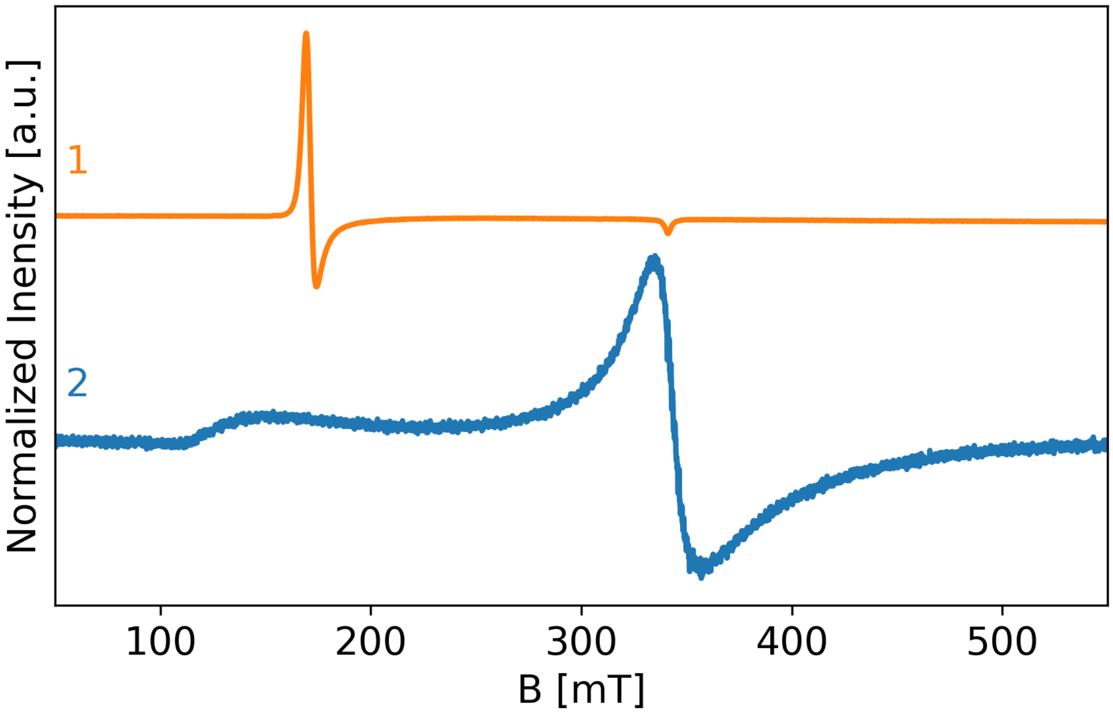

Figure 4.9: The CW-EPR spectra of (1) Cr[CH(SiMe$_3$)$_2$]$_3$ in hexane and (2) CrCl$_3$ in water at 77 K. The concentrations of the solutions are at the order of 10^{-3}M.

$g \approx 2.0$ and the weaker component at $g \approx 4.0$. This is documented in the literature as Cr(III) in nearly octahedral coordination, either in a hexa-aquo complex or in a cluster form, of which the distortion to the degree of symmetry is reflected by the intensity at effective $g \approx 4.0$.[3, 5, 21–23]

The CW-EPR spectra of the 4 catalysts are shown in Fig.4.10a. The spectra features in both the low ($g \approx$4.0) and central ($g \approx 2.0$) field regime are significantly different compared to the precursor. At the central field regime, all spectra showed sharp signals at $g \approx 1.98$ that can be simulated assuming $S = 1/2$ species with slightly rhombic g-tensors. (Fig.4.10b) They are characteristic of Cr(V) species, considered as adventitious impurities of Cr on silica and are negligible for catalysis similar to the that discussed in the previous section. Therefore, they won't be further commented later on. Whereas at low field, the complex spectral shape reflects the orthorhombic distortion of the grafted Cr(III) species. The degree of orthorhombic distortion can be analysed with the help of the rhombogram (Fig.4.11), which describes the splitting of the $m_S = +\frac{1}{2} \leftrightarrow -\frac{1}{2}$ transitions centered at $g \approx 4.0$ over the E/D value in a weak field limit ($D \gg \beta_B g B_0$).[24] The simulation (Fig.4.10b, 3-5) refining the zfs provides evidence of the presence of different Cr(III) species that can be attributed in two groups characterized by the different zfs parameters. Note that these species remain the same across all 4 samples with only the changes in relative amounts, indicating that the grafting reaction does not depend on the concentrations of these samples. The simulated spectrum of each Cr species is shown Fig.4.10b and the corresponding spin Hamiltonian parameters are reported in Tab. 4.3.

The first group among the two, Cr(III)A, is characterized by the significantly large D and the largest orthorhombic distortion E/D among all simulated Cr(III) species. Due to the large zfs

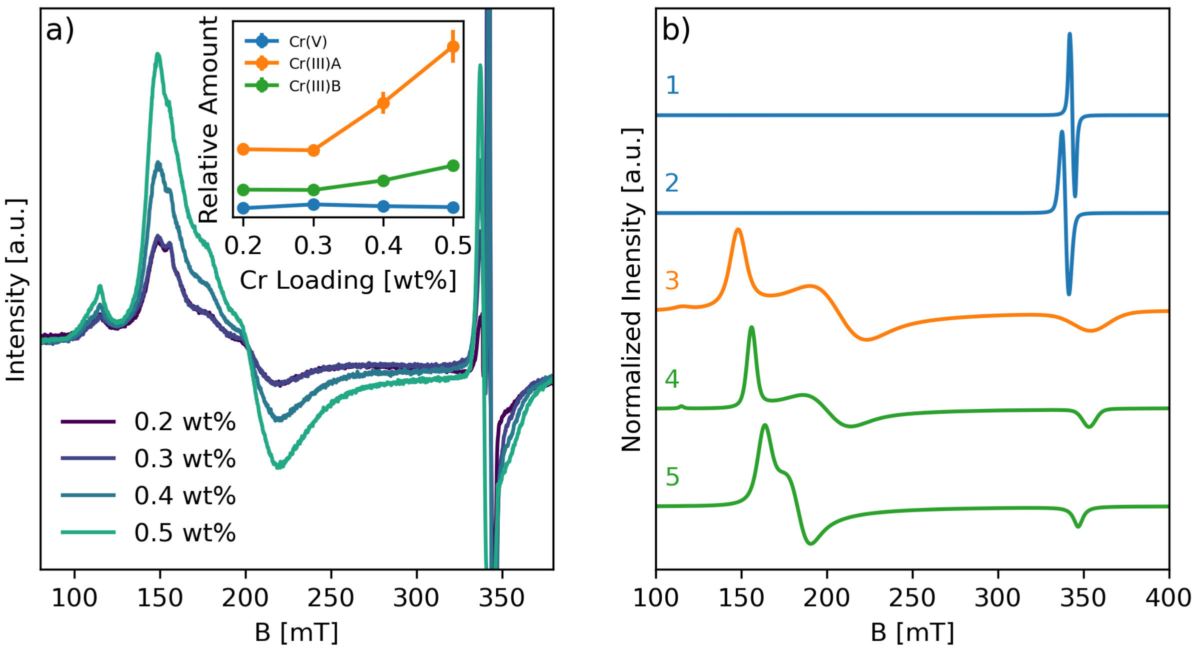

Figure 4.10: The CW-EPR spectra of the a) experiments of the nCr[CH(SiMe$_3$)$_2$]$_3$/SiO$_2$ and the relative amount of different Cr sites in the inset and b) each simulated Cr species. In b) the Cr species are Cr(V)$_{1,2}$: (1)&(2), Cr(III)A: (3), and Cr(III)B$_{1,2}$: (4)&(5).

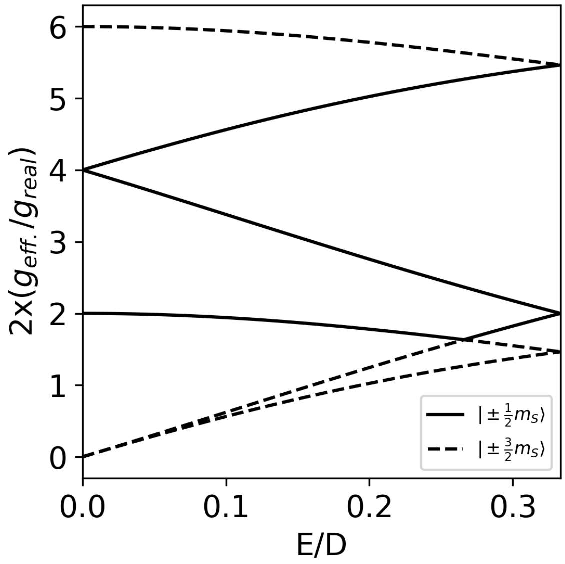

Figure 4.11: The rhombogram for S=3/2 species assuming $D \gg \beta_B g B_0$ and orthorhombic distortion $0 < E/D < 1/3$. The solid lines are the $m_S = +\frac{1}{2} \leftrightarrow -\frac{1}{2}$ transitions and the dashed lines are the $m_S = +\frac{3}{2} \leftrightarrow -\frac{3}{2}$ transitions.

	g_x	g_y	g_z	D [GHz]	E/D
Cr(V)$_1$	1.96(5)	1.97(5)	1.98(5)		
Cr(V)$_2$	-	-	1.99(9)		
Cr(III)A	1.98(5)	1.97(3)	1.97(0)	$\geq$87	1/9
Cr(III)B$_1$	1.98(0)	1.96(2)	1.97(0)	17$\pm$4	1/12
Cr(III)B$_2$	1.96(5)	1.99(8)	1.97(2)	19$\pm$4	1/30

Table 4.3: The spin Hamiltonian parameters of the Cr species in the nCr[CH(SiMe$_3$)$_2$]$_3$/SiO$_2$.

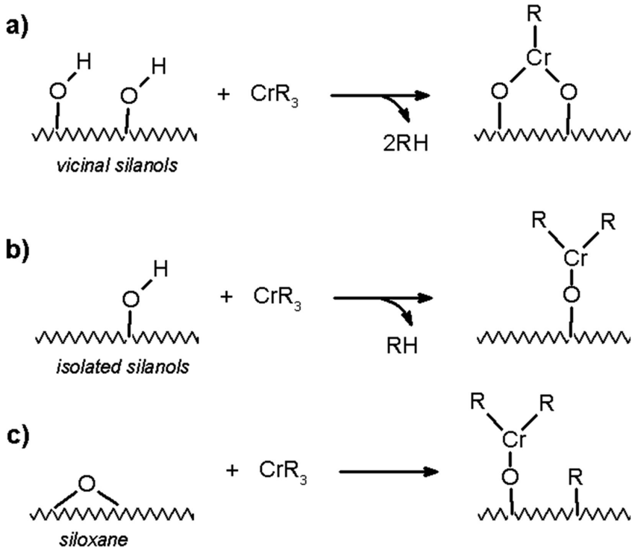

Figure 4.12: The scheme for Cr[CH(SiMe$_3$)$_2$]$_3$ grafting on silica surface by reaction with different surface functional groups. R stands for the CH(SiMe$_3$)$_2$ group.

parameters, this group is attributed to the isolated low-coordinated Cr(III) sites which is similar to the Cr[CH(SiMe$_3$)$_2$]$_3$ precursor but with a lower symmetry. It is in agreement with the DR UV-vis-NIR spectra showing similar bands correspond to that of the precursor.[16] Whereas the second group, Cr(III)B, consists of two Cr(III) species (Cr(III)B$_1$ and Cr(III)B$_2$) with smaller D and moderate E/D are assigned as surface-bound complexes with local distortions. It is correlated to the UV-vis bands of Cr(III) in octahedral field.

4.2.2 Quantitative Analysis of the Grafted Cr

Quantitative analysis of the nCr[CH(SiMe$_3$)$_2$]$_3$/SiO$_2$ was performed with the same method mentioned in the previous section. The relative amount of different Cr groups (inset of Fig.4.10a) is obtained with the optimized simulation as shown in Fig.4.13. The results show that Cr(III)A has the highest relative amount in the catalyst and has an increasing trend as a function of the Cr loading. Meanwhile, the amount of Cr(III)B is much lower and remained almost the same with the Cr loading.

Two types of Cr(III) sites are postulated by Monoi et al.[17] One formed when Cr[CH(SiMe$_3$)$_2$]$_3$ reacts with two vicinal silanols, releases two CH$_2$(SiMe$_3$)$_2$ groups, and gives the bis-grafted chromium species. (Fig.4.12a) The other site is by Cr[CH(SiMe$_3$)$_2$]$_3$ reacting with an isolated silanol (Fig.4.12b) or an opened siloxane bridge (Fig.4.12 and form a mono-grafted chromium species. Assuming the

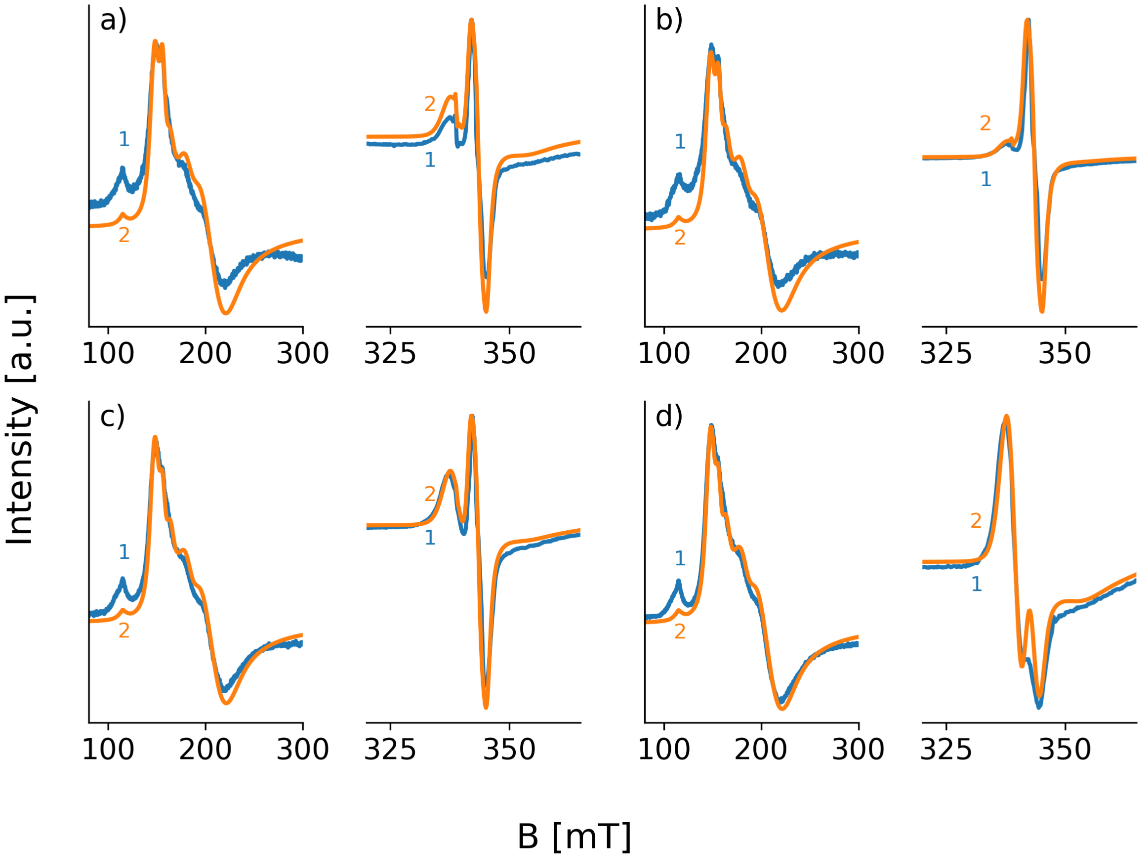

Figure 4.13: The (1) experimental and (2) simulated CW-EPR spectra of the $n\mathrm{Cr[CH(SiMe_3)_2]_3/SiO_2}$ for a) n=0.2, b) n=0.3, c) n=0.4, and d) n=0.5.

mono-grafted Cr(III) has spectroscopic properties more similar to the precursor and assign it to Cr(III)A; and the bis-grafted Cr(III) is assigned to Cr(III)B as it shows spectroscopic features of a chromium complex in a distorted octahedral field. This is consistent with the quantitative analysis. As the formation of the bis-grafted Cr species requires vicinal silanols which is more likely to be saturated with increasing Cr loading.

4.2.3 Reactivity of the Grafted Cr

Upon reaction with ethylene, studies showed that the number of short-chain branching in the produced polymer is increased with increased Cr loading.[17, 25] This can be associated with the mono-grafted Cr(III) sites oligomerizate ethylene to α-olefins (Cr_{oligom}) and the bis-grafted Cr(III) sites to the reaction of the ethylene polymerization and co-polymerization with the α-olefins (Cr_{polym}) according to the results of the quantitative analysis. This is supported by DR UV-vis-NIR spectra which compare the changes to bands that are likely masked by the formed PE and those aren't. The CW-EPR spectra recorded upon reaction the ethylene (Fig.4.14) show spectral changes in the low field region which represents a modification to the local environment. The change is expected for the mono-grafted Cr(III), hypothesizing a metallacycle mechanism for ethylene oligomerization,[1, 26–31] and considering the Cosee-Arlman polymerization mechanism on the bis-grafted Cr(III).[32] However, with all Cr(III) species overlapping in the low field region, direct assignment to the changes of each Cr site is difficult.

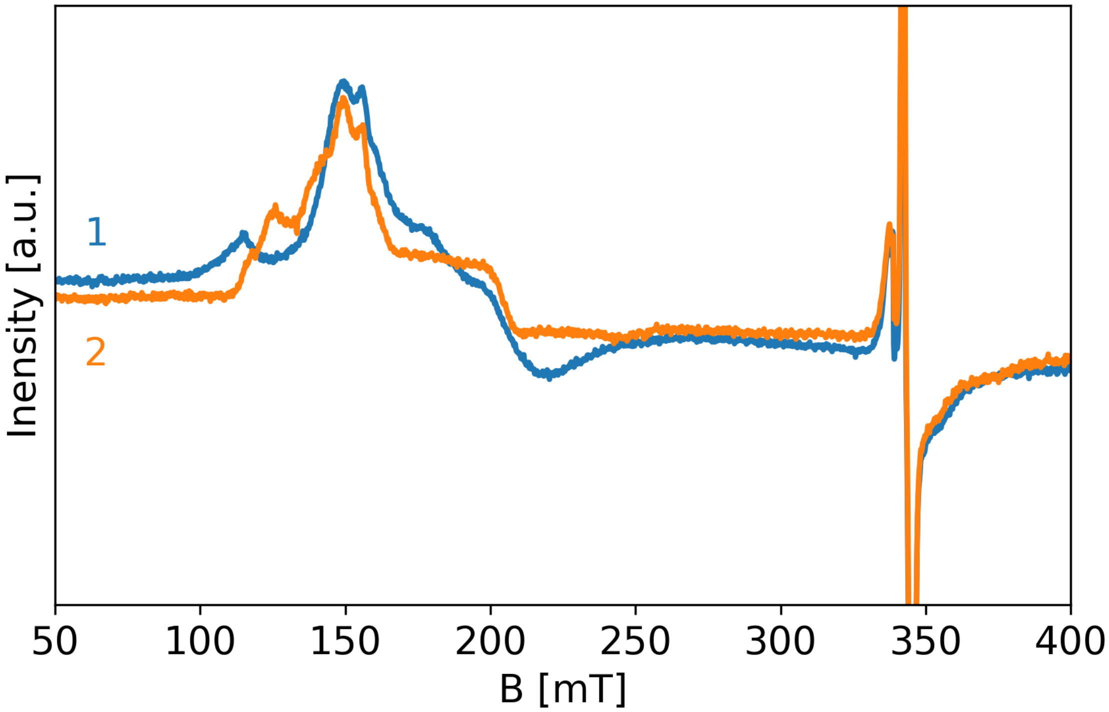

Figure 4.14: The CW-EPR spectra of the 0.2Cr[CH(SiMe$_3$)$_2$]$_3$/SiO$_2$ (1) before and (2) upon reaction with ethylene.

Bibliography

(1) McDaniel, M. P. In *Advances in Catalysis*, 1st edition; Elsevier Inc.: 2010; Vol. 53, pp 123–606 (cited on pages 41, 44, 52).

(2) Groppo, E.; Martino, G. A.; Piovano, A.; Barzan, C. *ACS Catalysis* **2018**, *8*, 10846–10863 (cited on page 41).

(3) Weckhuysen, B. M.; De Ridder, L. M.; Grobet, P. J.; Schoonheydt, R. A. *Journal of physical chemistry* **1995**, *99*, 320–326 (cited on pages 41, 49).

(4) Morra, E.; Martino, G. A.; Piovano, A.; Barzan, C.; Groppo, E.; Chiesa, M. *Journal of Physical Chemistry C* **2018**, *122*, 21531–21536 (cited on pages 41, 42, 44, 48).

(5) Weckhuysen, B. M.; Schoonheydt, R. A.; Mabbs, F. E.; Collison, D. *Journal of the Chemical Society - Faraday Transactions* **1996**, *92*, 2431–2436 (cited on pages 41, 42, 44, 49).

(6) Van Reijen, L. L.; Cossee, P. *Discussions of the Faraday Society* **1966**, *41*, 277 (cited on pages 42, 44).

(7) Greenblatt, M.; Pifer, J. H.; Banks, E. *Journal of Chemical Physics* **1977**, *66*, 559–562 (cited on pages 42, 44).

(8) Greenblatt, M.; Pifer, J. H. *The Journal of Chemical Physics* **1979**, *70*, 116–122 (cited on page 42).

(9) Greenblatt, M.; Pifer, J. H.; McGarvey, B. R.; Wanklyn, B. M. *The Journal of Chemical Physics* **1981**, *74*, 6014–6017 (cited on page 42).

(10) Banks, E.; Greenblatt, M.; McGarvey, B. R. *The Journal of Chemical Physics* **1967**, *47*, 3772–3780 (cited on page 42).

(11) Novosel, N.; Žilić, D.; Pajić, D.; Jurić, M.; Perić, B.; Zadro, K.; Rakvin, B.; Planinić, P. *Solid State Sciences* **2008**, *10*, 1387–1394 (cited on page 44).

(12) Shaham, N.; Cohen, H.; Meyerstein, D.; Bill, E. *Journal of the Chemical Society, Dalton Transactions* **2000**, *2*, 3082–3085 (cited on page 44).

(13) Hirscher, N. A.; Arnett, C. H.; Oyala, P. H.; Agapie, T. *Organometallics* **2020**, *39*, 4420–4429 (cited on page 44).

(14) Stoll, S.; Schweiger, A. *Journal of Magnetic Resonance* **2006**, *178*, 42–55 (cited on page 46).

(15) Salikhov, K. M.; Dzuba, S. A.; Raitsimring, A. M. *Journal of Magnetic Resonance (1969)* **1981**, *42*, 255–276 (cited on page 47).

(16) Martino, G. A.; Piovano, A.; Barzan, C.; Liao, Y. K.; Morra, E.; Hirokane, K.; Chiesa, M.; Monoi, T.; Groppo, E. *Journal of Catalysis* **2021**, *394*, 131–141 (cited on pages 48, 51).

(17) Monoi, T.; Ikeda, H.; Sasaki, Y.; Matsumoto, Y. *Polymer Journal* **2003**, *35*, 608–611 (cited on pages 48, 51, 52).

(18) Bradley, D. C.; Copperthwaite, R. G.; Cotton, S. A.; Sales, K. D.; Gibson, J. F. *Journal of the Chemical Society, Dalton Transactions* **1973**, 191–194 (cited on page 48).

(19) Eller, P. G.; Bradley, D. C.; Hursthouse, M. B.; Meek, D. W. *Coordination Chemistry Reviews* **1977**, *24*, 1–95 (cited on page 48).

(20) Delley, M. F.; Lapadula, G.; Núñez-Zarur, F.; Comas-Vives, A.; Kalendra, V.; Jeschke, G.; Baabe, D.; Walter, M. D.; Rossini, A. J.; Lesage, A.; Emsley, L.; Maury, O.; Copéret, C. *Journal of the American Chemical Society* **2017**, *139*, 8855–8867 (cited on page 48).

(21) Cordischi, D.; Occhiuzzi, M.; Dragone, R. *Applied Magnetic Resonance Quantitative EPR Spectroscopy: Comparison between Primary Standards and Application to MgO-MnO and a-Al203-Cr203 Solid Solutions*; technical report; 1999, pp 427–445 (cited on page 49).

(22) Landry, R. J.; Fournier, J. T.; Young, C. G. *The Journal of Chemical Physics* **1967**, *46*, 1285–1290 (cited on page 49).

(23) Barrera, J. A.; Wilcox, D. E. *Inorganic Chemistry* **1992**, *31*, 1745–1752 (cited on page 49).

(24) Hagen, W. R. In *Advances in Inorganic Chemistry*; C, 1992; Vol. 38, pp 165–222 (cited on page 49).

(25) Ikeda, H.; Monoi, T.; Sasaki, Y. *Journal of Polymer Science Part A: Polymer Chemistry* **2003**, *41*, 413–419 (cited on page 52).

(26) Delley, M. F.; Núñez-Zarur, F.; Conley, M. P.; Comas-Vives, A.; Siddiqi, G.; Norsic, S.; Monteil, V.; Safonova, O. V.; Copéret, C. *Proceedings of the National Academy of Sciences of the United States of America* **2014**, *111*, 11624–11629 (cited on page 52).

(27) Barzan, C.; Gianolio, D.; Groppo, E.; Lamberti, C.; Monteil, V.; Quadrelli, E. A.; Bordiga, S. *Chemistry – A European Journal* **2013**, *19*, 17277–17282 (cited on page 52).

(28) Brückner, A.; Jabor, J. K.; McConnell, A. E.; Webb, P. B. *Organometallics* **2008**, *27*, 3849–3856 (cited on page 52).

(29) Brückner, A. *Physical Chemistry Chemical Physics* **2003**, *5*, 4461–4472 (cited on page 52).

(30) Martino, G. A.; Piovano, A.; Barzan, C.; Bordiga, S.; Groppo, E. *Topics in Catalysis* **2018**, *61*, 1465–1473 (cited on page 52).

(31) Martino, G. A.; Piovano, A.; Barzan, C.; Rabeah, J.; Agostini, G.; Bruekner, A.; Leone, G.; Zanchin, G.; Monoi, T.; Groppo, E. *ACS Catalysis* **2020**, *10*, 2694–2706 (cited on page 52).

(32) Cossee, P. *Journal of Catalysis* **1964**, *3*, 80–88 (cited on page 52).

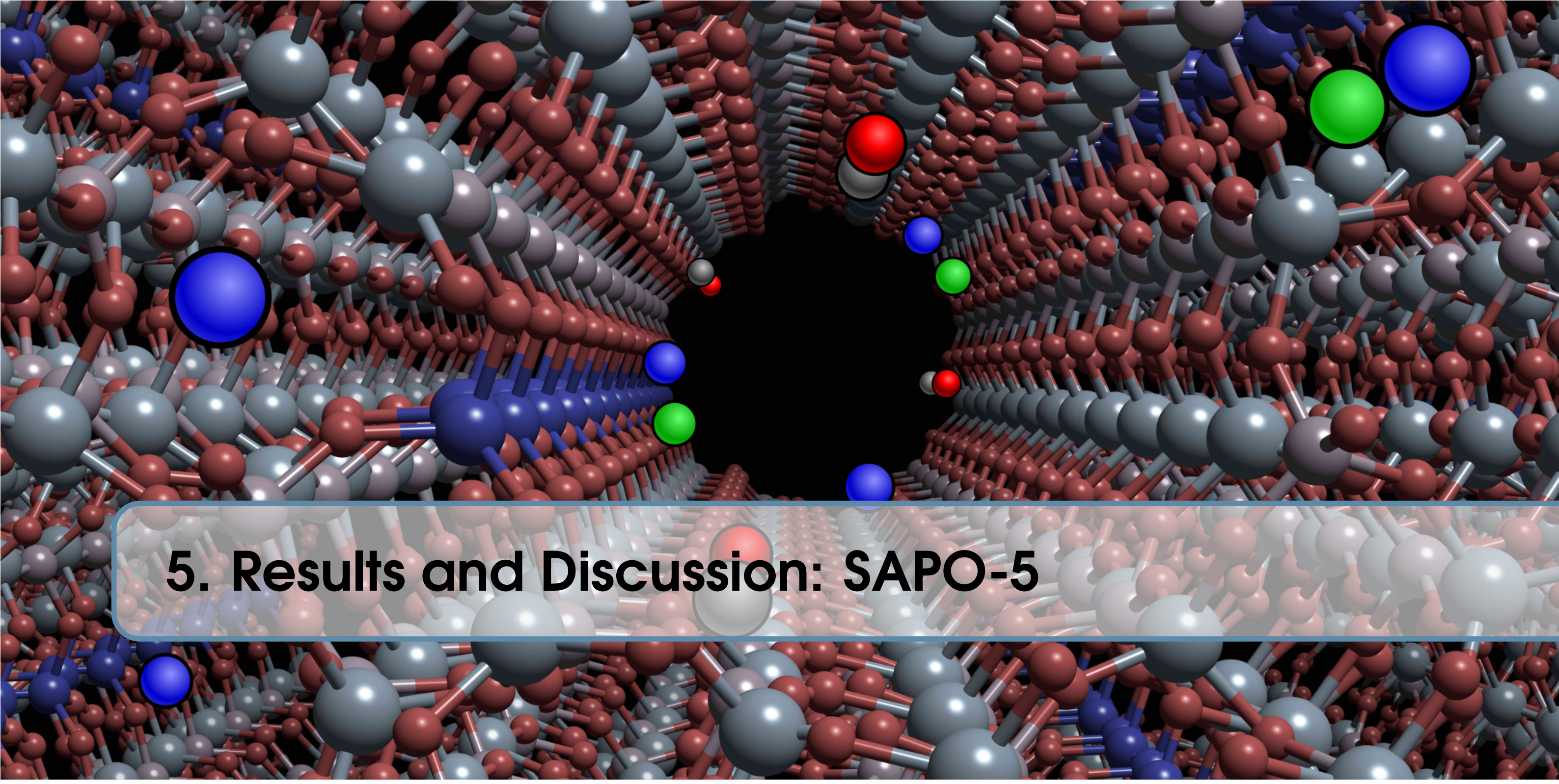

5. Results and Discussion: SAPO-5

In this chapter, I discuss the results from the study on the SAPO-5 with the AFI structure shown in Fig.5.1. The work includes various aspects of the electronic structure of SAPO-5: the investigation on the transition metal ions incorporated at the framework sites (Cr-SAPO-5), the bimetallic extra-framework sites (Mo/V-SAPO-5), and the reactivity towards NO molecules (NO-Adsorbed SAPO-5).

5.1 Cr-Incorporated SAPO-5

The EPR investigation of the Cr-SAPO-5 is a study corroborated by DFT modelling conducted by Paolo Cleto Bruzzese, a colleague within the PARACAT project. In this section, I present the results starting from CW-EPR experiment to track the change of Cr oxidation state after calcination, followed by hyperfine spectroscopy experiments to investigate the local environment of the Cr^{5+} species. This work is published on Journal of Physical Chemistry C in 2021.[1]

5.1.1 Coordination of the Pentavalent Cr

The CW-EPR spectra of the Cr-SAPO-5 is shown in Fig.5.2. The as-synthesized sample showed a broad signal between 120∼200 mT (g_{eff}=5.2∼3.2). This signal is characteristic of Cr^{3+} species in CrAlPO-5,[2] and CrAPSO-11[3] and is attributed to a distorted octahedral coordination.[3–6]

After calcination, part of the Cr^{3+} signal still contributes the spectrum, which indicates that the Cr^{3+} is highly stable and can be associated to isomorphous substitution, in agreement with the study reported by Padlyak et al.[2] Meanwhile, in the g≈ 2.0 region, the spectrum shows two new signals. The signal at g=2.0023 is due to a radical species formed during the removal of the template by calcination.[2] Whereas at $g\approx1.97$ the spectrum shows a axial signal that is assigned to a Cr^{5+} species in a CrO_4^{3-} unit. The spectrum can be simulated with a rhombic g-tensor assuming g_z=1.985±0.001, g_y=1.972±0.001, g_x=1.953±0.003. (Fig.5.3a) The same parameters can be used to fit the Q-band EDFS spectrum. (Fig.5.3b) The g-tensor obtained from simulation is in agreement with the DFT computation based on 3 different models which will be discussed in the next section. (Tab. 5.1)

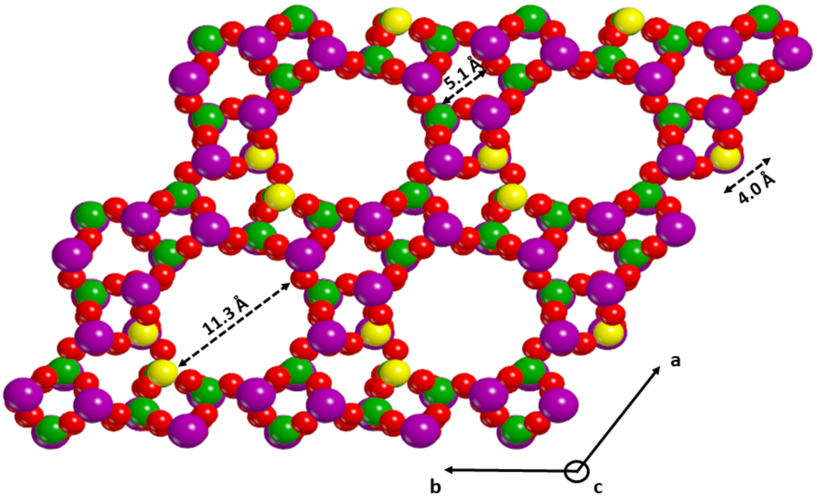

Figure 5.1: The structure of SAPO-5 viewing along the c-axis of the space filling periodic model. The dashed arrows report the size of the different pores. Si, Al, P, and O are in yellow, violet, green, and red respectively.

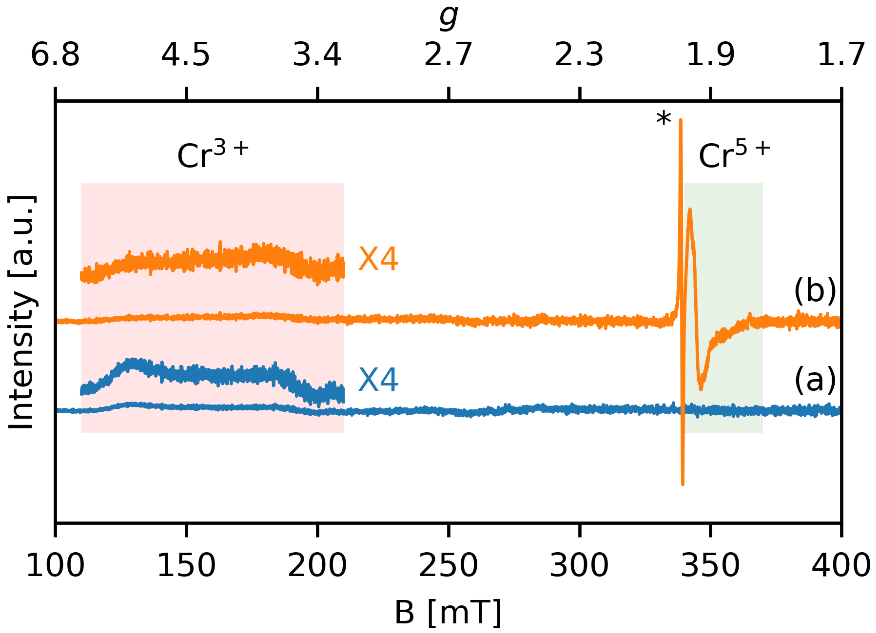

Figure 5.2: The CW-EPR spectra of the a) as-synthesized and b) calcined Cr-SAPO-5 sample recorded at 77 K. Red rectangular marked the region of Cr^{3+} signals and the green rectangular marked the region of Cr^{5+} signal. The asterisk marks the signal of the radical impurity occur in the calcined sample.

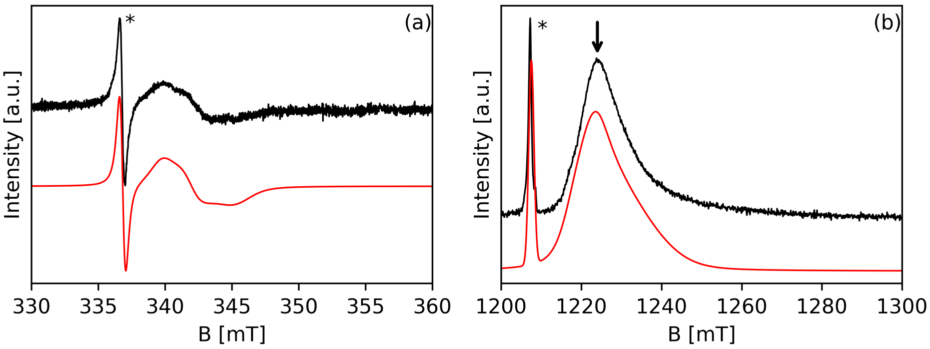

Figure 5.3: The a) X-band CW-EPR spectra at 77 K and b) Q-band EDFS spectra at 40 K of the Cr-SAPO-5. The black lines are the experimental spectra and the red lines mark the simulations. The arrow marks the field position of the HYSCORE measurements and the asterisks mark the radical impurity.

		g_x	g_y	g_z	Nuclei	a_{iso}	T_x	T_y	T_z
Simulated		1.953 ±0.003	1.972 ±0.001	1.985 ±0.001	^{27}Al(1)	0-2	-0.5 ±0.2	-0.5 ±0.2	1.0 ±0.4
					^{27}Al(2)	4-9	-0.9 ±0.3	-0.9 ±0.3	1.8 ±0.6
					^{27}Al(3)	13-17	-1.4 ±0.2	-1.4 ±0.2	2.8 ±0.4
					^{31}P	$\leq$0.1	-0.5 ±0.2	-0.5 ±0.2	1.0 ±0.4
Computed	Near-Si pair	1.953	1.979	1.987	^{27}Al$_1$	13.4	-1.6	-1.5	3.1
					^{27}Al$_2$	15.0	-1.4	-1.6	3.0
					^{27}Al$_3$	8.1	-0.9	-1.3	2.2
	Far-Si pair	1.955	1.977	1.990	^{27}Al$_1$	14.3	-1.5	-1.4	2.9
					^{27}Al$_2$	9.5	-1.4	-1.1	2.5
					^{27}Al$_3$	10.5	-1.1	-1.6	2.7
					^{27}Al$_4$	19.0	-1.9	-1.6	3.5
	Split-Si pair	1.952	1.978	1.985	^{27}Al$_1$	13.9	-1.7	-1.6	3.3
					^{27}Al$_2$	11.4	-1.2	-1.4	2.6
					^{27}Al$_3$	6.7	-0.8	-1.2	2.0

Table 5.1: Spin Hamiltonian parameters of ^{27}Al and ^{31}P and cluster computed g and periodic ^{27}Al *hfi* tensors elements at B3LYP-D3(ABC) level of theory relative to the atomistic Cr-SAPO-5 models. Ranges of a_{iso} values used in the simulation are given for the simulated spin Hamiltonian parameters. The numbering of the atoms refers to the labelling shown in Fig.5.5. All the hyperfine coupling values are given in MHz.

Considering a distorted tetrahedral symmetry, assuming pure atomic d orbitals within crystal field theory, the spin Hamiltonian parameters for a d_{z^2}ground state are given by Eq. 4.1 and lead to $g_{\parallel} > g_{\perp}$. The work from Greenblatt et al.[7] suggested that the covalency must be considered for d_{z^2} ground state, as the distortion will be unambiguously compressional when the ligand covalent effects are predominant. This is also pointed out from the significant spin density delocalization over the oxygens predicted by the DFT computation.[1] To reconcile the deviation of the g_z from the g_e and the large rhombicity of the experimental resolved spin Hamiltonian parameters, assumptions similar to the discussion made for Cr^{5+} on silica (Sec. 4.1) can be taken into account. The admixture of the $d_{x^2-y^2}$ state into the d_{z^2} ground state provided the departure of the g_z from g_e, and, in addition to the case of Cr^{5+} on silica, the resolved large rhombicity.[7–10]

5.1.2 Local Environment of the Pentavalent Cr

To investigate the surrounding environment of Cr^{5+}, Q-band HYSCORE experiments were performed at the field position (B_0=1124.1 mT) corresponding to the maximum signal intensity in the EDFS spectrum (Fig.5.3b). The standard 4-pulse HYSCORE gave poor signal intensity (Fig.5.4a). Presumably it is the effect of weakly modulating nuclei in the case of Q-band measurement of *hfi* with small anisotropic component, which is characterized by the signals lying on the anti-diagonal line centered at the Larmor frequency. On top of this, the sample gave a weak echo intensity signal due to small Cr concentration. To solve this problem, 6-pulse HYSCORE was conducted as proposed by Kasumaj and Stoll[11] to give modulation enhancement up to 8-fold for weakly modulated nuclei compared to the 4-pulse HYSCORE. It can be clearly seen that in the 6-pulse HYSCORE spectrum (Fig.5.4b) the signal intensities were greatly enhanced.

The spectrum shows three series of cross peaks (red arrows in Fig.5.4b) centered symmetrically around $\nu_{\mathrm{Al}} = 13.59$ MHz, which can be attributed to groups of ^{27}Al characterized by distinct *hfi*, in particular, relatively large isotropic *hfi* parameters a_{iso} and small dipolar couplings. In addition to the ^{27}Al signals, a peak (blue arrow in Fig.5.4b) centered at ^{31}P Larmor frequency ($\nu_P = 21.12$ MHz) is observed and attributed to remote ^{31}P lattice nuclei. The presence of ^{27}Al with larger a_{iso} and remote ^{31}P nuclei indicates the Cr^{5+} is situated in an ^{27}Al-rich environment without ^{31}P in the vicinity of its surrounding. This is an evidence of the framework P^{5+} substitution by Cr^{5+} which has only ^{27}Al in the second coordination sphere. DFT models were built based on this hypothesis assuming three different situations for the Si distributions. (Fig.5.5) The three models all consist of a Cr^{5+} per unit cell substituting a P^{5+} framework site with two Si^{4+} replacing a pair of framework Al^{3+} and P^{5+}. They differ by how the Si pairs are situated with respect to the Cr^{5+} site. In the first case, the two Si ions are next to each other and to the Cr^{5+}, this case is referred to as: "Near-Si pair". The second case occurs when the two Si ions are next to each other and far from the Cr^{5+}, this is the so-called "Far-Si pair". And in the third case, the two Si ions are separated leaving one Si next to the Cr^{5+} and the other one far from it, the "Split-Si pair". The *hfi* parameters were computed (Tab. 5.1) with these models and worked as a starting point for the HYSCORE computer simulations.

Computer simulation (Fig.5.4c) was done by summing up a series of ^{27}Al species with a_{iso} distributed within three ranges, namely: ^{27}Al(1) with a_{iso} = 0-2 MHz, ^{27}Al(2) with a_{iso} = 4-9 MHz, and ^{27}Al(3) with a_{iso} = 13-17MHz. (Tab. 5.1) Such a dispersion of isotropic hyperfine coupling constants, i.e., "a-strain", has been observed previously on both solid state[12, 13] and

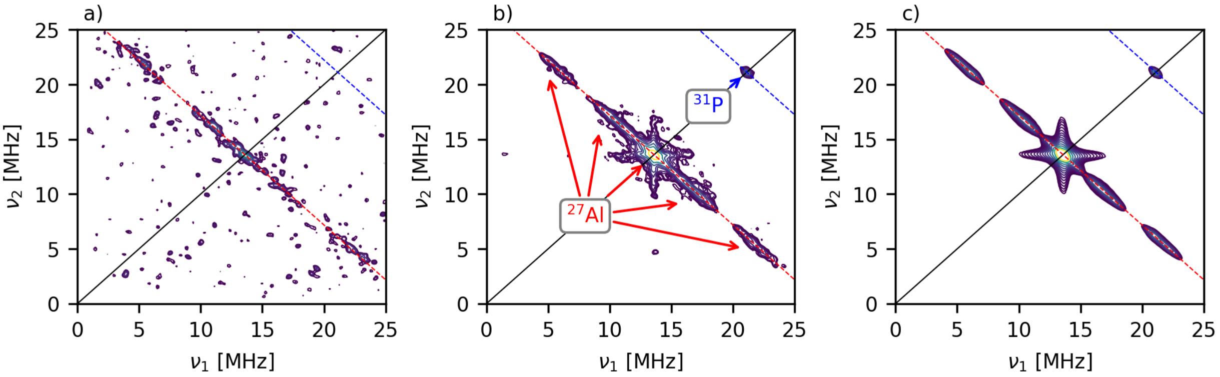

Figure 5.4: The Q-band a) standard 4-pulse HYSCORE spectrum superimposed with interpulse delays (τ = 110, 116, 146 ns), b) 6-pulse HYSCORE spectrum superimposed with interpulse delays (τ = 110, 146 ns), and simulated HYSCORE spectrum superimposed with interpulse delays (τ = 110, 146 ns) of the Cr-SAPO-5 measured at T = 40 K and field position marked in Fig.5.3b. The red dashed lines mark the Larmor frequency of ^{27}Al ($\nu_{\mathrm{Al}} = 13.59$ MHz) and the blue dashed lines mark the Larmor frequency of ^{31}P ($\nu_{\mathrm{P}} = 21.12$ MHz). In the simulation, three groups of ^{27}Al and a ^{31}P were considered with the *hfi* tensors given in Tab. 5.1.

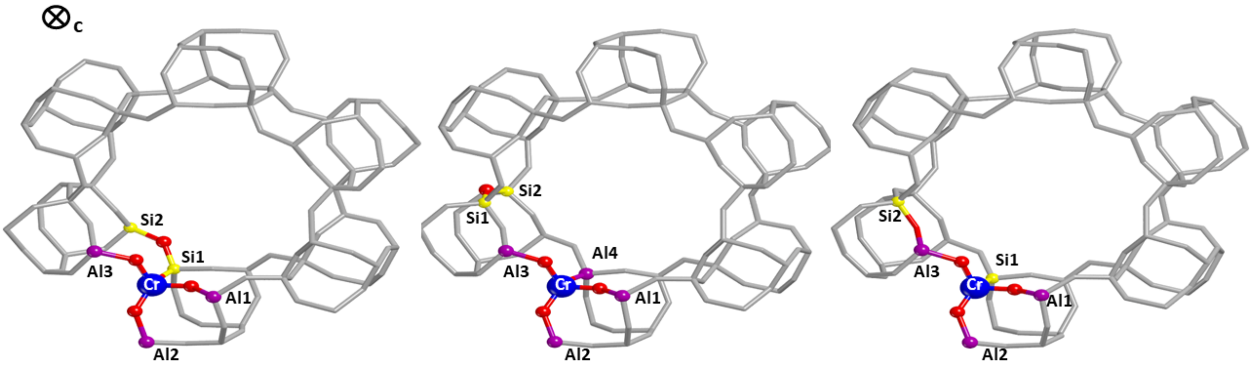

(a) Near-Si pair model **(b) Far-Si pair model** **(c) Split-Si pair model**

Figure 5.5: Fully optimized structure of Cr-SAPO-5 periodic models at B3LYP-D3(ABC)/pob-TZVP-rev2 level of theory: in a) the Near-Si pair, b) Far-Si pair and c) Split-Si pair models. The c-axis of the unit cell points towards the page.

molecular systems[14, 15] and is due to the structural fluctuations of the ligand environment around the paramagnetic metal center. The isotropic hyperfine coupling reflects the spin density transfer from the paramagnetic center to the ^{27}Al in the second coordination sphere through the directly coordinated oxygens, which depends remarkably on the bond angle and distance of the M-O-Al linkage, and therefore, is particularly sensitive to the structural fluctuations. This is also supported by the DFT computations, that the different ^{27}Al in the second coordination sphere in the different models show slightly different a_{iso} that fall in the range of the simulation. Meanwhile, a maximum of 1.4 ± 0.2 MHz of the dipolar coupling (T) is obtained from the simulations. Above this value, the simulation shows additional peaks associated to multi-quantum transitions which are not present in the experimental spectrum.

Considering the value of a_0=3367.76 MHz for unit spin density on the ^{27}Al 3s orbital,[16] the corresponding spin density transfer to the Al 3s orbital is in the range of 0.06-0.5 %, in good agreement with other d^1 transition metal ions involving M(3d^1)–O–Al linkages.[12, 13] In addition, the cross peak centered at the Larmor frequency of ^{31}P with extension of approximately 2 MHz indicates the electron spin that is localized on Cr^{5+} interacts with distant phosphorus nuclei. Using the point-dipole approximation

$$T = \frac{\mu_0}{4\pi} g_e g_n \beta_e \beta_n \frac{1}{r^3} \tag{5.1}$$

and the dipolar hyperfine coupling obtained from simulation (Tab. 5.1), a lower limit of the Cr-P distance r of 0.4 nm can be derived. This is in agreement with the DFT models and suggesting the P nuclei locating in the 4th coordination sphere of the Cr^{5+} ion. All in all, the HYSCORE spectrum with the DFT computation provides unambiguous evidence that the chromium ions were successfully incorporated at the framework P^{5+} sites of SAPO-5.

5.2 Bi-Metallic Mo/V-SAPO-5

In this section, I present the work on the method of preparing the bi-metallic Mo/V-SAPO-5 catalyst with the evidence provided by EPR spectroscopy. The local environment of the mono-metallic V-SAPO-5 was first investigated and compared to that of the bi-metallic system with molybdenum in addition.

5.2.1 Local Environment of V-SAPO-5

After contacting the dehydrated SAPO-5 sample with the vapor of VCl$_4$ the characteristic eight-fold hyperfine splitting of all anisotropic components of the typical V^{4+} (^{51}V, I = 7/2, 99.76 % abundance) is observed in the X-and Q-band CW-EPR spectra. (Fig.5.6) The well resolved ^{51}V hyperfine patter and the absence of broad absorption features suggests the the V^{4+} species were highly dispersed in the material without clustered or polymeric V^{4+} units. Computer simulations were done including the electron Zeeman interaction and hyperfine interaction. With slightly rhombic g and A tensors, as reported in Tab. 5.2, the spectra at both frequencies show good agreement between the experimental and simulated spectra. These values coincide with the typical values of the reported VO^{2+} species[12, 17] suggesting the formation of the V^{4+}–O^{2-} species with shorter V–O bond corresponds to the typical characteristics of a vanadyl species, resulting from the reaction of VCl$_4$ with SAPO-5. A similar situation has been reported in the case of VCl$_4$ reacting with ZSM-5 zeolites.[17]

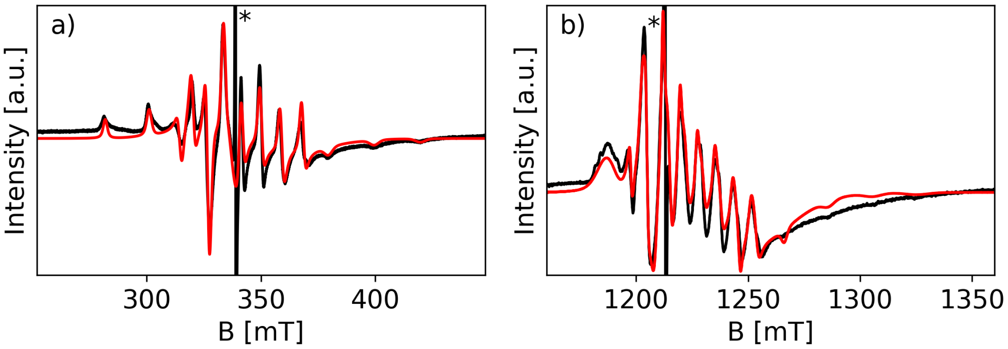

Figure 5.6: Experimental (black) and simulated (red) CW-EPR spectra of V-SAPO-5 recorded at a) X-band and b) Q-band. The spectra were recorded at room temperature (RT). The asterisks mark the signals of residual coke radical in SAPO-5 after calcination.

	g_x	g_y	g_z	$\|A_x\|$	$\|A_y\|$	$\|A_z\|$	$g_\perp$	$g_\parallel$	$\|A_\perp\|$	$\|A_\parallel\|$	Ref.
	V^{4+}						Mo^{5+}				
V-SAPO-5	1.9833 ±0.001	1.9785 ±0.001	1.9330 ±0.001	213 ±5	208 ±5	533 ±3					This Work
VAPO-5	1.978	1.9734	1.9358	209	183	534					[12]
	1.978	1.9643	1.9375	207	178	515					
VCl_4-ZSM-5	1.9843	1.9843	1.931	214	214	542					[17]
Mo/V-SAPO-5	1.9840 ±0.001	1.9785 ±0.001	1.9335 ±0.001	210 ±5	195 ±5	520 ±5	1.9575 ±0.002	1.9310 ±0.003	100 ±20	180 ±30	This Work
Mo-ZSM-5							1.945	1.878	190	-	[18]
Mo-SAPO-5							1.952	1.877	-	-	[19]

Table 5.2: Spin Hamiltonian parameters of Mo/V-SAPO-5 derived from the simulations of the CW-EPR spectra and comparison to reported similar systems. The units for hyperfine coupling parameters are in MHz.

		a_{iso}	T	α, β, γ		a_{iso}	T	δ	α, β, γ		a_{iso}	T	δ	α, β, γ	Ref.
		^{27}Al				^{31}P					^{95}Mo				
Mo/V-SAPO-5	$^{27}Al_1$	3-9	1-2	0,0,0	$^{31}P_1$	3-5	0.5-1	0	0,0,0	$^{95}Mo_1$	-3.0 ±0.5	-1.3 ±0.3	-0.5 ±0.3	0, 90 ±20, 0	This Work
	$^{27}Al_2$	13-15	1-2	0,0,0	$^{31}P_2$	9-15	1-1.5	0	0,0,0						
					$^{31}P_3$	18-21	0.5-1	0	0,0,0						
VAPO-5		4.5	2.5	0,90,0		18	3.5	0.5	0,80,0						[12]
		2	1	0,90,0		6.7	2.15	0.5	80,80,0						
						2	0.8	0	0,80,0						
											^{51}V				
VCl_4-TiO_2-101											6	0.5		0,60,0	[20]
VCl_4-TiO_2-001											7.17	3.46		0,70,0	

Table 5.3: Hyperfine coupling parameters of Mo/V-SAPO-5 derived from the simulations of the HYSCORE spectra and comparison to reported similar systems. The units of the hyperfine coupling parameters are in MHz and degrees for the Euler angles.

The local environment of the V^{4+} species can be examined by means of hyperfine spectroscopy, depicting the hyperfine interaction of the V^{4+} species with the surrounding paramagnetic nuclei. In the case of SAPO, these are the framework ^{27}Al ($I = 5/2$, 100 % abundance) and ^{31}P ($I = 1/2$, 100 % abundance). Due to low natural abundance (4.68 %), it is unlikely that ^{29}Si ($I = 1/2$) can give sensible information. The Q-band HYSCORE spectra measured at $B_0 = 1204$ and 1244 mT with increment $\Delta t = 16$ ns for t_1 and t_2 are reported in Fig.5.7. The spectra showed cross-peaks lying symmetrically along the anti-diagonals centered at the Larmor frequencies of ^{27}Al separated by 18 MHz and are almost identical for both field positions. This indicates the hyperfine coupling of the V^{4+} species with the Al is dominated by the isotropic component as reported in similar systems.[12] Whereas the cross-peaks lying along the anti-diagonals centered at the Larmor frequencies of ^{31}P extend until 32 MHz and are clipped at the upper limit of the frequencies. This shows that the increment Δt for t_1 and t_2 is not short enough to cover the higher frequency following the Nyquist criterion[21]

$$\Delta t = \frac{1}{2\nu_{max}}. \tag{5.2}$$

In order to decrease Δt, the number of points for the measurement needs to be increased making sure the resolution of the spectrum remain the same. This means the time required for recording one spectrum will also increase. For this reason, the Remote-HYSCORE method was adopted with shortest possible τ avoiding the need of recording and superimposing spectra with many different τ for eliminating the blind-spot effect.[22] The Remote-HYSCORE spectrum (Fig.5.8b,c) resolves the full spectrum without blind-spot or clipping, though with lower sensitivity due to the delay between the standard HYSCORE sequence and the storage/detection sequence.

The cross-peaks centered at the ^{27}Al Larmor frequency can be fitted by computer simulation with two groups of Al species characterized by the a_{iso} distributing in the range of 3-9 MHz and 13-15 MHz. (Tab. 5.3) Similar to the case of Cr-SAPO-5 discussed in the previous section, the distribution of a_{iso} results from the structural fluctuation of the ligand environment around the paramagnetic center.[1, 12–15] However, in contrast to the case of Cr-SAPO-5 that is related to the incorporated framework sites, it can be associated to the different extra-framework sites at which the V^{4+} is grafted on the surface of SAPO-5. The two groups indicate the vanadyl species interact with at least two different kind of Al species. Considering the value of $a_0 = 3367.76$ MHz for unit spin density localizing on the ^{27}Al 3s orbital,[16] the corresponding spin density transfer from V^{4+} to the two Al species can be estimated in the order of 0.17 % and 0.42 %. This indicates the presence of V–O–Al linkages and is similar to the reported case of extra-framework VO^{2+} species in the VAPO-5 system and the $Al_2O_3/TiCl_x$ catalyst.[12, 13]

In addition to the ^{27}Al couplings, the cross-peaks centered at the ^{31}P Larmor frequency can be simulated with three groups of P species characterized by a_{iso} distributing in the range of 3-5, 7-10, and 12-15 MHz. (Tab. 5.3) These values are similar to the ones reported in the case of VAPO-5.[12] And the a_{iso} distribution due to the structural fluctuation also applies here. The same analysis for the spin density transfer is considered for $a_0 = 10201.44$ MHz with the unit spin density on the ^{31}P 3s orbital. The spin density delocalizations of the order 0.04 %, 0.11 %, and 0.19 % are estimated for the three groups of P nuclei. The spin density transfers to the Al and P in the second coordination sphere in the same order of magnitude and differs mainly by the bond length and angle of the V–O–L linkages where L being either Al or P. The simultaneous presence of ^{27}Al and ^{31}P

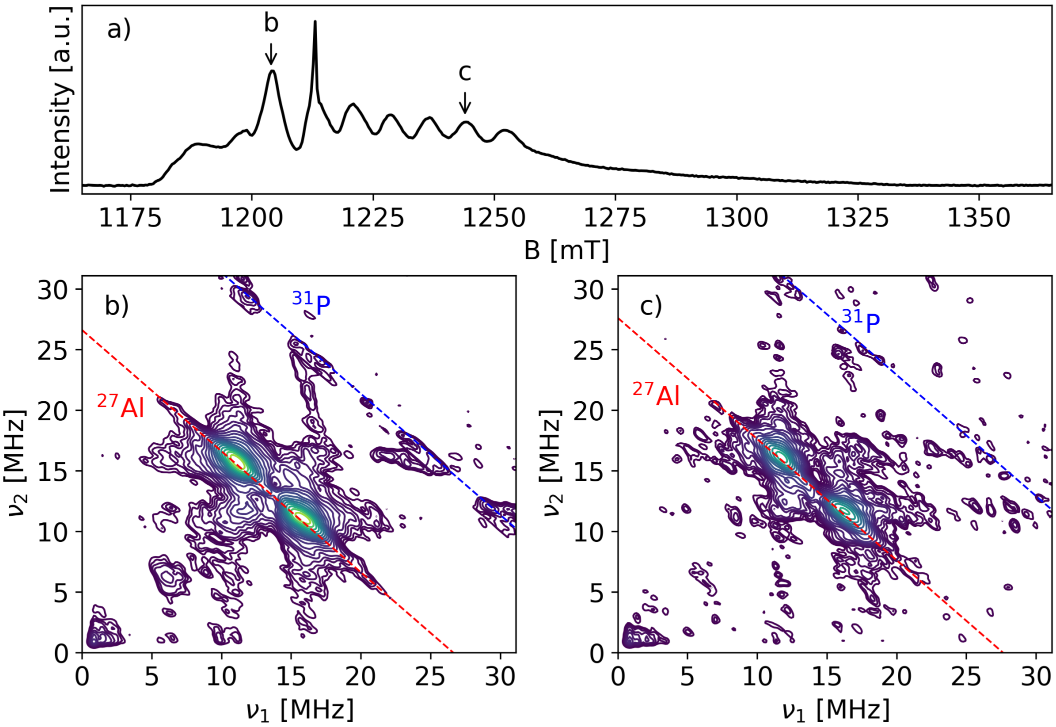

Figure 5.7: The Q-band V-SAPO-5 a) EDFS spectrum and b,c) HYSCORE spectra measured at field positions indicated in the EDFS spectrum. The HYSCORE spectrum measured at b) 1204 mT is superimposed with interpulse delay $\tau = 148$, 218 ns and the spectrum measured at c) 1244 mT is superimposed with interpulse delay $\tau = 152$, 224 ns. Experiments were conducted at T = 30K. The Larmor frequencies of ^{27}Al are marked with red dashed lines and that of ^{31}P are marked with blue dashed lines.

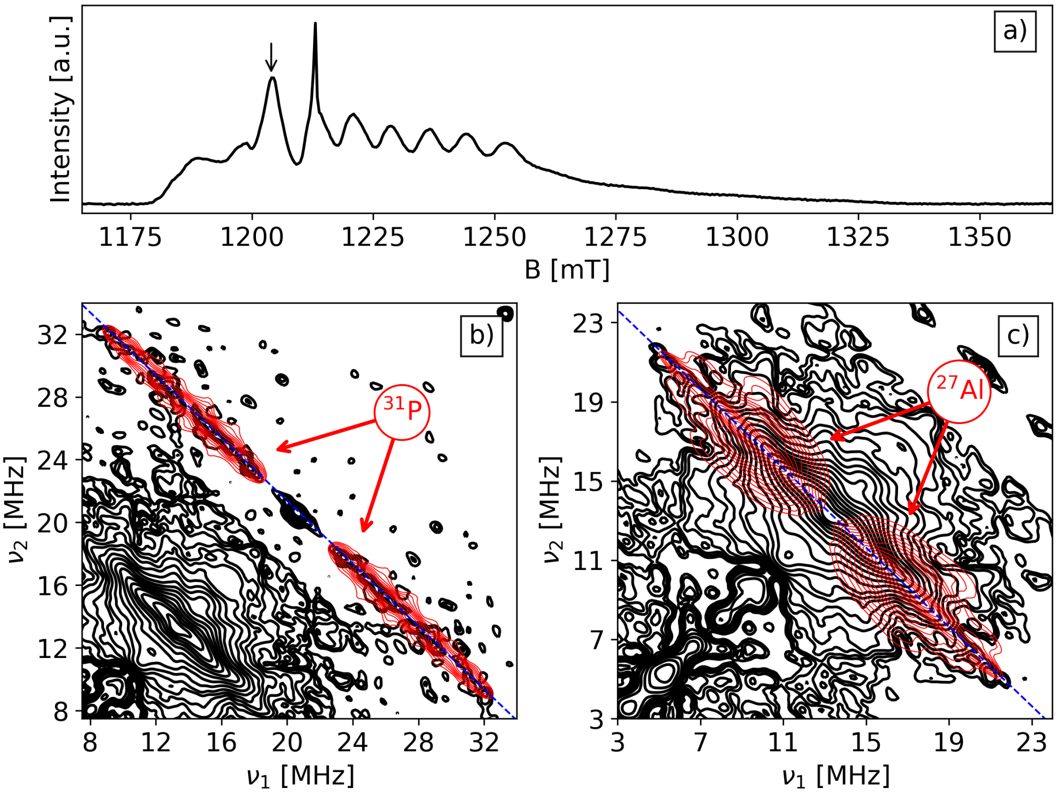

Figure 5.8: The Q-band V-SAPO-5 a) EDFS spectrum and Remote-HYSCORE spectrum with $\tau = 24$ ns at $B_0 = 1204$ mT with simulations in red for b) ^{31}P and c) ^{27}Al. The spectra were measured at T = 30 K. Larmor frequency of each nucleus is marked with blue dashed lines.

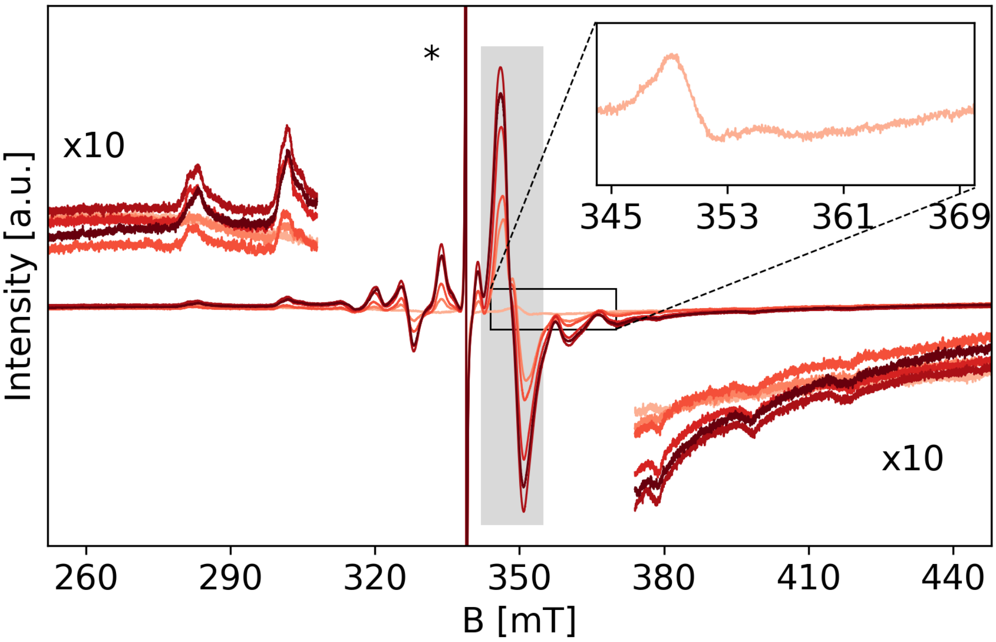

Figure 5.9: The CW X-band EPR spectra of VCl_4 deposited at increasing doses on Mo-SAPO-5. All the spectra were measured at RT. The inset shows the residual Mo^{5+} signal in the sample after the oxidation of the Mo and the shaded area marks the Mo^{5+} signal that appears after the doses of VCl_4. The asterisk marks the signal of the residual coke radical in SAPO-5 after calcination.

couplings with the similar order of spin density delocalization indicates that the vanadyl species are anchored at the extra-framework sites on the surface of SAPO-5. This is clearly different from the case of the V^{4+} incorporated at framework sites in VAPO-5 or TiAPO-5 where only the hyperfine couplings of P were detected.[12, 23] The alternating phosphate and aluminate tetrahedra units in the (S)APO materials combining the hyperfine spectroscopy allows clear distinction between framework and extra-framework incorporation of the transition metal ions.

5.2.2 Local Environment of Mo/V-SAPO-5

Similar experiments were performed on the bi-metallic Mo/V-SAPO-5. The Mo-grafting procedure was reported by Abdo and Howe[24] that the activated SAPO-5 was contacted with $Mo(CO)_6$ vapor then heated at 473 K under dynamic vacuum. After another oxidation with oxygen at 573 K, the CW-EPR spectrum shows a weak signal occured at 345-365 mT. (Fig.5.9) This can be attributed to the residual Mo^{5+} characterized by an axial pattern with $g_\perp = 1.940$ and $g_\parallel = 1.876$, the typical Mo^{5+} signal with oxygen-containing ligands,[19, 25] while the dominant Mo species were oxidized to Mo^{6+}. The EPR signal is unstable over time, suggesting the formation of diamagnetic species, possibly amenable to MoO_3 and $Al_2(MoO_3)_4$ crystallites as reported in the case of ZSM-5 zeolites.[26]

Enhanced redox properties of bi-metallic catalysts originate from the synergistic effects related to the existence of electronic interactions at short range. To investigate the possibility to establish short-range electronic interactions, VCl_4 was evaporated on the Mo-SAPO-5 catalyst. In the Fig.5.9, the X-band CW-EPR spectra are reported as a function of the VCl_4 doses. As the amount

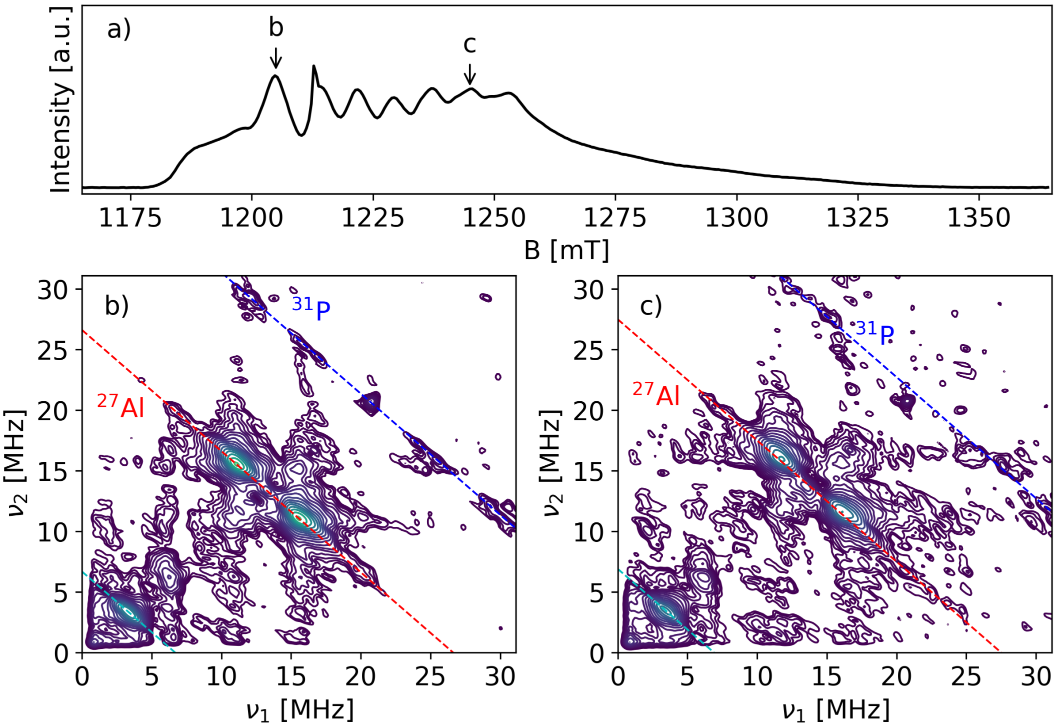

Figure 5.10: The Q-band Mo/V-SAPO-5 a) EDFS spectrum and b,c) HYSCORE spectra measured at field positions indicated in the EDFS spectrum. The HYSCORE spectrum measured at b) 1205 mT is superimposed with interpulse delay τ = 148, 218 ns and the spectrum measured at c) 1245 mT is superimposed with interpulse delay τ = 152, 224 ns. Experiments were conducted at T = 30K. The Larmor frequencies are marked for ^{27}Al with red dashed lines, ^{31}P with blue dashed lines, and ^{95}Mo with cyan dashed lines.

of VCl_4 increases, the spectral feature of V^{4+} similar to that occured in the V-SAPO-5 system (Fig.5.6) increases alongside with the emergence of the Mo^{5+} EPR signal. The latter signal suggests a single electron transfer reaction from V^{4+} leading to the reduction of Mo^{6+} species, $Mo^{6+} + V^{4+} \longrightarrow Mo^{5+} + V^{5+}$. And the emergence of the former signal of VO^{2+} is originated from the deposition of the species without grafted Mo^{6+} in close proximity.

To validate the presence of the V–O–Mo linkage, standard-HYSCORE experiments were performed at the same condition as for the V-SAPO-5 sample. However, the Mo^{5+} signal was not observed in the EDFS spectrum (Fig.5.10a) assuming a redox reaction, $Mo^{5+} + V^{5+} \longrightarrow Mo^{6+} + V^{4+}$, took place with unclear reason. The spectra (Fig.5.10b,c) show complex sets of cross-peaks. Two sets in each spectrum are related to ^{27}Al and ^{31}P couplings which are analogous to those discussed in the previous section and are related to the interaction of V with the nearby Al and P. At lower frequencies, the ridges with maximum extension of approximately 5.2 MHz appear on the diagonal at the frequency corresponds to the Mo Larmor frequency. As the spectrum measured at 1205 mT (Fig.5.10b) shows better signals and the other spectrum do not show much difference, the discussion will be focused on it later on. Mo has two paramagnetic isotopes (I = 5/2 for both), ^{95}Mo and ^{97}Mo, with 15.92 % and 9.55 % abundance and similar nuclear g factors (Tab. 2.1), leading to Larmor frequencies of 3.36 and 3.43 MHz. The ridge with maximum extension of about 5.2 MHz and centered at 3.4 MHz in the experimental spectrum is assigned to transitions between the $m_I = \pm 1/2$

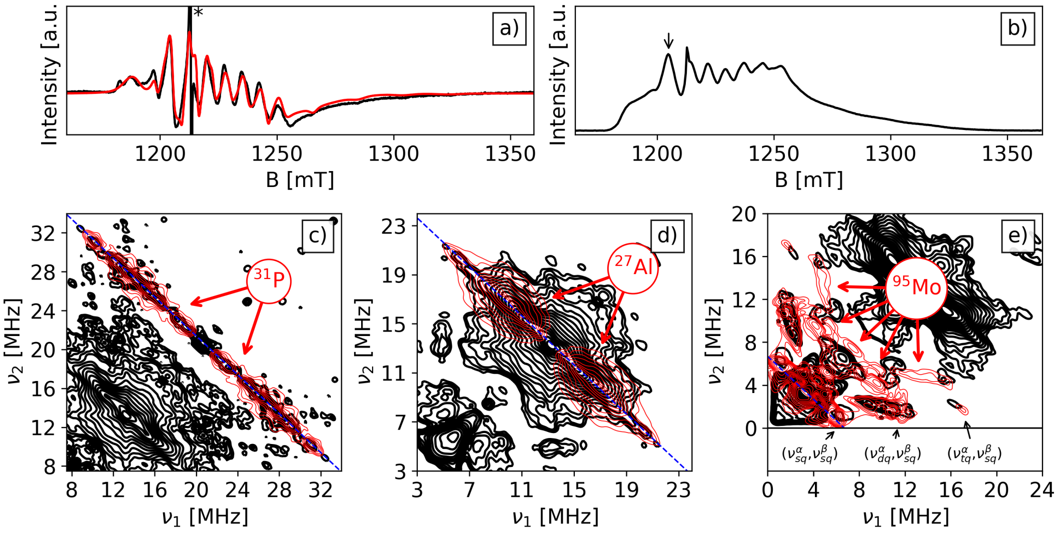

Figure 5.11: The Q-band Mo/V-SAPO-5 a) CW-EPR experimental (black) and simulated (red) spectrum, b) EDFS spectrum, Remote-HYSCORE spectrum with τ = 24 ns at B_0 = 1205 mT with simulations in red for c) ^{31}P and d) ^{27}Al, and the standard-HYSCORE spectrum with τ = 148 ns with simulation in red for ^{95}Mo. The spectra were measured at T = 30 K. Larmor frequency of each nucleus is marked with blue dashed lines.

states which are not affected (to first order) by nuclear quadrupole interaction. In addition to this ridge, the correlation peaks with $|\Delta m_I| = 2$ and $|\Delta m_I| = 3$ transitions are also observed at (10.58, 1.28) and (15.38, 1.28) MHz. The presence of these peaks and the extension of the ridge centered at the Mo Larmor frequency provides evidence of non-negligible spin density transfer from V^{4+} to the nearby Mo.[20]

The same Remote-HYSCORE experiment (Fig.5.11c,d) was conducted for analyzing the ^{27}Al and ^{31}P couplings. (Tab. 5.3) Similar to the case of V-SAPO-5, the results indicate similar spin density transfer over the V–O–L linkages for L = Al and P. Based on this evidence and assuming the same situation holds for V–O–Mo linkages, the spin density delocalization on Mo is assumed at the order of 0.1 % and used as the starting point in the computer simulation of the Mo nuclear transitions.[27] A simulation analysis was then performed, and the best result (Fig.5.11e) shows a convincing simulation of the Mo spectral feature with the hyperfine tensor $A = [-1.2, -2.2, -5.6]$ MHz. (Tab. 5.3) Similar bi-metallic linkages have been reported for vanadium species at the surface of TiO_2 involving the mixed valence V^{4+}–O–V^{5+} units, reminiscent of molecular $V_2O_3^{3+}$ species.[20]

5.3 NO-Adsorbed SAPO-5

In this section, I present the results related to the adsorption of NO on SAPO-5. Due to it's radical nature, NO molecules are widely used as a paramagnetic surface probe in microporous materials.[28–33] Here, I activated SAPO-5 under different conditions and admitted NO in order to investigate the interaction between the adsorption sites and the NO molecules by means of CW-and pulse EPR. Three samples will be considered, characterized by different activation and reaction conditions as referred named as **L20** (activated at lower temperature and dosed with 20 μmol NO), **H20** (activated at higher temperature and dosed with 20 μmol NO), and **H10** (activated at higher

	Activation Temperature [K]	NO amount [μmol]
SAPO5_NO_L_20 (L20)	473	~20
SAPO5_NO_H_20 (H20)	623	~20
SAPO5_NO_H_10 (H10)	623	~10

Table 5.4: The name of the samples for the NO-adsorbed SAPO-5 and their corresponding experimental condition.

temperature and dosed with 10 μmol NO). The detailed activation conditions are listed in Tab. 5.4.

5.3.1 Distinguishing NO Adsorption Sites

The CW-EPR spectra measured at T = 10 K are reported in Fig.5.12. In the spectrum of **L20**, signals can be attributed to surface NO species characterized by an axial feature where the $g_\perp$ centered at $B_0 \sim 343$ mT and $g_{||}$ at 376 mT.[28, 30, 34] Whereas the spectra of **H20** and **H10** shows similar features at the $g_\perp$ position while the the features for $g_{||}$ appear to be indefinite. The equation for the g-values for NO is written in second order perturbation theory as[35]

$$\begin{cases} g_{xx} = g_e \dfrac{\Delta}{\sqrt{\lambda^2+\Delta^2}} - \frac{\lambda}{E}\left(\dfrac{\Delta-\lambda}{\sqrt{\lambda^2+\Delta^2}} - 1\right) \\ g_{yy} = g_e \dfrac{\Delta}{\sqrt{\lambda^2+\Delta^2}} - \frac{\lambda}{E}\left(\dfrac{\Delta+\lambda}{\sqrt{\lambda^2+\Delta^2}} + 1\right) \\ g_{zz} = g_e - \dfrac{2l\lambda}{\sqrt{\lambda^2+\Delta^2}} \end{cases} \tag{5.3}$$

in which λ is the spin-orbit coupling constant, Δ is the energy level splitting between ${}^2\Pi_y^\star$ and ${}^2\Pi_x^\star$ state due to orthorhombic distortion caused by local electric field gradient (Fig.5.12), E is the energy level splitting between the ${}^2\Pi_y^\star$ ground state and ${}^2\Sigma^\star$ state, and l is the effective g-factor for the orbital contribution which is often found to be close to unity.[35–38] It can be seen in Eq. 5.3, that the $g_{||}/g_{zz}$ is dependent to the orthorhombic distortion, i.e. the local electric field gradient. The change of $g_{||}$ indicates the NO species are adsorbed at different sites. Meanwhile, the splitting at the $g_\perp$ position (marked as A_{yy} in Fig.5.12) is correlated to the spin density distribution on the $2s$ and $2p\pi$ orbitals of ^{14}N.[30, 39]

Computer simulations are rather difficult in these cases. The signals from NO are overlapping with that from the residual radical in SAPO-5 and broad features that can be attributed to weakly adsorbed NO species.[35, 40] The weakly adsorbed NO species are assumed to distribute over various adsorption sites and therefore experience different electric field gradient resulting in large distribution of the g-tensors. This is shown in particular for g_{zz} in **H20** and **H10** (Fig.5.12b,c) and leaves large uncertainty and distribution ranges for it. Nevertheless, the spin Hamiltonian parameters obtained from simulations are reported in Tab. 5.5 and compared to some reported physisorbed NO.[28, 30, 34] The axial symmetry of the g-tensors might be due to large energy difference from Π^* to Σ^*, E, which leads to small $\frac{\lambda}{E}$ (Eq. 5.3) resulting in small rhombicity and therefore unresolved in the spectra.[35] The comparison of the g-tensor between **L20** and the reported NO species indicates the NO species experience smaller electric field gradient. This might be due to the lack of cations as adsorption sites on the surfaces of SAPO-5. Considering the differences between the cases of γ-alumina and γ-alumina + water reported by Lunsford,[34] it might be also due to the residual

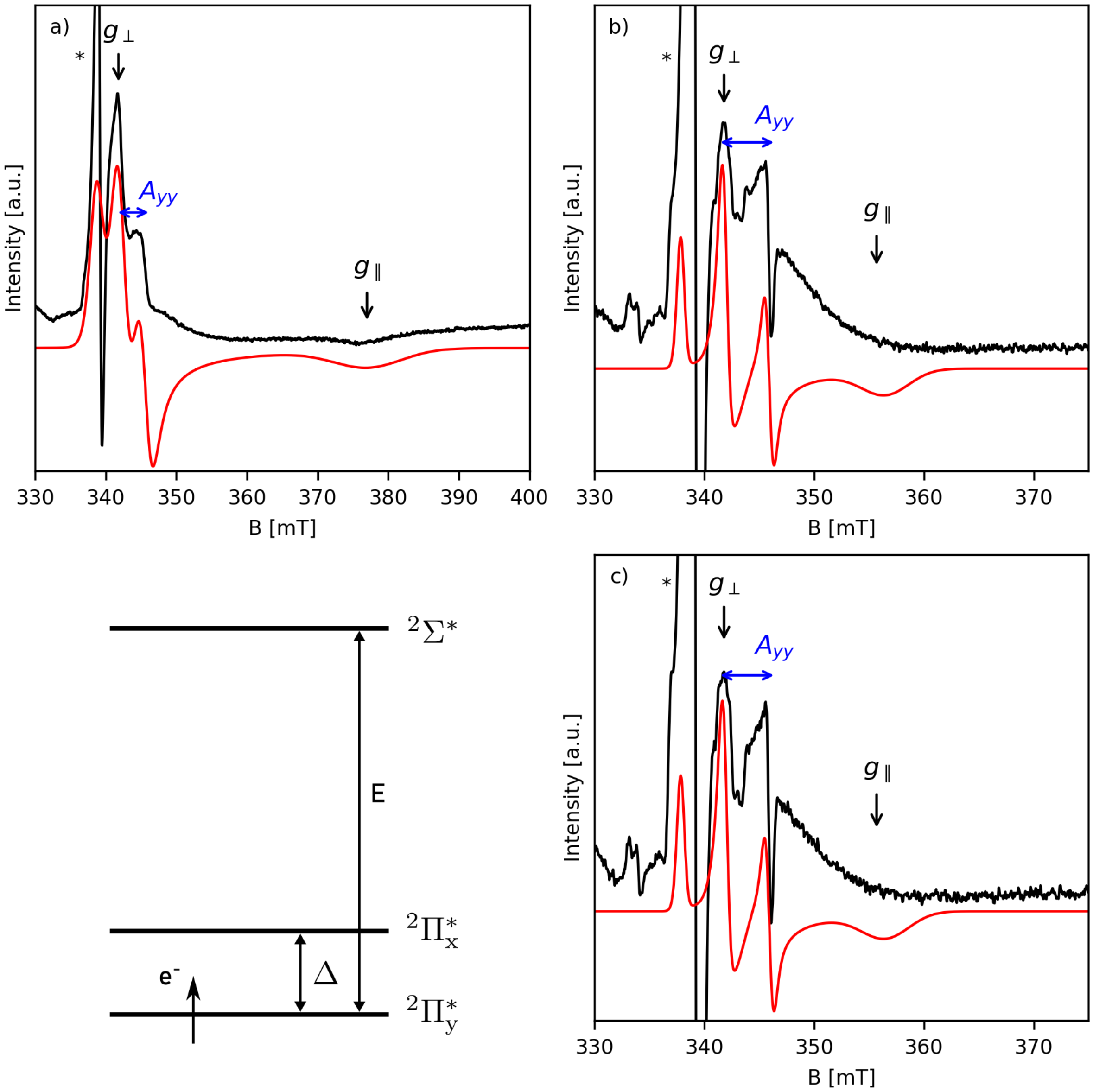

Figure 5.12: The X-band CW-EPR spectra of a) **L20**, b) **H20**, and c) **H10** measured at T = 10 K. At bottom left shows the diagram of the energy levels of the orbitals of NO. Asterisks mark the radical occurs in SAPO-5 after calcination.

	g_x	g_y	$g_z/g_\parallel$	A_{yy}^{14N} [MHz]	Ref.
	$g_\perp$				
L20	1.982 ±0.002		1.800 ±0.005	98 ±5	This Work
H20 **H10**	1.985 ±0.002		1.904 ±0.03	110 ±5	
Na-Y	1.986	1.978	1.83	81	[28]
Na-A	2.001	1.996	1.888	91	[30]
γ-alumina	1.996		1.96	- 39 (A^{27Al})	[34]
γ-alumina + water	1.996		1.94	-	
H-ZSM-5	1.999		1.927	84	[41]

Table 5.5: The spin Hamiltonian parameters derived from CW-EPR of the physisorbed NO on SAPO-5 and the reported NO species adsorbed on different surfaces.

water remaining in the pores of SAPO-5 shielding the electric field. Similarly, the difference for **H20** and **H10** indicates that the NO species are adsorbed at different sites and that the water removal might be more effective at higher activation temperature. Both suggestions are provided with evidence in the HYSCORE experiments which will be discussed in the next section.

Lastly, the study on free NO molecules reported by Dousmanis[39] suggested that the electronic structure of NO being in the mixture between $:\dot{\mathrm{N}}-\ddot{\mathrm{O}}:$ and $:\ddot{\mathrm{N}}^{-}-\dot{\mathrm{O}}:^{+}$. Meanwhile, the study on physisorbed NO on NaA zeolite suggested that the contribution from the latter electronic structure is enhanced as compared to the free NO molecule with evidence that the spin density shift to the oxygen $2p\pi$ orbital from the analysis of the ^{14}N hyperfine tensor.[30] It is the result of the interaction of NO with the Lewis acid sites, the sodium cations, creating net negative charge at the nitrogen. Similar result was also reported for the $\mathrm{Al}^{27}-\mathrm{NO}$ complex in H-ZSM-5.[41] In the case of physisorbed NO in SAPO-5, the hyperfine coupling parameter A_{yy} of all three samples are provided with higher value by computer simulations. This might be a result of lacking the Lewis acid sites on the surface of SAPO-5, and therefore, indicating the spin density is distributed more in the ^{14}N $2p\pi$ orbital, as opposed to the case of NaA zeolite. However, such suggestion can only be verified with the fully resolved hyperfine tensor which is not available here.

5.3.2 Characterizing Adsorption Sites

The X-band ^{27}Al HYSCORE spectra measured at field positions corresponding to maximum electron spin echo intensities are reported in Fig.5.13. The spectrum of **L20** shows a cross-peak at the ^{27}Al Larmor frequency ($\nu_{Al} = 3.93$ MHz) with extension of about 0.5 MHz and a cross-peak at the ^{31}P Larmor frequency ($\nu_P = 6.11$ MHz) with extension of 2 MHz. Both signals are attributed to remote species indicating the NO molecules are adsorbed on the surface of SAPO-5 without any direct interaction with the T-atoms. Computer simulation provides a maximum of 2.5 MHz for the nuclear quadrupole coupling conastant e^2qQ/h of the Al species, consistent with the solid-state NMR experiments.(Fig.3.2) On the other hand, the spectrum of **H10** shows cross-peaks at similar positions with reduced signal intensities presumably due to the lower dosage of NO and the properties of

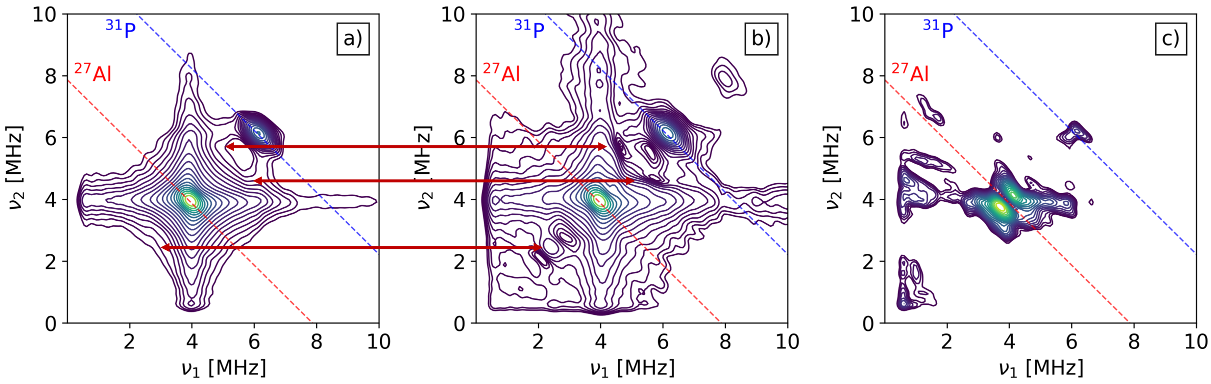

Figure 5.13: The X-band ^{27}Al HYSCORE spectra of a) **L20**, b) **H20**, and c) **H10**. All spectra were measure with τ = 100 ns at field positions correspond to $g_\perp$ and at T = 10 K. The diagonals centered at ^{27}Al Larmor frequency (ν_{Al} = 3.93 MHz) and ^{31}P Larmor frequency (ν_P = 6.11 MHz) are indicated with red and blue dashed lines.

different adsorption sites. The cross-peak at the ^{27}Al Larmor frequency is splitted symmetrically to the diagonal characteristic of large nuclear quadrupole interaction. With computer simulation, the Al e^2qQ/h is estimated with minimum of 4 MHz. Lastly, the spectrum of **H20** shows similar signals as **L20** with additional features at around (2.5, 2.5) and (4.5, 6) MHz. These features indicate the presence of two Al species, one that occurs in **L20** and the other from **H10**.

The differences between the three HYSCORE spectra can be explained by different adsorption sites. As the Al species in **H10** show distinctively large *nqi* which is not found in the literature, this might be due to NO molecules adsorbed at some defect sites with small quantity that are not observed previously. Whereas in **L20**, due to the lower activation temperature, some water molecules might still remain in the pores and block the defect sites, resulting the NO molecules being adsorbed in the vicinity of the dominant Al species. This is supported by the spectrum of **H20**, which is dosed with the doubled quantity of NO molecules, showing features of both Al with small and large *nqi* suggesting that the defect sites are saturated by part of the adsorbed NO and the remaining part are adsorbed near the major Al species.

The existence of residual water molecules was investigated by means of ^{1}H HYSCORE. The three ^{1}H HYSCORE spectra are reported in Fig.5.14. The spectrum of **L20** shows ridges centered around the ^{1}H Larmor frequency (ν_H = 15.16 MHz) extended by ~13 MHz with significant curvature characterized as *hfi* of proton species with large anisotropic component. Meanwhile, both spectra of **H20** and **H10** show ridges centered at the ^{1}H Larmor frequency with maximum of 4 and 2 MHz extension from *hfi* of remote proton. The presence of residual water molecules is then supported by the different spectral features observed between the cases of SAPO-5 activated at different temperatures. And the proton species in **L20** are assigned to water molecules in the vicinity of NO.

To analyze the ^{1}H HYSCORE spectrum of **L20**, the method developed by Dikanov et al.[42] for $S = 1/2$, $I = 1/2$ spin system was adopted. The one-to-one mapping of the nuclear frequencies $\nu_{\alpha(\beta)}$ and θ in the case of axial *hfi* is written in the form

$$\nu^2_{\alpha(\beta)} = (\nu^2_{\parallel\alpha(\beta)} - \nu^2_{\perp\alpha(\beta)}) \cdot \cos^2\theta + \nu^2_{\perp\alpha(\beta)} \tag{5.4}$$

with $\nu_{\parallel\alpha(\beta)} = |-\nu_I \pm (a_{iso} + 2T)/2|$ and $\nu_{\perp\alpha(\beta)} = |-\nu_I \pm (a_{iso} - T)/2|$. Considering the correlation

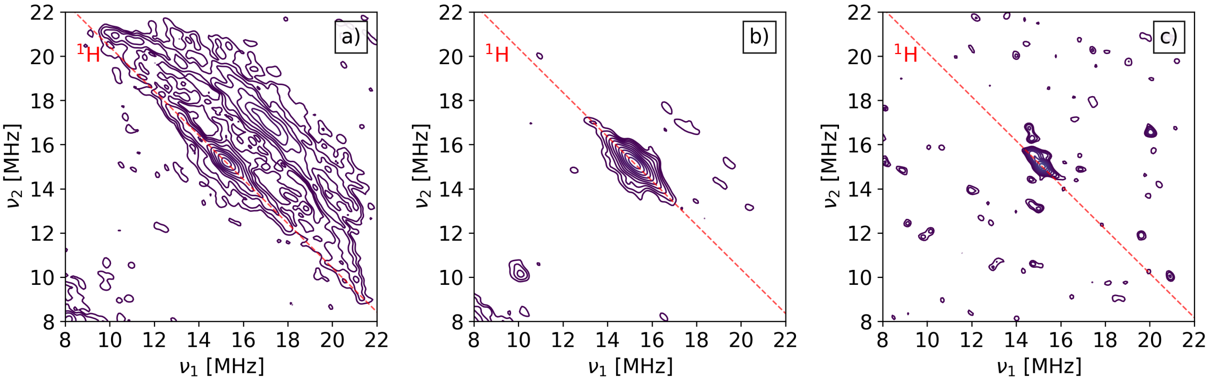

Figure 5.14: The X-band ^{1}H HYSCORE spectra of a) **L20** superimposed with τ = 100, 132, 254 ns, b) **H20** superimposed with τ = 100, 166 ns, and c) **H10** superimposed with τ = 100, 166, ns. All spectra were measure at field positions correspond to $g_\perp$ and at T = 10 K. The diagonals centered at ^{1}H Larmor frequency ν_H = 15.16 MHz are indicated with red dashed lines.

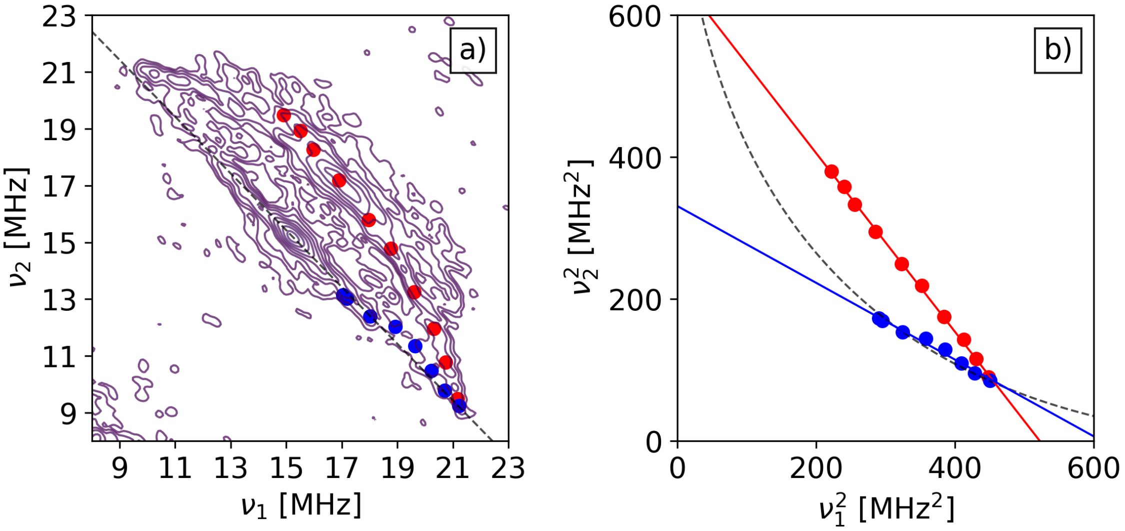

Figure 5.15: The application of the method for ^{1}H HYSCORE spectrum analysis developed by Dikanov et al.[42] by a) picking the data points from two of the three ridges of the proton cross-peaks from the X-band HYSCORE spectrum of **L20** at field position corresponding to $g_\perp$ and b) represents the data points in the (ν_1^2, ν_2^2) space with linear fit (red and blue solid lines) to the data points.

of nuclear frequencies in the two electron manifold, Eq. 5.4 can be rewritten with a unique mapping between ν_α and ν_β as

$$\nu^2_{\alpha(\beta)} = Q_{\alpha(\beta)}\nu^2_{\beta(\alpha)} + G_{\alpha(\beta)} \tag{5.5}$$

with

$$\begin{aligned} Q_{\alpha(\beta)} &= \frac{T + 2a_{iso} \mp 4\nu_I}{T + 2a_{iso} \pm 4\nu_I} \\ G_{\alpha(\beta)} &= \pm 2\nu_I \frac{4\nu_I^2 - a_{iso}^2 + 2T^2 - a_{iso}T}{T + 2a_{iso} \pm 4\nu_I} \end{aligned} \tag{5.6}$$

This leads to a linear equation for the nuclear frequencies in the $\nu^2_{\alpha(\beta)}$ coordinate with the slope $Q_{\alpha(\beta)}$ and the intercept $G_{\alpha(\beta)}$. And the hyperfine parameters a_{iso} and T can be worked out. For the case of rhombic *hfi*, the HYSCORE spectrum will show three ridges and by applying the method to each of the ridges, two of the three principal values of the hyperfine tensor can be obtained.[42, 43] Therefore, the full hyperfine tensor can be obtained so long as two ridges is resolved in the HYSCORE spectrum. The adaptation of this method to the **L20** ^{1}H HYSCORE spectrum is illustrated in Fig.5.15. The two ridges are picked from the red and blue points in Fig.5.15a and the plotted in the $\nu^2_{\alpha(\beta)}$ coordinate to run the least-square fitting to a linear equation (Fig.5.15b).

The hyperfine tensor obtained from the analysis method is used in the computer simulation with more refinement to the values and the Euler angles. To obtain the accurate Euler angles, the HYSCORE spectrum at the $g_\parallel$ position was also measured. The results are reported in Fig.5.16. The isotropic, axial, and rhombic components are obtained as $a_{iso} = 0.9\pm0.3$ MHz, $T = 9.5\pm0.5$ MHz and $\delta = 4\pm0.5$ MHz with Euler angles $\beta = 35\pm5°$ and $\gamma = 10\pm5°$. It is expected that the hyperfine tensor to be rhombic for such a large dipolar interaction resulting from small distance between the proton and NO at which the electron spin can no longer be treated as point-dipole.

The hyperfine tensor obtained from the experiment indicates a close distance from the proton to NO. The coordination of the water and NO molecules can be estimated by assuming that the spin density is distributed over the nitrogen and oxygen $2p\pi$ orbitals. Considering the hyperfine tensor for the dipolar component

$$\boldsymbol{T} = \sum_{K=N,O} \frac{\mu_0}{4\pi}\beta_e\beta_n g_e g_n \frac{\rho^K_{2p\pi}}{2}\left[\sum_{\mathbf{r}^\pm_{K-H}}\left(\frac{\mathbf{r}^\pm_{K-H}\otimes\mathbf{r}^\pm_{K-H}}{\|\mathbf{r}^\pm_{K-H}\|^5} - \frac{1}{\|\mathbf{r}^\pm_{K-H}\|^3}\right)\right] \tag{5.7}$$

with the spin density $\rho^K_{2p\pi}$ in the $2p\pi$ orbital for K = N, O and the electron-proton vector $\mathbf{r}^\pm_{K-H} = \mathbf{r}_{K-H} \pm \mathbf{R}^K_p$ for $\mathbf{r}_{K-H}$ the vector from the proton to N/O nucleus and $\mathbf{R}^K_p$ the vector from the N/O nucleus to the covalent radii[44] in one of the two lobes of $2p\pi$ orbitals. The scheme in Fig.5.17 shows the coordination structure assumed in the analysis of the system. The calculation is assumed for both the cases of the proton coordinates to nitrogen and to oxygen. And the proton is moved around the coordinated nucleus to probe the minimum difference between the calculated and experimental ^{1}H hyperfine tensors. The second proton is then moved around the first proton with the fixed distance to find the hyperfine tensor that reproduce the matrix proton signal in the HYSCORE spectrum. The calculation is run through different spin density distribution between the range of the free NO molecule ($\rho^N_{2p\pi} = 65\%$, $\rho^O_{2p\pi} = 35\%$) and the Na$^+$-NO complex[30] ($\rho^N_{2p\pi} = 46\%$, $\rho^O_{2p\pi} = 50\%$) to estimate the order of NO-water distance accordingly. The black lines in Fig.5.17a,b denote

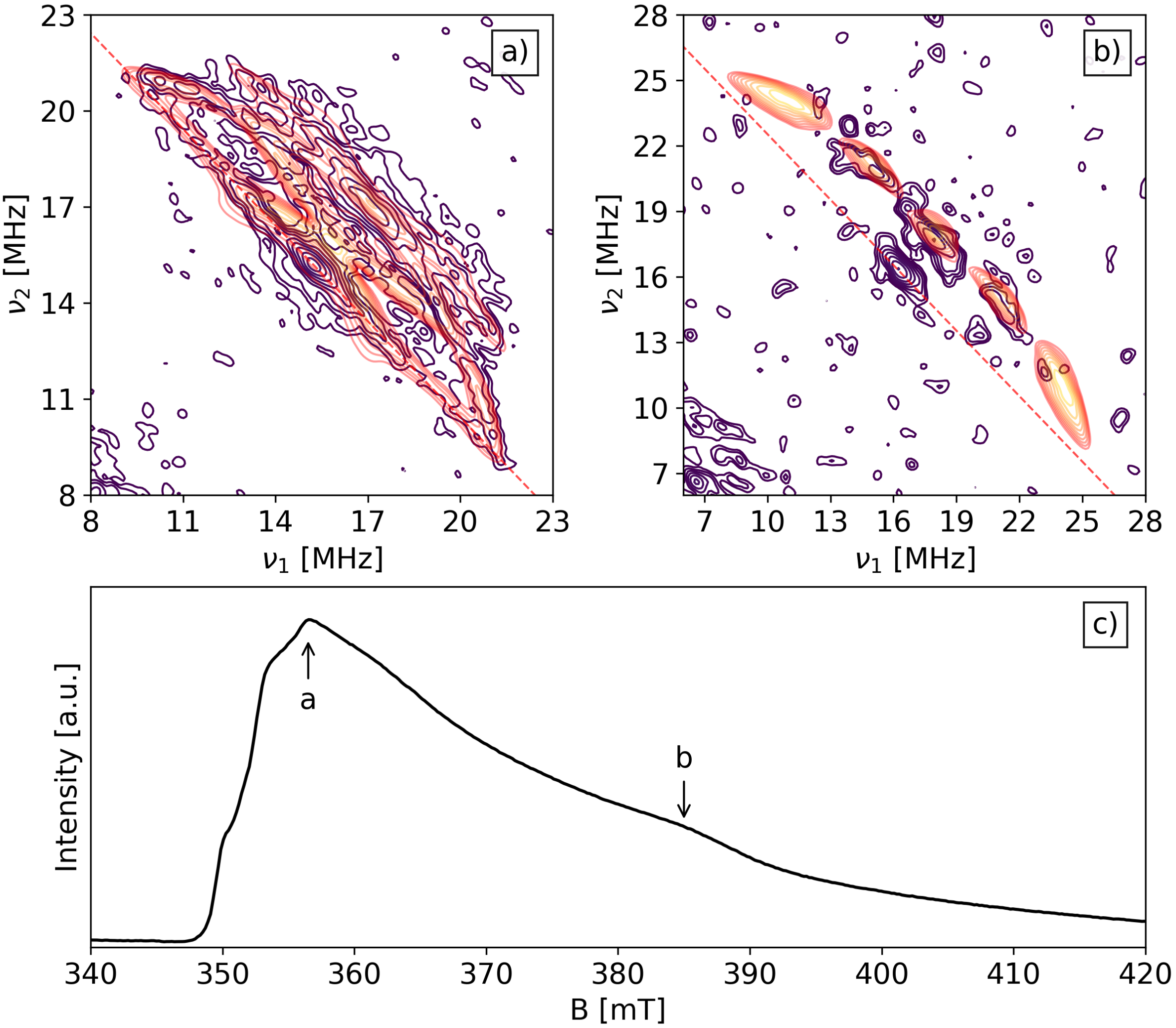

Figure 5.16: The experimental (purple) and simulated (orange) ^{1}H HYSCORE spectra of **L20** at two field positions indicated in the EDFS spectrum (c). The spectrum measured at a) 356.5 mT is superimposed with τ = 100, 132, 254 ns and b) 385 mT is superimposed with τ = 124, 154 ns.

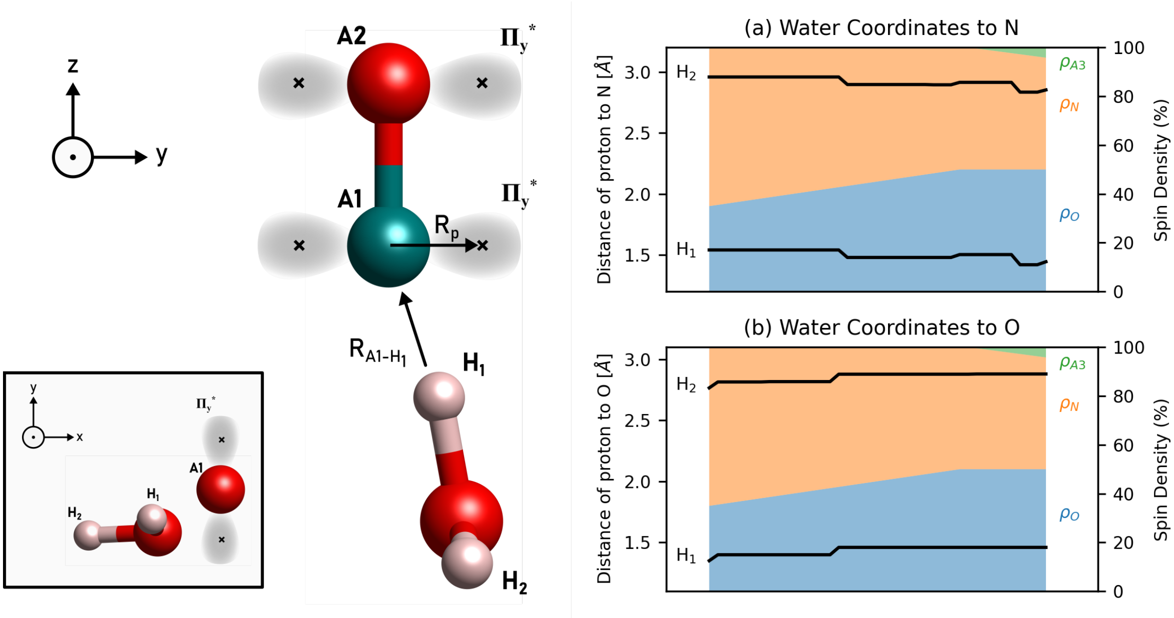

Figure 5.17: The scheme on the left is the water-NO coordination used for *hfi* theoretical calculation. The crosses in the shaded area indicate the covalent radii R_p for the p orbitals of nitrogen and oxygen.[44] Figures on the right are the R_{A1-H_1} corresponding to spin density distributed on N, O, and/or a third atom (A3). The sub-figure (a) is for the case where atoms A1 = N and A2 = O; and sub-figure (b) is for the case wher atoms A1 = O and A2 = N.

the distances of the two protons to the coordinated atom while the background colors indicate the proportion of the spin density on each atom. The results show that the distances in the case of the water molecule coordinating to nitrogen are slightly larger than to oxygen. The order of the difference is however beyond the accuracy of the HYSCORE experiment. Therefore, it is indistinguishable the two coordination cases as well as the different spin density distributions. Nevertheless, the results can be used as a starting point in the geometry optimization of DFT calculation.

Bibliography

(1) Liao, Y. K.; Bruzzese, P. C.; Hartmann, M.; Pöppl, A.; Chiesa, M. *Journal of Physical Chemistry C* **2021**, *125*, 8116–8124 (cited on pages 57, 61, 66).

(2) Padlyak, B. V.; Kornatowski, J.; Zadrozna, G.; Rozwadowski, M.; Gutsze, A. *Journal of Physical Chemistry A* **2000**, *104*, 11842–11843 (cited on page 57).

(3) Zhu, Z.; Wasowicz, T.; Kevan, L. *Electron Spin Resonance and Electron Spin Echo Modulation Spectroscopic Studies of Chromium Ion Location and Adsorbate Interactions in Calcined CrAPSO-11*; technical report; 1997 (cited on page 57).

(4) Weckhuysen, B. M.; Schoonheydt, R. A. *Zeolites* **1994**, *14*, 360–366 (cited on page 57).

(5) Zhu, Z.; Kevan, L. *Physical Chemistry Chemical Physics* **1999**, *1*, 199–206 (cited on page 57).

(6) Weckhuysen, B. M.; Schoonheydt, R. A.; Mabbs, F. E.; Collison, D. *Journal of the Chemical Society - Faraday Transactions* **1996**, *92*, 2431–2436 (cited on page 57).

(7) Greenblatt, M.; Pifer, J. H.; McGarvey, B. R.; Wanklyn, B. M. *The Journal of Chemical Physics* **1981**, *74*, 6014–6017 (cited on page 61).

(8) Greenblatt, M.; Pifer, J. H. *The Journal of Chemical Physics* **1979**, *70*, 116–122 (cited on page 61).

(9) Greenblatt, M.; Pifer, J. H.; Banks, E. *Journal of Chemical Physics* **1977**, *66*, 559–562 (cited on page 61).

(10) Banks, E.; Greenblatt, M.; McGarvey, B. R. *The Journal of Chemical Physics* **1967**, *47*, 3772–3780 (cited on page 61).

(11) Kasumaj, B.; Stoll, S. *Journal of Magnetic Resonance* **2008**, *190*, 233–247 (cited on page 61).

(12) Maurelli, S.; Berlier, G.; Chiesa, M.; Musso, F.; Corà, F. *Journal of Physical Chemistry C* **2014**, *118*, 19879–19888 (cited on pages 61, 63, 65, 66, 69).

(13) Piovano, A.; Thushara, K. S.; Morra, E.; Chiesa, M.; Groppo, E. *Angewandte Chemie - International Edition* **2016**, *55*, 11203–11206 (cited on pages 61, 63, 66).

(14) Stamos, N. A.; Ferentinos, E.; Chrysina, M.; Raptopoulou, C. P.; Psycharis, V.; Sanakis, Y.; Pantazis, D. A.; Kyritsis, P.; Mitrikas, G. *Inorganic Chemistry* **2020**, *59*, 3666–3676 (cited on pages 63, 66).

(15) Dikanov, S. A.; Liboiron, B. D.; Orvig, C. *Molecular Physics* **2013**, *111*, 2967–2979 (cited on pages 63, 66).

(16) Fitzpatrick, J. A.; Manby, F. R.; Western, C. M. *Journal of Chemical Physics* **2005**, *122*, DOI: `10.1063/1.1851501` (cited on pages 63, 66).

(17) Lagostina, V.; Salvadori, E.; Chiesa, M.; Giamello, E. *Journal of Catalysis* **2020**, *391*, 397–403 (cited on pages 63, 65).

(18) Ha, V. T. T.; Sarioğlan, A.; Erdem-Şenatalar, A.; Taârit, Y. B. *Journal of Molecular Catalysis A: Chemical* **2013**, *378*, 279–284 (cited on page 65).

(19) Lee, C. W.; Saint-Pierre, T.; Azuma, N.; Kevan, L. *The Journal of Physical Chemistry* **1993**, *97*, 11811–11814 (cited on pages 65, 69).

(20) Lagostina, V.; Romeo, E.; Maria Ferrari, A.; Maurino, V.; Chiesa, M. *Journal of Catalysis* **2022**, *406*, 28–38 (cited on pages 65, 71).

(21) Schweiger, A.; Jeschke, G., *Principle of Pulse Electron Paramagnetic Resonance*; Oxford University Press: Oxford, 2001 (cited on page 66).

(22) Höfer, P. Distortion-Free Electron-Spin-Echo Envelope-Modulation Spectra of Disordered Solids Obtained from Two-Dimensional and Three-Dimensional HYSCORE Experiments, 1994 (cited on page 66).

(23) Maurelli, S.; Chiesa, M.; Giamello, E.; Leithall, R. M.; Raja, R. *Chemical Communications* **2012**, *48*, 8700–8702 (cited on page 69).

(24) Abdo, S.; Howe, R. F. *Journal of Physical Chemistry* **1983**, *87*, 1722–1730 (cited on page 69).

(25) Louis, C.; Che, M.; Anpo, M. *Journal of Catalysis* **1993**, *141*, 453–464 (cited on page 69).

(26) Rhimi, B.; Mhamdi, M.; Kalevaru, V. N.; Martin, A. *RSC Advances* **2016**, *6*, 65866–65878 (cited on page 69).

(27) Morton, J. R.; Preston, K. F. *Journal of Magnetic Resonance (1969)* **1978**, *30*, 577–582 (cited on page 71).

(28) Kasai, P. H.; Bishop, R. J. *Journal of the American Chemical Society* **1972**, *94*, 5560–5566 (cited on pages 71, 72, 74).

(29) Pöppl, A.; Rudolf, T.; Michel, D. *Journal of the American Chemical Society* **1998**, *120*, 4879–4880 (cited on page 71).

(30) Pöppl, A.; Rudolf, T.; Manikandan, P.; Goldfarb, D. *Journal of the American Chemical Society* **2000**, *122*, 10194–10200 (cited on pages 71, 72, 74, 77).

(31) Barth, B.; Mendt, M.; Pöppl, A.; Hartmann, M. *Microporous and Mesoporous Materials* **2015**, *216*, 97–110 (cited on page 71).

(32) Yahiro, H.; Lund, A.; Shiotani, M. *Spectrochimica Acta Part A: Molecular and Biomolecular Spectroscopy* **2004**, *60*, 1267–1278 (cited on page 71).

(33) Chiesa, M.; Giamello, E.; Che, M. *Chemical Reviews* **2010**, *110*, 1320–1347 (cited on page 71).

(34) LUNSFORD, J. *Journal of Catalysis* **1969**, *14*, 379–385 (cited on pages 72, 74).

(35) Gardner, C. L.; Weinberger, M. A. *Canadian Journal of Chemistry* **1970**, *48*, 1317–1322 (cited on page 72).

(36) Che, M.; Tench, A. In *Advances in Catalysis*; C, 1983; Vol. 32, pp 1–148 (cited on page 72).

(37) Känzig, W.; Cohen, M. H. *Physical Review Letters* **1959**, *3*, 509–510 (cited on page 72).

(38) Zeller, H. R.; Shuey, R. T.; Känzig, W. *Le Journal de Physique Colloques* **1967**, *28*, 4–81 (cited on page 72).

(39) Dousmanis, G. C. *Physical Review* **1955**, *97*, 967–970 (cited on pages 72, 74).

(40) Mendt, M.; Barth, B.; Hartmann, M.; Pöppl, A. *Journal of Chemical Physics* **2017**, *147*, DOI: `10.1063/1.4995551` (cited on page 72).

(41) Rudolf, T.; Böhlmann, W.; Pöppl, A. *Journal of Magnetic Resonance* **2002**, *155*, 45–56 (cited on page 74).

(42) Dikanov, S. A.; Tyryshkin, A. M.; Bowman, M. K. *Journal of Magnetic Resonance* **2000**, *144*, 228–242 (cited on pages 75–77).

(43) Chrysina, M.; Zahariou, G.; Ioannidis, N.; Sanakis, Y.; Mitrikas, G. *Magnetochemistry* **2021**, *7*, DOI: `10.3390/magnetochemistry7090131` (cited on page 77).

(44) Cordero, B.; Gómez, V.; Platero-Prats, A. E.; Revés, M.; Echeverría, J.; Cremades, E.; Barragán, F.; Alvarez, S. *Dalton Transactions* **2008**, 2832 (cited on pages 77, 79).

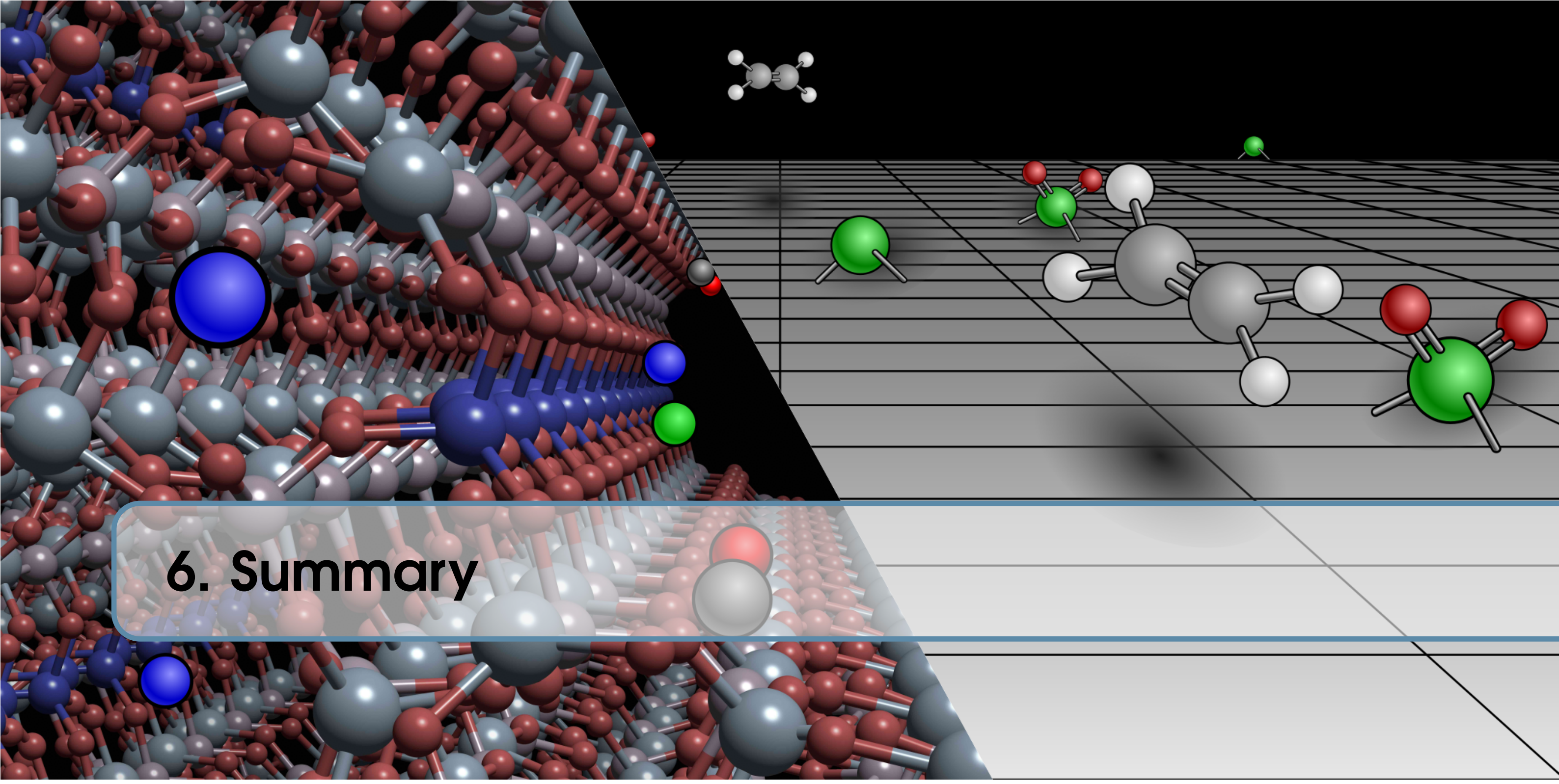

6. Summary

Phillips Catalyst

The activated Phillips catalyst shows two Cr(V) species overlapping in the X-band CW-EPR spectra. The EDFS techniques were applied to disentangle the two species and obtain their spin Hamiltonian parameters. The spin Hamiltonian parameters indicate that the two Cr(V) species can have very different local geometry. The quantitative analysis indicate Cr(V)A being more reactive than Cr(V)B and suggest that the Cr(V)B can be an intermediate species as it grew in intensity during the reaction. However, without direct observation on the other diamagnetic/EPR-silent Cr species, such assignment can hardly be verified. Meanwhile, the total amount of the paramagnetic Cr changes over time indicate no direct correlation between different species. Lastly, the results combining spin counting, which provides information on the overall spin concentration, and the instantaneous diffusion analysis, which provides the information on the local concentration, indicate cluster the Cr(V) species in the activated Phillips catalyst.

Organometallic Cr on Silica

The CW-EPR spectra of the $n\mathrm{Cr[CH(SiMe_3)_2]_3/SiO_2}$ catalysts consist of three groups of paramagnetic Cr: the Cr(V) impurities, the Cr_{Oligom} sites (Cr(III)A), and the Cr_{Polym} sites (Cr(III)B). Cr(III)A is characterized by their large D and orthorhombic distortion E/D which is similar to the $\mathrm{Cr[CH(SiMe_3)_2]_3}$ precursor with lower symmetry. On the other hand, Cr(III)B is characterized by the smaller zfs which is assigned to a distorted octahedral coordination of the surface-bound species. The quantitative analysis shows that the relative amount of the Cr(III)A is increased with higher Cr loading. Put together with the analysis on the produced polymer and the DR UV-vis-NIR, the Cr(III)A is attributed to the Cr_{Oligom} sites that oligomerize ethylene to α-olefin and similarly attributed Cr(III)B to the Cr_{Polym} sites for ethylene polymerization.

Cr-Incorporated SAPO-5

The X-band CW-EPR spectrum of the as-synthesized Cr-SAPO-5 show the characteristic Cr^{3+} signal. After the calcination, the presence of Cr^{5+} species is demonstrated by the CW-EPR signals that resonant at $g_z = 1.985 \pm 0.001$, $g_y = 1.972 \pm 0.001$, $g_x = 1.953 \pm 0.003$. It was assigned to a distorted tetrahedral coordination.

The HYSCORE spectra of the Cr^{5+} species reveal the cross-peaks on the diagonal centered at ^{27}Al Larmor frequency with large *hfi* dominated by the isotropic component a_{iso}. The following analysis shows the corresponding spin density transfer to the Al 3s orbital is of the order of 0.06-0.5 %, consistent with the Cr–O–Al linkage. The 6-pulse HYSCORE spectrum also shows a ridge at the ^{31}P Larmor frequency with extension of about 2 MHz assigned to distant (> 0.4 nm) P species in the fourth coordination sphere of Cr^{5+}. The presence of Al species with large *hfi* coupling and remote P species alongside have provided evidence of Cr^{5+} incorporated at the P^{5+} framework sites.

Bi-metallic Mo/V-SAPO-5

The CW-EPR spectra of the VCl_4 grafted SAPO-5 shows characteristic signals of the V^{4+} coincide with the reported VO^{2+} species.[1, 2] The HYSCORE spectra show cross-peaks along the diagonals centered at the ^{27}Al and ^{31}P Larmor frequencies. The computer simulations provided *hfi* dominated by a_{iso} for both the Al and P nuclei and suggested spin density transfer to them of the order of 0.1 %. The presence of Al and P nuclei with large *hfi* indicates the V^{4+} species were grafted at the extra-framework positions.

The CW-EPR spectra of the VCl_4 doses to the Mo-SAPO-5 indicate the Mo^{6+} species reduced by the V^{4+} via a single electron transfer reaction. The HYSCORE spectra show cross-peaks that are analogous to the Al and P signals in the V-SAPO-5 sample. In addition, at the low frequency range observed complex spectral feature that were attributed to the multi-quantum nuclear transitions of ^{95,97}Mo with large *hfi*. The detection of Mo hyperfine couplings corresponding to the spin density transfer of the order of 0.1 % can be explained by the interaction between the V^{4+} species and the covalently bound Mo^{6+}. This then points to the presence of electronic interactions at short range order, compatible with V–O–Mo linkages. With the results, conclusion can be drawn that the V and Mo species are grafted at the extra-framework sites of SAPO-5 via reaction of gas phase precursors.

NO-Adsorbed SAPO-5

The CW-EPR spectra of the NO-adsorbed SAPO-5 show signals of the typical physisorbed NO species with $g_\perp > g_\|$ and the splitting at the $g_\perp$ caused hyperfine coupling due to the spin density at the ^{14}N $2p\pi$ orbital. The lower $g_\|$ observed for **L20** might due to the lack of cation adsorption sites in SAPO-5 and the shielding of electric field by water molecules. The former suggestion is supported by the higher A^N_{yy} observed for the sample suggesting the higher spin density localized at ^{14}N $2p\pi$ orbital as compared with the literature. The shifting of the $g_\|$ between the samples activated at different temperatures indicates the NO molecules are adsorbed at different sites.

The ^{27}Al HYSCORE spectra show different remote ^{27}Al species characterized by the splitting of the cross-peaks caused by *nqi*. It is hypothesized as the NO molecules are adsorbed at the defect sites in **H10** where ^{27}Al species with significant *nqi* were observed; and in **L20** the water molecules preoccupy such defect sites resulting in observing the dominant ^{27}Al species in HYSCORE. This is supported by doubling the NO dosage in **H20** and saturating the defect sites with excessive adsorbed NO; both Al species were observed in HYSCORE in this case. The presence of water molecules is supported by cross-peaks of proton with large *hfi* only appear in the ^{1}H HYSCORE of **L20**. The suggested structure of the NO-water is given here by working out first the full ^{1}H hyperfine tensor and attempting to calculate the coordination accordingly. The results provide no distinction between the case of water molecule binding to N or O of NO. However, the direct coordination of water to NO is unambiguously proven. This structure can be used as the starting point of DFT computation later on.

Bibliography

(1) Maurelli, S.; Berlier, G.; Chiesa, M.; Musso, F.; Corà, F. *Journal of Physical Chemistry C* **2014**, *118*, 19879–19888 (cited on page 84).

(2) Lagostina, V.; Salvadori, E.; Chiesa, M.; Giamello, E. *Journal of Catalysis* **2020**, *391*, 397–403 (cited on page 84).

A. Acronyms and Symbols

Acronyms

EZ Electron Zeeman Interaction. 16
NZ Nuclear Zeeman Interaction. 16
hfi Hyperfine Interaction. 4
nqi Nuclear Quadrupole Interaction. 6
zfi Zero-Field Interaction. 3

AlPO Aluminophosphate. 5
APO Aluminophosphate. 5

CTP Coherence Transferring Pathways. 30
CW Continuous Wave. 4

DFT Density Functional Theory. 57

EC Electron Coherence. 28
EDFS Echo-Detected Field Sweep. 26
ELDOR Electron-Electron Double Resonance. 28
ENDOR Electron Nuclear Double Resonance. 5
EPR Electron Paramagnetic Resonance. 1
ESEEM Electron Spin Echo Envelop. 5

HDPE High-Density Polyethylene. 1
HYSCORE Hyperfine Sublevel Correlation. 4

NC Nuclear Coherence. 28
NMR Nuclear Magnetic Resonance. 6
NP Nuclear Polarization. 30

PXRD Powder X-ray Diffraction. 36

SAPO Silico-Aluminophosphate. 5
SHC Supported homogenous Catalysis. 4
SOMC Surface Organometallic Chemistry. 4
SSHC Single-Site Heterogeneous Catalyst. 5

TMI Transition Metal Ion. 1

Symbols

A	secular hyperfine coupling
$\mathbf{A}$	hyperfine interaction tensor
a_{iso}	isotropic component of hyperfine coupling
B	pseudo-secular hyperfine coupling
$\mathbf{B}_0$	magnetic field
g_e	free-electron g value (2.002331)
g_n	nuclear g value
h	Planck constant ($6.6260755\times10^{-34}\,\mathrm{J\cdot s}$)
$\hbar$	reduced Planck constant ($1.05457266\times10^{-34}\,\mathrm{J\cdot s}$)
$\mathcal{H}$	Hamiltonian
$\mathbf{I}$	nuclear spin operator
I	nuclear spin quantum number
$\mathbf{P}$	nuclear quadrupole tensor
$\mathbf{S}$	electron spin operator
S	electron spin quantum number
$\mathbf{T}$	dipolar hyperfine tensor
T	axial component of hyperfine coupling
T_1	longitudinal relaxation time
T_m	phase memory time
α	first Euler angle
β	second Euler angle
β_B	Bohr magneton ($9.27400899\times10^{-24}\,\mathrm{J\cdot T^{-1}}$)
β_n	nuclear magneton ($5.05078317\times10^{-27}\,\mathrm{J\cdot T^{-1}}$)
γ	third Euler angle
μ_0	permeability of vacuum ($4\pi\times10^{-7}\,\mathrm{N\cdot A^{-2}}$)
ν	frequency
ω	angular frequency ($2\pi\nu$)

Acknowledgement

I would like to thank my supervisors, Prof. Mario Chiesa and Prof. Andreas Pöppl, for helping me to get through various obstacles in the course of my PhD study. The study is like climbing a mountain and they are the ones who pointed out the direction and taught me how to do it. There were also people who supplied me with resources, lent me the gears, and accompanied me on the way. For that I would also like to thank the colleagues of the EPR groups in Turin and in Leipzig, the people at ECRC in Erlangen, and the fellow ESRs in the PARACAT project. They provide a good environment for me to do the work. And the ideas came out in many interesting discussions were also invaluable. Lastly, I thank the support from my friends and family. Without them, I might not persist until now.

This work is part of the PARACAT project that received funding from the European Union's Horizon 2020 research and innovation programme under the Marie Skłodowska-Curie grant agreement No 813209.